LBL-176
c.2

SHORT RANGE ORDER

Santosh Kumar Das
(Ph. D. Thesis)

November 1971

AEC Contract No. W-7405-eng-48

TWO-WEEK LOAN COPY

This is a Library Circulating Copy which may be borrowed for two weeks. For a personal retention copy, call Tech. Info. Division, Ext. 5545

LAWRENCE BERKELEY LABORATORY • UNIVERSITY OF CALIFORNIA • BERKELEY

LBL-176
c.2

25

DISCLAIMER

This document was prepared as an account of work sponsored by the United States Government. While this document is believed to contain correct information, neither the United States Government nor any agency thereof, nor the Regents of the University of California, nor any of their employees, makes any warranty, express or implied, or assumes any legal responsibility for the accuracy, completeness, or usefulness of any information, apparatus, product, or process disclosed, or represents that its use would not infringe privately owned rights. Reference herein to any specific commercial product, process, or service by its trade name, trademark, manufacturer, or otherwise, does not necessarily constitute or imply its endorsement, recommendation, or favoring by the United States Government or any agency thereof, or the Regents of the University of California. The views and opinions of authors expressed herein do not necessarily state or reflect those of the United States Government or any agency thereof or the Regents of the University of California.

SHORT RANGE ORDER

Contents

Abstract v

I. Introduction 1

II. Experimental Procedure

2.1 Alloy and Specimen Preparation 6

2.2 Preparation of Single Crystal Thin Films 7

2.3 Electron Microscopic Techniques 9

III. Results

3.1 The Short Range Ordered Alloys 10

3.1.1 Ni_4Mo 10

3.1.2 Ni_3Mo 15

3.1.3 Au_3Cr 17

3.1.4 Au_4Cr 21

3.1.5 Au_4V 22

3.1.6 Au_3Mn 22

3.2 Development of Long Range Order in Ni-Mo Alloys . . . 26

3.2.1 Ni_3Mo 26

3.2.2 Ni_4Mo 33

3.3 Summary of Experimental Results 38

IV. Discussion 39

4.1 Statistical Thermodynamic Model of SRO 40

4.2 Structural Interpretation of the SRO State 43

4.3 The Formation of Metastable Ni_2Mo Phase 50

4.4 The Origin of the Tweed Pattern 53

V. Conclusions 55

Acknowledgments 57

References 58

Figure Captions 61

Figures 66

SHORT RANGE ORDER

Santosh Kumar Das
Inorganic Materials Research Division, Lawrence Berkeley Laboratory
Department of Materials Science and Engineering, College of Engineering
University of California, Berkeley, California 94720

ABSTRACT

The nature of short range order (sro) has been investigated in the systems Au_4Cr, Au_3Cr, Ni_4Mo, Ni_3Mo, Au_3Mn and Au_4V, by transmission electron microscopy and diffraction. The examination of the sro state, in the hot stage at temperatures above the critical temperature (T_c) for order-disorder transformation and also in the samples that were quenched from above T_c, showed diffuse scattering peaks centered near $\{1\frac{1}{2}0\}$ positions in the fcc reciprocal lattice, whose shape changed from one system to another. Evidence for diffuse scattering near superlattice positions corresponding to the Dla structure was obtained in the high temperature diffraction patterns of Au-Cr and also in the quenched samples. The Au-V system also showed similar behavior. The diffraction patterns of Au_3Mn above T_c showed evidence for the presence of diffuse scattering near the superlattice positions corresponding to Watanabe type two-dimensional long period superstructure. The sro diffuse scattering in Ni_3Mo and Ni_4Mo show presence of weak Dla and Ni_2Mo superlattice reflections, in addition to the $\{1\frac{1}{2}0\}$ peaks. The existence of the diffuse scattering near these various superlattice positions is taken as the evidence for the presence of microdomains of corresponding superstructures. The diffuse scattering near $\{1\frac{1}{2}0\}$ positions is interpreted to be due to the presence of imperfectly

ordered DO_{22} type microdomains. The direct evidence of these microdomains is obtained by dark field images of the corresponding superlattice reflections only after a short time aging at low temperatures.

Using the pairwise interaction parameters up to third nearest neighbors in the existing statistical thermodynamic model of Clapp and Moss one can partially account for the shapes of $\{1\frac{1}{2}0\}$ sro spots in Ni-Mo and Au-Mn alloys, but not in Au-Cr and Au-V alloys. On the other hand the diffuse sro scattering in all these alloys can be qualitatively explained by assuming the presence of imperfectly ordered microdomains of various superstructures that may exist in the long range ordered (ℓro) state in these alloys. For a particular stoichiometry, the structures of the microdomains that exist above T_c may or may not correspond to the equilibrium ℓro structure obtained at that stoichiometric composition. This description of the sro state to consist of a mixture of various types of microdomains is in accord with recent theoretical probability variational calculations of Clapp.

The development of ℓro in Ni_3Mo is associated with decomposition into the metastable phases Ni_2Mo and Ni_4Mo, the microdomains corresponding to which were present in the sro state. Evidence for the presence of metastable Ni_2Mo phase was also found during ordering of Ni_4Mo. Thermodynamic justification has been given for the occurrence of these metastable phases.

I. INTRODUCTION

A solid solution having short range order (sro) usually exhibits diffuse maxima in the diffraction patterns. In order to explain the shape and position of these diffuse maxima various models of the sro state have been proposed. These fall into two main categories, namely the statistical thermodynamic model and the microdomain or more generally the structural model. According to the statistical thermodynamic model the sro is said to exist when there is a tendency for each atom to be surrounded by more than an average number of unlike atoms and in the microdomain model the sro state is described as an assembly of ordered microdomains separated by antiphase domain boundaries or other discontinuities. Both models can satisfactorily explain the positions of the sro diffuse maxima in the systems where they coincide with the superlattice reflections, that appear in the long range ordered (ℓro) state. In the microdomain model the diffuse sro maxima are explained as due to the broadening of the superlattice reflections arising from very small domain size. So this model requires that the position of sro maxima in reciprocal space should always coincide with that of the superlattice reflections.

Certain systems such as Ni_4Mo,[1] Ni_4W,[2] Au_3Cr,[3] and several Ti-O alloys,[4] have been found to exhibit sro diffuse maxima at positions other than the superlattice positions. In the ordered state the first three alloys are isostructural and possess a body centered tetragonal structure commonly known as D1a, and are disordered f.c.c. above the critical temperature (T_c). The s.r.o. diffuse maxima in these three systems occur at all equivalent $\{1\ \frac{1}{2}\ 0\}$ positions of the f.c.c. reciprocal

lattice, which are not superlattice positions. So the microdomain model fails to explain the position of sro maxima in these systems. On the other hand the recent statistical thermodynamic model of Clapp and Moss[5,6] is able to predict the shape and position of the diffuse $\{1\ \frac{1}{2}\ 0\}$ maxima in Ni_4Mo, which agrees well with the X-ray measurements of Spruiell and Stansbury.[1] On this basis they rejected the microdomain concept of sro at least for this Ni_4Mo system.

More recently Clapp[37] has used a Probability Variation Method to determine the complete frequency distribution of nearest neighbor configurations for a number of cubic alloys from their experimentally determined sro parameters. His calculations show that the most enhanced configuration relative to the random state often corresponds to the perfectly ordered state. Although no calculations were done for the system Ni_4Mo, the results for the system suggest that the microdomain concept of sro cannot be totally rejected. Recently Okamoto and Thomas[7,8] have shown that the microdomain concept is still valid for the system Ni_4Mo and the $\{1\ \frac{1}{2}\ 0\}$ diffuse maxima can be explained by the presence of non-conservative antiphase boundaries (APB's) within the mic rodomains which give rise to imperfectly ordered regions with DO_{22} superstructure. The presence of microdomains was inferred from the diffraction evidence that samples of Ni_4Mo quenched from above T_c showed weak superlattice reflections at Dla positions co-existing with much stronger $\{1\ \frac{1}{2}\ 0\}$ peaks.

On the other hand Tanner, et al.,[3] while investigating the Au_3Cr and Au_3Mn systems, the two other systems that also exhibit $\{1\ \frac{1}{2}\ 0\}$ sro maxima, did not report any evidence of superlattice reflections in the sro state. However, in their at temperature electron diffraction studies

of Au_3Cr above T_c, they examined only [100] reciprocal lattice section and as has been pointed out earlier[8] this reciprocal lattice section is not very suitable for detection of weak Dla superlattice reflections and it is essential to examine other reciprocal lattice sections such as [$\bar{1}$30]. So it is still uncertain as to whether microdomains exist in these systems or not. Since the diffraction evidence for the presence of microdomains in Ni_4Mo system is based on the examination of quenched samples and quenching may have induced some ordering, there is some question as to whether the observed scattering actually represents the sro state at temperatures above T_c or not. Thus, the microdomain model still lacks generality. The primary objective of this thesis is to see if the microdomain concept of sro is true in general or not, expecially for the systems where the diffuse sro maxima are not coincident with the superlattice reflections. For this a number of systems such as Ni_4Mo, Ni_3Mo, Au_3Cr, Au_4Cr, Au_3Mn, and Au_4V were chosen. The choice behind these different systems lies in the fact that all of them do not have the same ℓro structure, and still they exhibit sro diffuse maxima at the same position namely $\{1\ \frac{1}{2}\ 0\}$. The systems Au_4Cr, Au_3Cr, Ni_4Mo, Au_4V are isostructural with Dla, Ni_3Mo is orthorhombic where as Au_3Mn has a two-dimensional long period superstructure. It was hoped that a comparative study of these various systems would reveal the true nature of the sro from the structural point of view.

The diffraction patterns of these various alloy systems were examined both in the specimens quenched from above T_c and wherever possible at temperatures above T_c, in order to see if there is any difference in the diffuse scattering behavior. If the sro state consists of microdomains

of a particular ordered structure, there must be some scattering near the superlattice positions corresponding to that structure and thus a difference in the diffuse scattering behavior will be expected in the systems having different lro structures. During this work special attention was given to detect the presence or absence of these weak superlattice spots corresponding to different superstructures.

The results of the study of the sro state of Ni_4Mo and Ni_3Mo show that they are similar in the quenched state and contain weak superlattice reflections corresponding to Ni_4Mo and Ni_2Mo superstructures. This raises the question as to how these alloys order at the very early stages of aging, because the Ni_2Mo phase has never been observed in Ni_4Mo, although there have been a number of studies,[8-13] both by X-ray and electron diffraction, on the ordering of Ni_4Mo. In the alloy Ni_3Mo Yamamoto et al.[14] found that on aging it initially decomposes to Ni_2Mo when then N-$_4$Mo precipitates and both these phases co-exist. On prolonged aging these are subsequently replaced by equilibrium Ni_3Mo. Thus, it is not clear why the Ni_2Mo phase forms at stoichiometric Ni_3Mo composition. Since the sro study shows weak superlattice reflections corresponding to both Ni_2Mo and Ni_4Mo to be present; in the quenched samples of Ni_3Mo and Ni_4Mo, one would expect these two alloys to behave similarly at the very early stages of the development of long range order, i.e. the Ni_2Mo phase may also form as a metastable phase in Ni_4Mo. In order to resolve this, the initial stages of ordering in both Ni_4Mo and Ni_3Mo were studied by electron microscopy and diffraction for various isothermal annealing treatments. Attempts were made to answer whether the metastable Ni_2Mo

or not, and if Ni_2Mo is present as a metastable phase, to find a possible mechanism for its formation and to provide thermodynamic justification for the formation of this metastable phase, both in Ni_3Mo and Ni_4Mo.

Although the main aim of this thesis is understanding the nature of sro, it is necessary to study the initial stages of ordering in Ni_3Mo and Ni_4Mo, because the development of ℓro depends very much on what is present in the sro state. Thus the information obtained from the ℓro structure or structures that develop at the early stages can be used for the understanding of sro state. This is especially important for a system like Ni_3Mo where the diffuse sro scattering does not show any evidence for the presence of Ni_3Mo superlattice reflections.

II. EXPERIMENTAL PROCEDURE

2.1. Alloy and Specimen Preparation: Bulk alloys of Au_3Cr, Ni_4Mo, Ni_3Mo and Au_4V were prepared by melting together required proportions of the individual components in an arc furnace, back filled with argon. The purity of all the starting materials were 99.99% except for Vanadium which was 99.9% pure. The alloys were melted several times in the furnace. After each melt, the ingot was cut into small pieces and the pieces were intermixed and then remelted in order to obtain a homogeneous composition. The ingots were encapsulated in quartz tubes in vacuum and were homogenized at suitable temperatures for three days. The compositions of the bulk alloys and their corresponding homogenization temperatures are shown in Table 1.* The ingots were

TABLE 1. Composition of the Bulk Alloys

Alloy	Atomic % Solute	Homogenization Temp (°C)
Ni_4Mo	Mo - 19.7	1200
Ni_3Mo	Mo - 25.1	1270
Au_3Cr	Cr - 23.5	900
Au_4V	V - 19.1	900

quenched into water and then cold rolled to 6 mil strips with intermediate anneals. The foils were then finally homogenized in an inert atmosphere and quenched directly into iced brine from their homogenization temperature.

The thin foils of Ni-Mo alloys for transmission electron microscopy were prepared in two stages. The 6 mil foils were first electrolytically

thinned to 1-2 mils by window technique using a solution containing 396cc ethylene glycol, 57cc perchloric acid, 57cc hydrofluoric acid, and 27cc distilled water. The temperature of the solution was maintained at 10°C and the applied voltage was 9-11 volts. From these 1-2 mil foils 2.3 mm discs were punched out and were finally jet polished in an electrolyte containing two parts of sulphuric acid and one part water, keeping the total current below 10 milliamps. The thin foils of Au alloys were relatively difficult to prepare and the window method was again used with an electrolyte containing 88 gms of chromic oxide, 465cc acetic acid, 25cc water.

2.2. Preparation of Single Crystal Thin Films: For high temperature transmission electron microscopic studies it is necessary to have thin foils with large transparent areas, because at high temperatures holes start forming and thin areas are gradually eaten up. Because of the difficulty in obtaining large thin areas in the thin foils of bulk Au-alloys by electropolishing, it was decided to grow epitaxial single crystal thin films of Au-Cr alloys. This method gives large single crystal thin films of desired thickness and such films have been used by many workers in the past for the order-disorder studies of Cu-Au and other alloys. The alloy single crystal films can be prepared either by simultaneous evaporation of the two elements or by evaporating separately one on the top of the other and then diffusing them. In the present case a different method, the evaporation of bulk Au_3Cr alloy was employed. This method will be successful only if the vapor pressures of the two elements in the binary alloy are same at the evaporation temperature and in this case Au and Cr

have similar vapor pressures.

The weight of the bulk alloy (W) requirement was calculated from the simple expression,

$$W = 4\pi R^2 t\rho$$

where R is the distance of the substrate from the filament, t is the required thickness of the film and ρ is the density of the alloy Au_3Cr. The thickness of the thin films were in the range 300-600Å, and so the weight of the alloy required was very small and was weighed accurately up to 0.1 milligrams. The required amount of bulk alloy was first premelted on a hair-pin type tungsten filament in a vacuum bell jar. A small furnace was built inside the bell jar to heat the substrate. Freshly cleaved 100 faces of NaCl were used as the substrate to grow films in [100] orientation. The substrate was first degassed at 550°C for 1/2 hour and then cooled to 450°C and was held at that temperature. The substrate temperature is very critical for obtaining good single crystal films and 450°C was found to give the best results for Au_3Cr. The premelted alloy was flash evaporated on to the substrate in order to obtain a film of the same composition as the bulk alloy, the evaporation time being about 30 seconds. At a slower evaporation rate the film composition may change due to the difference in mobility of the Au and Cr atoms. The films were homogenized at 400°C for about 2 hours. They were then stripped off the substrate by dissolving the rock salt in distilled water and were mounted on platinum grids. Further annealing was done

inside the microscope. The composition of the few films were checked by measuring the critical temperature (T_c) for order-disorder transition and was found to be close to that of Au_3Cr. The composition of the rest of the films were assumed to be close to stoichiometric Au_3Cr because of the identical evaporation procedure employed.

The thin films of Au_4Cr were prepared in a similar manner by melting together required amounts of Au with the bulk Au_3 on the filament to form the alloy Au_4Cr and then evaporating on to the heated rock salt. The evaporated thin films of Au_3Mn were obtained from Mr. Lee Tanner of Kennecott Copper Corporation and were similar to those employed in his studies.

2.3. Electron Microscopic Techniques: All the microscopy was done on a Siemens Elmiskop IA operated at 100 kV. A standard Siemens hot stage was used for the high temperature electron diffraction work. The hot stage was calibrated outside the microscope in a vacuum bell jar at a vacuum similar to that inside the microscope. The temperature on the grid was recorded directly on a Honeywell Electronik 19 recorder by spot welding a chromel-alumel thermocouple to the platinum grid. The steady state temperature and the time required to reach it were measured as a function of the applied voltage. Figure 1 shows the calibration curve obtained which is similar to that obtained earlier.[15]

III. RESULTS

3.1. The Short Range Ordered Alloys: The short range order study involved the examination of the electron diffraction patterns of the six systems Ni_4Mo, Ni_3Mo, Au_3Cr, Au_4Cr, Au_4V and Au_3Mn either in the specimens quenched from above T_c or at temperatures above T_c or both. Because of the large number of systems involved the results obtained on each system will be presented separately. The important crystallographic features of each of these systems will be pointed out first and then the diffuse scattering results will be described.

3.1.1. Ni_4Mo: In the ℓro state the stoichiometric Ni_4Mo has a body centered tetragonal structure[16] (space group - C_{4h}^5 -I 4/m) commonly referred to as D1a in the strukturbericht symbol. Figure 2 shows the partial phase diagram of the Ni_4Mo system and it can be seen that Ni_4Mo does not have a true order-disorder transition temperature but undergoes a peritectoid transformation around 865°C. However, at this peritectoid temperature the (α + Ni_3Mo) range is so narrow that disordered α transforms to Ni_4Mo as in any other order-disorder transformation. The crystallographic features of the ordered Ni_4Mo structure are well known,[8,9] but a few aspects that are important to this study will be described here. Figure 3a shows the unit cell of the ordered Ni_4Mo, where the dotted lines outline the original f.c.c. lattice. It is easier to visualize this ordered structure in relation to the original f.c.c. lattice and Fig. 3b shows the projection of atoms on the (001) plane. The b.c.t. cell is outlined by the dotted lines. The projection of atoms on the plane $\frac{a}{2}$ above are shown by the open circles. The important feature of this structure is that if one considers the stacking of atoms on {420}* planes, every fifth

*Unless mentioned, all the indices refer to the f.c.c. lattice.

plane contains only Mo atoms and in between planes contain only Ni atoms. Thus, the reciprocal lattice for the ordered structure can be constructed from the fundamental f.c.c. lattice, where the superlattice reflections appear at every $\frac{1}{5}$<420> reciprocal lattice vector of f.c.c. unit cell.

The other structure that is important to this study is the structure of Ni_2Mo phase in the phase diagram (Fig. 2) but occurs as a metastable phase during the ordering of Ni_3Mo. The atomic arrangement is isomorphous with the ordered Pt_2Mo (space group - D_{2h}^{25} - Immm) and Fig. 4a shows the body centered orthorhombic unit cell. The dotted line outlines the f.c.c. unit cell and the relationship between the disordered cubic lattice (α) and the ordered orthorhombic Ni_2Mo lattice are:

$$[100]_{Ni_2Mo} \;//\; [110]_{\alpha}$$

$$[010]_{Ni_2Mo} \;//\; [\bar{1}10]_{\alpha}$$

$$[001]_{Ni_2Mo} \;//\; [001]_{\alpha}$$

Figure 4b shows the projection of atoms on the (001) plane where the dotted line outlines the orthorhombic Ni_2Mo lattice and as before, the open circles represent atoms on a/2 layer above. Like the D1a structure this structure can be described by the stacking of atoms on either {420} or {220} planes where every third plane contains all Mo and in between all Ni atoms. Thus, the reciprocal lattice of the ordered structure can be constructed from the original f.c.c. lattice, where the superlattice reflections will appear at every $\frac{1}{3}$<220> or $\frac{1}{3}$<420> reciprocal lattice vectors. This gives rise to six orientation variants of Ni_2Mo corresponding to six variants of {220} and because of

the two-fold degeneracy associated with stacking on {420} planes. Figure 5a and b show the [001] and [$\bar{1}$30] reciprocal lattice sections constructed in the above manner. Here the positions of Dla and Ni_2Mo superlattice spots are shown together with the $\{1\frac{1}{2}0\}$ s.r.o. spots. As has been pointed out earlier,[8] the [$\bar{1}$30] orientation is very important for the detection of weak superlattice reflections in the s.r.o. state, because this reicprocal lattice section does not contain any $\{1\frac{1}{2}0\}$ s.r.o. spots, as can be seen in Fig. 5b. It is to be noted that each $\{1\frac{1}{2}0\}$ s.r.o. spot is surrounded by four Dla spots in the form of a tetrahedron with the $\{1\frac{1}{2}0\}$ s.r.o. spot at the center and the spots are not very far from each other. The small open circles in Fig. 5a represent the projection of Dla spots that are located at $\ell = \frac{1}{10}$th of [002] reciprocal lattice vector and the open squares in Fig. 5b are the projections of the neighboring $\{1\frac{1}{2}0\}$ s.r.o. spots. Keeping these crystallographic features in mind, we can now examine the diffuse scattering results.

Figure 6 shows a [001] diffraction pattern of a freshly quenched Ni_4Mo sample. The diffuse s.r.o. maxima can be seen at the $\{1\frac{1}{2}0\}$ positions. In the study of the quenched samples of Ni_4Mo Okamoto and Thomas[8] found weak scattering to be present near the Dla superlattice positions by examining [$\bar{1}$30] orientation, because in the [001] diffraction pattern it was difficult to detect them for the reason that they are very close to the $\{1\frac{1}{2}0\}$ s.r.o. spots as shown before (Fig. 5). However, if these Dla spots are present there should be an

enhanced scattering of $\{1\frac{1}{2}0\}$ spots towards the Dla positions and as a result the shape of the $\{1\frac{1}{2}0\}$ spots should be somewhat like the dotted triangle in Fig. 5. But the X-ray diffuse scattering measurements by Spruiell and Stansbury[1] on quenched samples of Ni_4Mo show the shape of $\{1\frac{1}{2}0\}$ spots to be quite different from the expected shape. Figure 7 is a reproduction of their diffuse scattering maps for Ni_4Mo quenched in iced brine from 1000°C. In this the outer contours at $(1\frac{1}{2}0)$ are slightly elongated towards the (100) and (210) positions and similarly for other equivalent $\{1\frac{1}{2}0\}$ spots. In order to resolve this apparent discrepancy isointensity contour maps were drawn on an isodensitracer from a number of diffraction patterns of the quenched samples of Ni_4Mo and Fig. 8 shows one such. The original map uses a color code for the relative intensities and Fig. 8 has been redrawn from the original for easy reproduction. The relative intensities are in arbitrary units. On this map the positions of the Dla and the Ni_2Mo superlattice reflections are also marked. It can be seen that the map is very similar to the X-ray map in Fig. 7. Here, the diffuse intensities near each of the $\{1\frac{1}{2}0\}$ positions are not exactly the same because the optic axis being at the origin (000), the deviations of each of the $\{1\frac{1}{2}0\}$ spots from the exact Bragg positions are different. However, the distribution of diffuse intensity in Fig. 8 suggests that there may be weak scattering present not only at the Dla positions but also at the superlattice positions corresponding to the Ni_2Mo structure. The observed enhanced scattering of $(1\frac{1}{2}0)$ spot towards (100) and (210) positions in [001] pattern is most likely to be due to the presence of weak scattering near the Ni_2Mo spots. In order to check this several other reciprocal lattice sections were examined and

Fig. 9 shows a [$\bar{1}$30] section. The diffuse peaks observed in this pattern are not entirely due to the weak D1a spots as was reported earlier by Okamoto and Thomas.[8] Careful measurements show that the center of these diffuse peaks do not lie exactly at the positions where the D1a spots ought to occur. It can be seen from Fig. 5b that the projection of the $\{1\frac{1}{2}0\}$ spots on tb the [$\bar{1}$30] reciprocal lattice section lies very close to that of the D1a spots. The diffuse peaks at A in Fig. 9 are, in fact, elongated towards the projection of $\{1\frac{1}{2}0\}$ spots and have the shape outlined by dotted lines in Fig. 5b. Thus, the diffuse D1a peaks are not isolated from the diffuse $\{1\frac{1}{2}0\}$ s.r.o. maxima, but merge together with them. The diffuse scattering (Fig. 9) near 'B' is different from that at 'A' and has two wings on either side (marked by arrows) that extend towards the positions of the Ni_2Mo spots [Fig. 5b]. This shows that in addition to the diffuse scattering near D1a positions, there must be scattering near Ni_2Mo positions. This has never been reported before. This was further confirmed by examining a [110] section [Fig. 10] which contains only the Ni_2Mo spots and no $\{1\frac{1}{2}0\}$ s.r.o. or D1a spots. The arrows in Fig. 10a point to the weak peaks that appear at the Ni_2Mo positions as indexed in Fig. 10b. It must be pointed out that the detection of such weak peaks depends very much on the exposure time. In the underexposed plates these may be missed altogether, and the present investigation exposure times up to 10 minutes (with a well-defocussed second condensor lens) were necessary to bring out the details. The reason the X-ray results (Fig. 7) do not show any diffuse scattering near the D1a positions is not quite clear at present, but could be due to inadequate X-ray counter

resolution. Thus, in the quenched state Ni_4Mo samples exhibit weak scattering near D1a and Ni_2Mo superlattice positions coexisting with much stronger scattering at $\{1\frac{1}{2}0\}$. The scattering at D1a and Ni_2Mo positions are not isolated peaks but emerge from the $\{1\frac{1}{2}0\}$ peaks that lie close to it.

3.1.2. <u>Ni_3Mo</u>: The equilibrium ℓro structure of Ni_3Mo has been determined by Saito and Beck[17] to be orthorhombic and isotypic with that of ordered Cu_3Ti (space group - D_{2h}^{13} - Pmmm). The stoichiometric Ni_3Mo also does not have a true T_c and decomposes peritectoidally at 910°C to α + NiMo (Fig. 2) and is disordered f.c.c. at high temperatures in the single phase region. On fast quenching from the single phase region the decomposition to Ni-Mo can be suppressed. It has been mentioned[14,18] that the s.r.o. state of Ni_3Mo is similar to that of Ni_4Mo, but no detailed study as to whether any weak superlattice peaks are present or not has been done. During the isothermal annealing the Ni_4Mo and Ni_2Mo phases appear as metastable phases at an early stage and finally the equilibrium Ni_3Mo forms. Thus, it would be interesting to see whether any weak superlattice spots are present in the s.r.o. state or not and if so of what type.

Figure 11a shows a [001] diffraction pattern of Ni_3Mo quenched into iced brine from 1270°C. This pattern is similar to that of Ni_4Mo (Fig. 6). Here the diffuse scattering appears to extend from one $\{1\frac{1}{2}0\}$ position to the neighboring ones in the form of an arc, that passes through the Ni_2Mo position. This means that the diffuse scattering near Ni_2Mo position may be more prominent in Ni_3Mo than in Ni_4Mo. The fact that this is so can be seen by comparing the

[110] section of Fig. 11b with Fig. 10a where only Ni_2Mo spots are present. The [$\bar{1}$30] diffraction pattern (Fig. 11c) of Ni_3Mo is also similar to that of Ni_4Mo (Fig. 9). Here also the diffuse scattering at A is elongated towards the projection of $\{1\frac{1}{2}0\}$ s.r.o. spot and that at B is smeared out towards the neighboring Ni_2Mo positions. In all the sections examined no evidence for diffuse scattering near Ni_3Mo positions was obtained. Thus the quenched state of Ni_3Mo is similar to that of Ni_4Mo and there is weak scattering present near the superlattice positions corresponding to the Dla and Ni_2Mo structures in addition to the $\{1\frac{1}{2}0\}$ peaks. Although it may be surprising that stoichiometric Ni_3Mo does not show Ni_3Mo superlattice spots but rather Ni_2Mo and Ni_4Mo superlattice spots, the reason this may be so will be discussed later. Hence, in the Ni-Mo system as the stoichiometry changes from Ni_4Mo to Ni_3Mo the diffraction patterns of the quenched samples do not change very much except on increased scattering near Ni_2Mo positions with increased Mo content.

Now the question arises as to whether these quenched samples represent the s.r.o. state above Tc or not. It is quite possible that some ℓ.r.o. might have been induced during the quench itself. In many ordering systems the development of ℓ.r.o. state is associated with the appearance of tweed contrast[19,20] in the images of quenched samples show that there is hardly any tweed contrast developed in Ni_4Mo (Fig. 12), whereas in Ni_3Mo there may be some weak tweed contrast (FIg. 13). The different images were taken with different $\vec{g}$ vectors operating in order to distinguish the tweed contrast from the surface roughness. The weak tweed contrast observed in Fig. 13 for Ni_3Mo

could be due to the small amount of ordering induced because of quenching from a higher temperature of 1270°C. At higher temperatures the equilibrium concentration of vacancies will be higher which may aid in enhancing ordering during the quench. Even though there is a slight increase in the degree of order in Ni_3Mo compared to Ni_4Mo, the diffraction patterns are basically the same. Thus, we believe that in the s.r.o. state these Ni-Mo alloys do contain weak scattering near Ni_4Mo and Ni_2Mo superlattice positions. This will be further supported by the results to be discussed in the next section. In fact, to prove conclusively that these weak superlattice reflections are present in the s.r.o. state it is necessary to examine at temperature diffraction patterns. In the Ni-Mo system, since the disordering temperatures are rather high, at temperature electron diffraction studies are not very helpful because of the excessive thermal diffuse scattering. Thus, the Au-Cr and Au-Mn systems that have relatively lower T_c were chosen for high temperature electron diffraction studies, to see whether there are any weak superlattice reflections co-existing with $\{1\frac{1}{2}0\}$ maxima.

3.1.3. <u>Au_3Cr</u>: The equilibrium ℓ.r.o. structure of Au_3Cr is not definitely known and the phase diagram of Au-Cr system shows (Fig. 14) that an ordered phase may be present below ~330°C. However, it has been established[3] that in thin films it transforms to Dla superstructure. Current experiments on bulk alloys show that the ℓ.r.o. structure is not Dla but the exact structure has not been identified yet.[21] Thus, the thin film and the bulk alloy may behave differently similar to Au_3Mn.[22] In the present study s.r.o. state was studied both in the

thin films and in the bulk alloys. Since the important crystallographic features of Dla structure have been described earlier, they need not be repeated here.

Figure 15a and b show the [001] and [$\bar{1}$30] diffraction patterns respectively, obtained from a thin film of Au_3Cr, after aging for 67 hours at 270°C. The patterns consist of superlattice reflections due to Dla structure (see Fig. 5), together with the weak spots that are due to the double diffraction. The spots marked 'T' in Fig. 15b are due to the fine {111} f.c.c. twins that are invariably present in such epitaxially grown thin films. As the ordered structure was heated the Dla spots suddenly became weak and the $\{1\frac{1}{2}0\}$ s.r.o. spots appeared around 330°C. This temperature is the same as that reported by Tanner et al.[3] for Au_3Cr. This critical temperature was a good check on the composition of the thin film as mentioned earlier. Figure 16a shows a [001] diffraction pattern obtained after holding for 30 minutes at 330°C $\pm$ 10°C. Diffuse peaks can be seen at $\{1\frac{1}{2}0\}$ positions. Accurate measurements of the size and shape of $\{1\frac{1}{2}0\}$ spots on enlarged prints show that it is triangular shaped with the edges extending towards the neighboring Dla superlattice positions. In fact the area of the triangle covers almost the entire area outlined by the dotted lines in Fig. 5a. Figure 16b shows a [$\bar{1}$30] pattern taken at 370°C. Similar to the case of Ni_4Mo, here also the observed diffuse peaks (marked by arrows) are not entirely due to the weak Dla spots but are elongated towards the projection of $\{1\frac{1}{2}0\}$ spots and have the shape outlined by dotted lines in Fig. 5b. So here again the diffuse Dla peaks are not isolated from the diffuse $\{1\frac{1}{2}0\}$ maxima, but merge

together with them. This gives rise to a tetrahedral distribution of the diffuse s.r.o. scattering centered about the $\{1\frac{1}{2}0\}$, but enveloping the D1a positions.

It has been reported[3] that the ordering reaction in bulk Au_3Cr is very sluggish and does not show any evidence of ℓ.r.o. even after annealing for 550 hours at 270°C. Thus, on fast quenching from above Tc it should be possible to retain the s.r.o. state without inducing any ℓ.r.o. In order to check this and also to compare the high temperature results described above on thin films with that of the bulk, samples of Au_3Cr were quenched from various temperatures above Tc. Figure 17a and b show [001] and $[\bar{1}30]$ diffraction patterns respectively obtained on specimens that were water quenched from 550°C. These patterns are very similar to the high temperature electron diffraction patterns shown in Fig. 16. The $\{1\frac{1}{2}0\}$ spots in the quenched samples (Fig. 17a) are sharper compared to the at temperature diffraction patterns (Fig. 16a), but the shape remains more or less the same. The $[\bar{1}30]$ pattern (Fig. 17b) is also identical to the high temperature pattern shown in Fig. 16b. Here again the diffuse peaks near D1a positions elongate towards the $\{1\frac{1}{2}0\}$ spots. In addition to the diffuse peaks there are extra spots due to relrods from the (111) and (200) reciprocal lattice points above and below this section.

In order to arrive conclusively at the shape of the $\{1\frac{1}{2}0\}$ spots some other reciprocal lattice sections were also examined. Figure 18a shows a [121] pattern, that has been indexed in Fig. 18b. The symbols used in indexing are the same as in Fig. 5. The D1a positions marked 3 and 4 in Fig. 18b are especially important in determining the shape

of $\{1\frac{1}{2}0\}$ spots. Diffuse peaks can be observed near these and its equivalent positions. They are elongated in the <210> directions shown by the full and dotted lines on the indexed pattern and are shifted in the direction of the arrows shown, which point towards the projection of the $\{1\frac{1}{2}0\}$ spots. The diffuse scattering near the Dla positions such as 1 and 2 are difficult to distinguish from the broad diffuse $\{1\frac{1}{2}0\}$ spot that lies very close to it. Based on the information gathered above a three-dimensional reciprocal lattice model of the s.r.o. state was constructed and Fig. 19a shows the intensity distribution around each $\{1\frac{1}{2}0\}$ position. It can be seen that each $\{1\frac{1}{2}0\}$ spot is stretched out into two triangular shaped sheets of intensity that are normal to each other. For comparison the three-dimensional reciprocal lattice of the fully ordered Dla structure is also shown in Fig. 19b. It is clear that the shapes of the $\{1\frac{1}{2}0\}$ s.r.o. spots have resulted from the presence of weak scattering near the four Dla positions surrounding it.

The comparison of these results of quenched bulk samples with that of the at temperature diffuse scattering results show that no ℓ.r.o. has been induced in Au_3Cr during the quench. The ordering reaction is so sluggish that even the thin films that were cooled from above Tc just by switching off the furnace show diffraction patterns that are no different from those obtained on quenched samples. Figure 20a and b show such diffraction patterns from a thin film cooled from 400°C, which are identical to those in Fig. 17 obtained from quenched bulk samples except the intensity of the $\{1\frac{1}{2}0\}$ spots may be slightly higher in the slowly cooled sample. These results conclusively show that weak scattering is present near the Dla

superlattice reflections in the s.r.o. state above Tc in Au_3Cr. On this basis it is quite reasonable to assume that in the Ni-Mo alloys also weak scattering is present near Dla and Ni_2Mo superlattice positions in the s.r.o. state above Tc. The fast quenching may have just slightly enhanced their intensities.

3.1.4. <u>Au_4Cr</u>: The equilibrium ℓ.r.o. structure of Au_4Cr has been established[23] to be Dla and on heating it disorderes to f.c.c. structure around 325°C (Fig. 14). To the author's knowledge there has been no report of the study of the s.r.o. state above Tc, but one would expect it to behave similar to the system Au_3Cr. In order to see if they exhibit diffuse scattering centered around $\{1\frac{1}{2}0\}$ positions, similar to that of Au_3Cr, thin films of Au_4Cr were examined above Tc. In the fully ordered state the diffraction patterns were identical to those in Fig. 15. On heating to a temperature above Tc (~325°C) the Dla superlattice spots vanished and were replaced by diffuse $\{1\frac{1}{2}0\}$ spots. Figure 21 shows a [001] diffraction pattern taken at 340°C. This pattern is identical to the at temperature diffraction pattern of Au_3Cr shown in Fig. 16a. The triangular shape of the $\{1\frac{1}{2}0\}$ spots extending towards the Dla positions can be clearly seen. Examination of other reciprocal lattice sections also showed that the shapes of the diffuse $\{1\frac{1}{2}0\}$ spots in Au_4Cr are identical to that of Au_3Cr and shows diffuse scattering near Dla positions.

Thus, like the Ni-Mo alloys where both Ni_3Mo and Ni_4Mo are similar in s.r.o. state, the Au_3Cr and Au_4Cr alloys are similar in the s.r.o. state although the ℓ.r.o. structure of Au_3Cr in bulk alloys may be different.

3.1.5. Au$_4$V: The alloy Au$_4$V also possesses D1a structure[23] in the ℓro state and this structure exists over a composition range as can be seen in the phase diagram in Fig. 22. The stoichiometric Au$_4$V has a critical temperature of 565°C and is fcc above T_c. So far there has been no report of the electron diffraction study of order-disorder transformation in this system. Since this system is isostructural with Ni$_4$Mo and Au$_4$Cr it would be interesting whether it behaves similarly in the sro state or not. In other words whether it exhibits diffuse sro peaks at $\{1\frac{1}{2}0\}$ positions and whether there are any weak superlattice reflections present or not. Figure 23 shows a [001] electron diffraction pattern of a bulk sample quenched in iced brine from 900°C. Weak peaks can be observed in this pattern at $\{1\frac{1}{2}0\}$ positions (marked by arrows). There is an enchanced scattering of each $\{1\frac{1}{2}0\}$ spot towards the neighboring D1a positions. As a matter of fact the diffuse intensity extends beyond the D1a position towards the fundamental fcc spots. Examination of other reciprocal lattice sections such as [121] and [$\bar{1}$30] is consistent with this observation. The reason for this is not quite clear at present, but in any case the important observation is that diffuse scattering is present near the D1a positions. Although no diffraction patterns were examined at temperatures above T_c, comparison with the results on Au$_3$Cr suggests that the quenched state represents the sro state above T_c, fairly well in this alloy. Thus the sro state in this alloy is very similar to that in the Au-Cr alloys.

3.1.6. Au$_3$Mn: The system Au$_3$Mn shows a DO$_{22}$ structure [also described as a long period superlattice of the type L1$_2$ (M=1) i.e. an antiphase derivative of Cu$_3$Au structure where an APB is introduced at every unit

cell] with long period stacking modulations, in the bulk material[22] and in thin films it has a two-dimensional long period superstructure analyzed by Watanabe.[24] The alloy Au_4Mn shows Dla structure both in the thin films[25] and in bulk.[22] In addition to these two a number of other structures have been found[22,26] in between Au_3Mn and Au_4Mn. Figure 24 shows the Au-rich portion of the Au-Mn phase diagram. The hexagonal of phase occurs[26] at 23.8%Mn, and the α'' phase has the Watanabe type two-dimensional long period superstructure.[27] In addition to these Morris et al.[28] reported two complicated structures Au_3MnI, an orthorhombic metastable phase, and Au_3MnII, a tetragonal phase, at the stoichiometric Au_3Mn composition, depending on the heat treatment conditions. Thus in this narrow composition range between Au_3Mn and Au_4Mn at least six different structures exist at various composition and temperature ranges. This makes this system very interesting for sro study, in order to see whether the diffuse scattering above T_c shows any evidence for the presence of weak superlattice reflections corresponding to any of the complicated ordered structures observed below T_c.

Figure 25(a) shows a [001] diffraction pattern from an evaporated thin film of Au_3Mn showing only the Watanabe type two-dimensional long period superlattice and Fig. 25(b) shows a similar pattern butcontaining additional Dla spots, indicating a mixture of Au_4Mn and Watanabe type Au_3Mn. As mentioned earlier the structure of these Au-Mn alloys is very sensitive to composition and depending on composition it is possible to get a mixture of both Dla and Watanbe type two-dimensional long period superlattice structures. In the present case since the composition of the thin films are unknown it is quite likely that the film corresponding to Fig. 25(b) has a different composition than the film corresponding

to Fig. 25(a). The [001] reciprocal lattice section corresponding to the Watanabe type structure is shown in Fig. 25(c), where the filled small circles are the superlattice spots corresponding to the two-dimensional long period superlattice with periodicites m_1 $(= \frac{a^*_1}{M_1})$ and m_2 $(= \frac{a^*_2}{M_2})$. Here a^*_1 and a^*_2 refer to the reciprocal lattice vectors and M_1 and M_2 correspond to the periodicities in real space in a_1 and a_2 directions respectively. That is, in real space the periodic APB's occur at every M_1 and M_2 unit cells in the a_1 and a_2 directions respectively. The values of M_1 and M_2 measured from the diffraction patterns were found to be 1·2 and 2·3 respectively, which are close to those obtained by Watanbe.[24] The occurrence of these superlattice reflections in the two-dimensional long period superstructures and the significance of non-integral periodicities have been reviewed by Sato and Toth[29] and need not be discussed here. In addition to the superlattice reflections there are weak satellites present (marked by small open circles) which are thought[24] to arise from the lattice modulations such as variation in lattice spacing or scattering factor and hence have the same periodicity of the APB's. Figure 25(b) shows some additional streaks joining pairs of superlattice spots, such as A and B [Fig. 25(c)], the origin of which is not quite clear at present.

In order to examine the sro state, the two different kinds of ordered states, one containing the two-dimensional lng period superlattice [Fig 25(a)] and the other a mixture of Dla and Watanbe type structure [Fig. 25(b)] were heated above T_c to examine the differences in the diffuse scattering behaviors, if there is any. During heating it was observed that the Dla spots disappeared completely around 450°C and only the Watanabe type structure remained and Fig. 26(a) shows a diffraction

pattern taken at 450°C. This pattern corresponds to the film that contained a mixture of Dla and Watanabe type structure in the ordered state before heating [Fig. 25(b)]. The streaks are still present at this temperature. On further heating to 475°C all the sharp superlattice reflections vanished and were replaced by diffuse scattering around $\{1\frac{1}{2}0\}$ positions and Fig. 26(b) shows the pattern taken at 500°C. The samples containing only the Watanbe type ordered structure, such as in Fig. 25(a), showed diffraction patterns above T_c that were identical to Fig. 26(b). Thus the sro state above T_c in these samples containing different initial ordered structures are identical. Although the actual composition of these films are unknown the low T_c(~475°C) suggests that the composition is closer to Au_4Mn than Au_3Mn. It can be seen from Fig. 26(b) that the diffuse intensity is not so much concentrated around $\{1\frac{1}{2}0\}$ as was observed in Au-Cr and Ni-Mo alloys, but is fairly spread out in the <100> directions. Measurements show that the diffuse intensity extends from the superlattice position marked P [Fig. 25(c)] to that marked Q, which shows that there is diffuse scattering present near most of the superlattice reflections in Fig. 25(c), except those near A and C and their equivalent positions. If there is any scattering present near A and C it must be very weak. The shape of the diffuse scattering is quite different from that of Au_3Cr and shows no enhanced scattering towards the Dla positions. There is also no diffuse scattering observed near the satellite positions of Fig. 25(c).

Thus the diffuse scattering results above T_c in thin films of Au-Mn alloys of compositions between 20-25 at%Mn show the presence of weak scattering near most of the superlattice reflections of the Watanabe type two-dimensional long period superstructure.

3.2. Development of L.R.O. in Ni-Mo Alloys: As mentioned earlier, the diffraction and microstructural studies at the very early stages of the development of ℓro are very helpful in understanding the sro state. In this study the detailed study of the development of ℓro was restricted to Ni-Mo alloys, as this system is particularly interesting because of the discovery of weak Ni_2Mo superlattice reflections in the sro state, both in Ni_3Mo and in Ni_4Mo.

3.2.1. Ni_3Mo: The isothermal aging studies of Ni_3Mo were carried out at 650°C and all the results to be described below correspond to various aging times at this temperature. The choice of this temperature is based on previous studies on Ni_4Mo,[8] which indicate that aging at 650°C is associated with some interesting diffraction effects at the initial stages whereas ordering reaction at high temperatures (~750°C) is extremely fast and these diffraction effects are missed altogether.

The diffraction patterns and the microstructures of the as quenched alloy have been described earlier in Figs. 11 and 13. In the as quenched condition it was not possible to obtain any definite images by dark field imaging the $\{1\frac{1}{2}\,0\}$ spot. On aging for 30 mins. the $\{1\frac{1}{2}0\}$ spots become sharper as can be seen in the [121] diffraction pattern in Fig. 27(b). For the sake of comparison a similar diffraction from the as quenched alloy is shown in Fig. 27(a). In addition to the sharpening of $\{1\frac{1}{2}0\}$ spots, pronounced diffuse streaks can be seen in the $\langle 210 \rangle$ directions. The $\{1\frac{1}{2}0\}$ spots still exist after aging for 1 hour. At this stage, it is possible to obtain definite dark field images of the $\{1\frac{1}{2}0\}$ spots

and Fig. 28(a) shows a dark field micrograph of the $\{1\frac{1}{2}0\}$ spot encircled in the diffraction pattern in Fig. 28(b). The orientation of the foil is $[1\bar{2}0]$. The microdomains are about 30-40Å in diameter and appear as a random array. It can be seen from the diffraction pattern that the $\{1\frac{1}{2}0\}$ spots are associated with diffuse streaks similar to that observed after 30 mins. of aging in [121] pattern [Fig. 27(b)]. The dark field image of $\{1\frac{1}{2}0\}$ spot in Ni_3Mo in Fig. 28(a) is similar to that obtained by Ruedl et al.[9] in quenched Ni_4Mo. In the present study on Ni_3Mo and in the previous study on Ni_4Mo,[8] it was not possible to obtain definite dark field images of the microdomains using the $\{1\frac{1}{2}0\}$ spots in the quenched condition. This implies that in the quenched condition the degree of order within these microdomains is very small and on aging for short time the $\{1\frac{1}{2}0\}$ spots become a little sharper as the degree of order increases. The microdomains observed by Ruedl et al. in quenched Ni_4Mo could have been due to a slower quench in their samples compared to those employed in the present study. Nevertheless, the fact is that microdomains are visible in the dark field micrographs of $\{1\frac{1}{2}0\}$ spots, when the superlattice reflections are still very diffuse and weak, even though it is quite likely that a part of the diffuse streak may also contribute to the dark field image. It is to be noted that at this stage the microdomains do not have a well-defined shape and have a rather diffuse boundary.

On prolonged aging the $\{1\frac{1}{2}0\}$ spots disappear and the Ni_2Mo and Ni_4Mo superlattice spots become stronger. Figure 29(a) shows a [001]

diffraction pattern obtained after aging for 4 hours. The pattern consists of superlattice reflections from both Ni_2Mo and Ni_4Mo phases as indexed in Fig. 29(c). The Ni_2Mo reflections appear to be arced towards the neighboring Ni_4Mo reflections with the main direction of streaking being <110>, whereas the Ni_4Mo reflections are streaked in <210> directions. The streaking of Ni_4Mo spots, in this case after 4 hrs. of aging, is similar to that obtained by Okamoto and Thomas[8] in Ni_4Mo after 5-10 mins. of aging at the same temperature, implying a slower kinetics for the decomposition of Ni_3Mo compared to that of Ni_4Mo at 650°C. There is also some intensity that appears to be present near the $\{1\frac{1}{2}0\}$ positions (marked by arrows) and is elongated in <100> directions. This intensity is not due to the presence of $\{1\frac{1}{2}0\}$ spots (as they do not lie precisely at $\{1\frac{1}{2}0\}$ positions) but arises from the relrods from the other two NI_4Mo spots that are also streaked in <210> directions and lie at positions $\frac{1}{10}[002]$ above and below this [001] reciprocal lattice section [see Fig. 5(a)]. Thus, they extend from $\{1\frac{1}{2}0\}$ position to the projection of the Ni_4Mo spots, along <100> directions. On further aging the Ni_4Mo spots become rounded as can be seen in Fig. 29(b), whereas the Ni_2Mo spots are still arced. The previous study on Ni_4Mo has shown that the streaking of Ni_4Mo superlattice spots in <210> directions is not a shape factor effect because the streaking is asymmetrical and the dark field images show equiaxed domains. This streaking of D1a spots in <210> directions was explained to be due to the presence of non-conservative APB's on {420} planes. If the

APB's are spaced periodically then one would observe satellites, as mentioned before for Au_3Mn structure, but if the spacing is irregular these satellites will be broadened into streaks. On aging for longer times, when these non-conservative APB's, which have a relatively higher energy than the conservative APB's, are eliminated and the streaks will disappear as seen in Fig. 29(b). However, some of them may still remain and it will be seen later that they give rise to very weak streaks. Although the Ni_4Mo spots are not streaked after aging for 49 hrs. [Fig. 29(b)] the Ni_2Mo spots are still streaked. This makes it doubtful whether an explanation based on APB's, similar to that of Ni_4Mo can be applied to Ni_2Mo or not. In order to see the actual reason for the arcing of Ni_2Mo spots and to determine their true shape several other reciprocal lattice sections were examined for various aging treatments. Figures 30 and 31 show $[1\bar{2}0]$ and [121] reciprocal lattice respectively. It can be seen from Fig. 30(a) that the Ni_2Mo spots [as indexed in Fig. 30(c)] are streaked along <210> direction and not along <110> as was apparent from the [001] pattern. A dark field micrograph of the Ni_2Mo spot [as shown by the position of the objective aperture in Fig. 30(a)] reveals that the Ni_2Mo domains have a plate-like shape forming on (420) plane. Thus, the streaking of Ni_2Mo spots in <210> directions is a true shape factor effect due to plate-like domains. The $[1\bar{2}0]$ diffraction pattern in Fig. 30(a) also contains some additional relrods from the Ni_4Mo spots whose positions are shown in Fig. 30(c) by open squares. Their intensities are fairly

strong because they lie very close to this section and are still elongated. The [$\bar{1}$21] sections (Fig. 31) further confirm that the Ni_2Mo spots are streaked along <210> directions. Figures 31(a) and (b) show the diffraction patterns after 4 hrs. and 14 hrs. of aging respectively. Out of the three variants of Ni_2Mo that are present, each one is streaked in different <210> directions. The variant marked by open triangle [Fig. 31(c)] is streaked in a <210> direction that intersects the [$\bar{1}$21] section at an angle and so this spot appears slightly elliptical [Fig. 31(a)]. In fact, the streaks in the <210> directions appear to extend continuously from one reciprocal lattice point to another [Fig. 31(b)] with maxima at Ni_2Mo and Ni_4Mo positions.

Now after establishing that the Ni_2Mo spots are streaked in <210> directions due to a shape factor effect we can examine why in the [001] diffraction pattern the streaking appears to be along <110>. It was mentioned earlier in Section 3.1.1 that the Ni_2Mo structure has a two-fold degeneracy with respect to stacking on {420} planes, for example, stacking on (420) and (240) gives rise to the same variant of Ni_2Mo [Spot 'A' in Fig. 29(c)]. Thus if plate-like Ni_2Mo domains form with equal probability on (420) and (240) planes the Ni_2Mo spot at 'A' will be streaked both in [420] and [240] directions, as shown by the thick lines [Fig. 29(c)]. Since these two directions are fairly close to each other and the streaks are fairly wide, these two streaks are not discernible from each other in [001] orientation and give rise to an apparent streak in <110> direction and an arcing towards the neighboring Ni_4Mo spots. However,

the $[1\bar{2}0]$ section contains only one direction of the streak as can be seen from the trace in Fig. 29(c) and it is possible to see that the Ni_2Mo spots are, in fact, streaked in <210> directions. Similar is the case with [121] orientation whose trace on [001] section is the same as that of $[1\bar{2}0]$. These results show that it is absolutely necessary to examine certain particular reciprocal lattice sections such as $[1\bar{2}0]$ and [121] in order to reveal the origin of the diffraction effects associated with Ni_2Mo spots, or else erroneous conclusions may be drawn.

The Ni_2Mo and Ni_4Mo phases appear to coexist for a long time and Fig. 32 shows the structure obtained after 163 hrs. of aging. Figure 32(a) and (b) show the dark field micrographs of Ni_2Mo and Ni_4Mo spots, marked A and B respectively in the corresponding diffraction pattern in Fig. 32(c). It can be seen that the Ni_2Mo particles are elongated normal to $[2\bar{1}0]$ direction [Fig. 32(a)], whereas the Ni_4Mo particles are more or less equiaxed. In Fig. 32(a) some Ni_4Mo particles are also imaged, because the Ni_4Mo spot lies very close to the Spot A. The diffraction pattern [Fig. 32(c)] shows that the Ni_2Mo spots are still fairly elongated along <210> directions and there is a weak streak running along <210> direction continuously from one superlattice reflection to the other. If this streak is due to a shape factor effect of the Ni_2Mo phase, this would mean that the Ni_2Mo domains are only a unit cell thick, whereas the dark field micrographs show much thicker domains. The origin of this streak

can be explained as due to the presence of APB's in Ni_4Mo which give rise to a monolayer thick Ni_2Mo. An antiphase boundary model that can account for this streaking as well as the results on Ni_4Mo to be described in next section will be presented later in Section 4.3.

On further aging the Ni_2Mo and Ni_4Mo phases disappear and the equilibrium Ni_3Mo phase appears. Figure 33 shows the fully ordered structure of Ni_3Mo obtained after aging for 244 hrs. Several thermal APB's can be seen in one single domain in the bright field micrograph in Fig. 33(a) and also in the corresponding dark field micrograph [Fig. 33(b)] of $(200)_{Ni_3Mo}$ superlattice reflection. The diffraction pattern from this area is very similar to that shown in Fig. 34(a). This shows a single domain of Ni_3Mo and no double diffraction spots are seen. The reflections obey the extinction rule that all reflections with $h + k = 2n + 1$ have zero structure factor and are absent. The orientation relationships between the $Ni_3Mo(\gamma)$ and fcc phase (f) can be derived as follows:

$$[100]_\gamma \;//\; [10\bar{1}]_f$$

$$[010]_\gamma \;//\; [1\bar{1}1]_f$$

$$[001]_\gamma \;//\; [121]_f$$

Thus, the stoichiometric Ni_3Mo first decomposes to two metastable phases Ni_2Mo and Ni_4Mo. In the initial stages of deocmposition the Ni_2Mo phase forms plate-like domains on {420} planes that give rise to pronounced streaking in the diffraction pattern, whereas the Ni_4Mo phase does not form plate-like domains but still shows streaking

in the diffraction patterns in <210> directions. At intermediate stage of aging the streaking of Ni_4Mo spots disappear, whereas those of Ni_2Mo spots remain. On prolonged aging both the metastable phases Ni_2Mo and Ni_4Mo are replaced by the equilibrium Ni_3Mo.

3.2.2. $\underline{Ni_4Mo}$: The previous study[8] on the initial stages of ordering shows that interesting diffraction effects are associated with short aging times (5 - 10 mins) at 650°C and so no attempt was made to repeat the previous observations. In this study main emphasis was on the microstructural characterization with respect to the presence or absence of Ni_2Mo pahse. Because the discovery of weak scattering near Ni_2Mo positions in the quenched samples, as discussed before, makes one suspicious that this phase may be present as a metastable phase, similar to the case of Ni_3Mo. The aging treatments were all done at 650°C, as before.

Figure 35 shows the microstructure after aging for 2 hrs. In Fig. 35(a) the typical tweed contrast, characteristic of the high volume fraction of misfit particles is seen. In this [012] foil, as seen from the corresponding diffraction pattern in Fig. 35(c), the directions of the situations appear to coincide with the projections of $(\bar{1}01)$ and $(\bar{1}10)$ planes respectively, similar to that observed in Cu-Be.[30] This type of contrast has been observed earlier in Ni_4Mo and has been found[8] to change contrast with the operating reflection, very similar to that of Cu-Be. Figure 35(b) shows the dark field micrograph of one variant of Ni_4Mo superlattice reflection, encircled in the diffraction

pattern of Fig. 35(e). The indexing of the diffraction pattern is the same as that in Fig. 30(e) and no Ni_2Mo spots are apparently visible. The dark field micrograph shows domains of about 70-80Å in diameter and it is interesting to note that these domains align up in a way that follows closely the contour of the tweed striations. The small arrows in Fig. 35(a) and (b) point to the identical positions in the image and it is seen that the domains of the particular variant that is imaged do not reverse contrast [Fig. 35(b)] exactly at the same position where the black tweed striation is in Fig. 35(a), but align up next to the tweed striation. This alignment of domains can be further seen at a later stage of aging and Fig. 36(a) and (b) show a bright and dark field pair obtained after aging for 8 hrs. The foil orientation is [121] and the corresponding diffraction pattern is shown in Fig. 36(d) where the foil has been slightly tilted from the strong two beam case in Fig. 36(a) to obtain this more symmetrical diffraction pattern. Here again the direction of the tweed striations [Fig. 36(a)] coincide with the trace of $(10\bar{1})$ plane. The dark field micrograph [Fig. 36(b)] of one variant of the Ni_4Mo superlattice reflection [marked 'B' in Fig. 36(d)] shows an alignment of the domains more or less in the direction of the tweed striations. Some typical areas are marked by arrows. These results show that the ordered domains are not in a random array of particles but are arranged in some ordered fashion in three dimensions. At this stage it is not possible to describe further the exact nature of the ordered array.

Figure 36(c) shows a [001] diffraction pattern containing two variants of Ni_4Mo superlattice reflections [see Fig. 29(e) for indexing]. In addition to the Ni_4Mo superlattice reflections there are also weak Ni_2Mo superlattice reflections present, as marked by the single arrows. This pattern is very similar to the pattern obtained from Ni_3Mo [Fig. 29(b)], except that Ni_2Mo reflections are very weak. Similar to the case of Ni_3Mo, the weak Ni_2Mo spots are arced towards the neighboring Ni_4Mo spots. There are also some relrods (marked by double arrows) from the Ni_4Mo spots that lie $\frac{1}{10}$[002] above and below this reicprocal lattice section. In the [121] diffraction pattern [Fig. 36(d)] it can be clearly seen that the different variants of the Ni_2Mo reflections are streaked in different <210> directions. The indexing of this pattern is similar to that in Fig. 31(c). Here the <210> streaks are elongated continuously from one superlattice reflection to another with a maxima at the Ni_2Mo position, similar to the weak <210> streak observed in Ni_3Mo at a later stage of aging (Figs. 31 and 32). This means that the Ni_2Mo phase exists as very thin platelets whose thickness is of the order of a unit cell. There are also some weak double diffraction spots present (marked by double arrows), from the different variants of the Ni_4Mo reflections. It must be pointed out that the detection of these weak spots depends very much on the exposure time, foil contamination, etc. In relatively thicker foils, these weak spots are difficult to detect at 100 kV because of the presence of the Kikuchi

lines or bands. The presence of the Ni_2Mo superlattice reflections was also detected at other aging treatments at 650°C, and Fig. 37 shows the diffraction patterns from two extreme conditions. At the early stage of aging [Fig. 37(a)] the diffuse streak in the <210> direction is present, which passes through the Ni_2Mo position, but the Ni_2Mo peak is not so distinct. At the intermediate stage (shown earlier in Fig. 36) the Ni_2Mo peaks are clearly recognizable and on prolonged aging up to 24 hrs. these Ni_2Mo peaks in the <210> streaks do not grow into sharp superlattice reflections and the pattern remains essentially unchanged, as seen in the [121] pattern in Fig. 37(b). This pattern is slightly underexposed, but still the <210> streaks can be seen and the Ni_2Mo peaks can be clearly seen on the negative. Figure 37(e) shows a $[1\bar{2}0]$ pattern after 24 hrs. of aging, which is very similar to Fig. 30(a) and here also the Ni_2Mo peaks (marked by arrows) can be seen. Since these 210 streaks through the Ni_2Mo reflections do not vanish even after aging for 24 hrs., it implies that the Ni_2Mo phase does not grow beyond a thickness of a few atom layers. It will be shown later in Section 4.3 that this monolayer thick Ni_2Mo phase arises from the presence of nonconservative APB's on $\{420\}$ planes in Ni_4Mo phase.

Aging treatments beyond 24 hrs. is dominated by the heterogeneous reaction at the grain boundaries and Fig. 38 shows an example. The heterogeneous reaction starts at the grain boundary and advances into the next grain (D). The structure inside the heterogeneous

component (c) contains a dense array of dislocations and APB's. The dislocation pile ups in grain D indicate the stress field ahead of the migrating interface. It is interesting to note that this heterogeneous reaction does not start at the twin boundary as seen in Fig. 38(b). Here, the lower grain 1 is in $[1\bar{1}0]$ orientation, whereas the upper grain 2 is in [114] orientation and the heterogeneous component is migrating into grain 2, but there is no heterogeneous component at the twin boundary marked 'T.' The tweed contrast is seen in grain 1 where a strong [220] beam is operating. In these heterogeneously decomposed areas neither the <210> streaks nor any evidence for Ni_2Mo phase was obtained. Similar heterogeneous reaction mode has been observed in Ni_2V [31] and it has been found that this heterogeneous reaction at the grain boundary is the predominant decomposition mode at lower temperatures. In Ni_4Mo aged at 650°C, the heterogeneous decomposition mode becomes predominant only after 24 hrs. and until then the domains grow to a size of about 100Å and also the degree of order within these domains increases. On the other hand this heterogeneous decomposition was not observed in Ni_3Mo until 163 hrs. of aging at the same temperature of 650°C and after 244 hrs. fully ordered Ni_3Mo was obtained. It is possible that the Ni_3Mo phase heterogeneously nucleated at grain boundaries and migrated into the matrix containing Ni_2Mo and Ni_4Mo phases.

The important observation on Ni_4Mo is the presence of weak superlattice reflections corresponding to Ni_2Mo phase. The pronounced

streaking of Ni_2Mo reflections in <210> directions imply that this phase arises from the presence of non conservative APB's on $\{420\}$ planes of Ni_4Mo domains. At a later stage of aging heterogeneous reaction starts at the grain boundary and this heterogeneously nucleated phase migrates from the grain boundary into the whole grain. There is no Ni_2Mo phase present in the final equilibrium Ni_4Mo phase.

3.3. Summary of Experimental Results: The most important results of this investigation can be summarized as follows:

(a) In the Au-Cr alloys, in addition to the $\{1\frac{1}{2}0\}$ sro peaks, diffuse superlattice reflections corresponding to Dla structure are observed both in the as quenched state and at temperatures above T_c.

(b) The Au_4V system shows diffuse scattering near $\{1\frac{1}{2}0\}$ as well as Dla positions in the as quenched state.

(c) At temperatures above T_c the diffuse $\{1\frac{1}{2}0\}$ peaks in Au-Mn alloys appear to extend to most of the superlattice reflections of the two dimensional long period superlattice of Au_3Mn.

(d) The as quenched Ni-Mo alloys show weak peaks at Ni_2Mo positions, in addition to the Dla and $\{1\frac{1}{2}0\}$ peaks.

(e) The stoichiometric Ni_3Mo first decomposes to metastable Ni_2Mo and Ni_4Mo phases. The Ni_2Mo phase forms as plate-like domains on $\{420\}$ planes but the Ni_4Mo does not. On prolonged aging both Ni_2Mo and Ni_4Mo phases are replaced by Ni_3Mo.

(f) The stoichiometric Ni_4Mo also shows the presence of a small amount of Ni_2Mo domains. At a later stage of aging at 650°C heterogeneous reaction takes over and no Ni_2Mo phase is present.

IV. DISCUSSION

The results of the sro alloys presented above show conclusively that in the systems that exhibit diffuse $\{1\frac{1}{2}0\}$ sro peaks, there is additional weak scattering present near the superlattice reflections. These superlattice reflections are not isolated from the $\{1\frac{1}{2}0\}$ peaks but merge with the neighboring $\{1\frac{1}{2}0\}$ peaks. The superlattice reflections that are observed in the sro state in a particular alloy correspond to one or more of the ro phases that appear in that system, although they may or may not be the equilibrium ℓro structure at that particular composition. For example in the Ni-Mo alloys weak scattering is observed near Ni_4Mo and Ni_2Mo superlattice positions both of which appear at some stage or other in the ℓro state. In Au-Cr and Au-V alloys weak scattering appears near Dla positions which is also the structure in the ro state. In thin films of Au-Mn alloys diffuse scattering appears near Watanabe type superlattice positions which is also one of the structures that are observed in the ro state in that composition range. Thus, in different systems the $\{1\frac{1}{2}0\}$ peak assumes different shapes, so as to give rise to scattering near these various superlattice positions. Now, first an attempt will be made to account for the various shapes of these diffuse $\{1\frac{1}{2}0\}$ spots by using the statistical thermodynamic model of Clapp and Moss.[5] It will be shown that this model in its present form is unable to account for all the features of the observed diffuse scattering and then it will be examined whether the structural interpretation of the sro state can

explain the observed shapes or not. The occurrence of the Ni_2Mo phase in stoichiometric Ni_3Mo and Ni_4Mo alloys will be justified thermodynamically and also interms of a structural model.

4.1. Statistical Thermodynamic Model of SRO: In the high temperature approximation of the statistical thermodynamic model developed by Clapp and Moss, the diffuse intensity, $I(\vec{k})$ at any reciprocal lattice point, $\vec{k}$, can be written as

$$I(\vec{k}) = C \left[1 - \frac{T_c}{T} \cdot \frac{V(\vec{k})}{V(\vec{k}_m)} \right]^{-1}$$

where C is a normalization constant, T_c is the critical temperature for order-disorder transition, T is any temperature above T_c where the diffuse scattering is measured, and $V(\vec{k})$ is the Fourier transform of the pairwise interaction potential. For a fcc crystal, considering the interaction potentials Vi's only up to third nearest neighbors $V(\vec{k})$ can be written as,

$$\begin{aligned} V(k) = {} & 4V_1 \left[\cos \pi h_1, \cos \pi h_2 + \cos \pi h_2 \cos \pi h_3 + \cos \pi h_3 \cos \pi h_1\right] \\ & + 2V_2 \left[\cos 2\pi h_1 + \cos 2\pi h_2 + \cos 2\pi h_3\right] \\ & + 8V_3 \left[\cos 2\pi h_1 \cos \pi h_2 \cos \pi h_3 + \cos \pi h_1 \cos 2\pi h_2 \cos \pi h_3 \right. \\ & \left. + \cos \pi h_2 \cos 2\pi h_3\right] \end{aligned}$$

where $\{h_1, h_2, h_3\}$ are continuous variables in reciprocal space. $V(\vec{k}_m)$ corresponds to the value of $V(\vec{k})$ at that position in reciprocal lattice, $\vec{k}_m$, where it takes an absolute minimum value. The intensity $I(\vec{k})$ has a peak where $V(\vec{k})$ goes to a minimum and in the present case, since we

are concerned with the diffuse peaks at $\{1\frac{1}{2}0\}$ positions, the value of $V(k_m)$ is the value at $h_1 = 1$, $h_2 = \frac{1}{2}$, $h_3 = 0$. Now using equation (1) we can calculate the diffuse intensity at any point in reciprocal space for various values of the ratios $\frac{V_2}{V_1}$ and $\frac{V_3}{V_1}$ and then plot out isointensity contours. The limits over which the ratios $\frac{V_2}{V_1}$ and $\frac{V_3}{V_1}$ can be varied for the minima of $V(k)$ to occur at $\{1\frac{1}{2}0\}$ have been calculated by Clapp and Moss[5] and is shown in Fig. 39. A computer program was written to plot out the isointensity contours for [001] reciprocal lattice section with $\frac{T_c}{T}$, $\frac{V_2}{V_1}$ and $\frac{V_3}{V_1}$ as the variable parameters. Iso-intensity contour maps were plotted for all possible values of the ratios $\frac{V_2}{V_1}$ and $\frac{V_3}{V_1}$ within the enclosed triangle in Fig. 39, keeping a constant $\frac{T_c}{T} = 0.95$ close to the experimental value. No matter what values of the ratios of the interaction parameters were chosen, it was not possible to match the computed shape with the tetrahedral shape of $\{1\frac{1}{2}0\}$ sro spots in Au-Cr alloys [Fig. 19(a)] and also in Au_4V. In the case of Ni_4Mo, Clapp and Moss tried to match the computed curves with the X-ray results of Spruiell and Stansbury [Fig. 7] and obtained a good agreement. But as pointed out earlier, the X-ray results failed to detect any scattering near D1a positions and so also the computed curves. Similar attempts were made to obtain a match for Ni_3Mo and Fig. 40 shows the best possible match with that of Fig. 11(a), by using $\frac{T_c}{T} = 0.95$, $\frac{V_2}{V_1} = 0.4$ and $\frac{V_3}{V_1} = 0.00$. The intensities are in relative units. Here, although the diffuse scattering near Ni_2Mo positions is reproduced well in the computed curve, it is still not

possible to obtain any scattering near Dla positions. Thus, by using only the first three nearest neighbor interaction parameters V_1, V_2 and V_3 it is not possible to account for the diffuse scattering that is present near the Dla positions in the sro state in several alloys. It may be necessary to incorporate higher neighbor (>3) interaction parameters in order to fully account for the shapes of $\{1\frac{1}{2}0\}$ sro diffuse scattering, which implies that long range inter-atomic interactions are necessary.

The shape of the $\{1\frac{1}{2}0\}$ spot in Au_3Mn [Fig. 26(b)] is quite different from other systems and is in the form of a cigar elongated along 100 . The theoretical diffuse scattering map obtained by Moss and Clapp[6] for Au_3Mn using $\frac{V_2}{V_1} = +0.08$ does not match very well with our experimental result. A better match was obtained by using a large negative $\frac{V_2}{V_1} = -0.7$ and $\frac{V_3}{V_1} = -0.2$ as shown in Fig. 41. On the basis of this agreement between theoretical and experimental shape of $\{1\frac{1}{2}0\}$ spots in Au_3Mn and the apparent agreement in Ni_4Mo Clapp and Moss ruled out the microdomain concept of sro for these alloys, and said that the sro state can be best described by the statistical theory. The present results show that the theory fails to explain the sro state in Au_3Cr, Au_4Cr, Au_4V and the fine features of the diffuse scattering in Ni-Mo alloys. This theory also fails to explain some of the features of the diffuse scattering observed in Cu-Au alloys in the sro state. For example the weak splitting observed in the diffuse scattering in Cu_3Au,[32,33] in CuAu[34] and in $CuAu_3$[35]

above T_c cannot be reproduced from the theoretical calculations from this model. In the following section it will be shown that the structural model can account for the observed results and at the same time gives a better physical description of the sro state than the statistical theory.

4.2. Structural Interpretation of the SRO State: Any structural model for the sro state in the systems investigated has to account for the presence of all the weak superlattice reflections observed and the $1\frac{1}{2}0$ spot. There are two structures, namely the DO_{22} and Ll_0 (M = 1) that give rise to superlattice reflections at $\{1\frac{1}{2}0\}$ positions in the fcc reciprocal lattice. Figure 42(b) and (d) show the unit cells of these two structures. The Ll_2(M = 1) or also known as DO_{22} structure is an antiphase derivative of the $Ll_2(Cu_3Au)$ structure [Fig. 42(a)] where an APB occurs at every unit cell. Similarly Ll_0(M = 1) is obtained by introducing an APB at every unit cell of the Ll_0 (CuAu) structure [Fig. 42(c)]. A perfectly ordered DO_{22} structure exhibits superlattice peaks at $\{1\frac{1}{2}0\}$ and also at 100 positions and the experimental results do not show any diffuse peak position. It has been shown[8] that if there exists a sinusoidal composition fluctuation within the DO_{22} structure the $\{100\}$ reflections are extinct and thus the diffuse sro peaks at $\{1\frac{1}{2}0\}$ positions has been explained to be due to the presence of such imperfectly ordered microdomains in the sro state. It may seem that it is equally likely that the sro state may have microdomains with Ll_0(M = 1) structure,

which also give rise to peaks at $\{1\frac{1}{2}0\}$ positions, but this structure is rarely observed in the ordered alloys and only recently Lin et al.[36] have indicated that this structure might exist in Au-40 at %Pd alloy. Moreover the $L1_0$(M = 1) structure corresponds to a stoichiometry of 50 at% solute and so its probability of occurrence will be less than the DO_{22} structure containing 25 at% solute, in the composition range investigated. The presence of $L1_0$(M = 1) type microdomains corresponding to 50 at% solute at this 25 at% solute concentration will necessarily mean a very large composition fluctuation to exist. Although it may appear to be difficult to decide as to whether the microdomains possess DO_{22} or $L1_0$ (M = 1) structure, the reasons given above and the additional reasons to be discussed shortly it is more likely that the imperfectly ordered microdomains with DO_{22} structure are responsible for the diffuse $\{1\frac{1}{2}0\}$ spots.

The presence of weak scattering present near D1a positions in Au_3Cr, Au_4Cr, Au_4V, Ni_4Mo and Ni_3Mo in the sro state can be due to the presence of microdomains with D1a structure. In the Ni_4Mo and Ni_3Mo alloys there is additional diffuse scattering present near Ni_2Mo positions which implies that there are microdomains with Ni_2Mo type superstructure. Since the intensity of Ni_2Mo spots is greater in Ni_3Mo than in Ni_4Mo, there may be a larger volume fraction of Ni_2Mo type microdomains present in Ni_3Mo than in Ni_4Mo. This is in accord with what one would expect from the difference in Molybdenum contents in these two alloys. Since no superlattice reflections at Ni_3Mo positions were detected, there may

not be any microdomains present with Ni_3Mo structure, although this is the equilibrium ℓro structure of stoichiometric Ni_3Mo. Thus, it appears that in the sro state Au_3Cr, Au_4Cr and Au_4V alloys contain predominantly microdomains of imperfectly ordered DO_{22} and Dla structures, whereas in Ni_4Mo and Ni_3Mo additional microdomains of Ni_2Mo type structure will exist. The reason why Ni_2Mo type microdomains do not exist in Au-Cr and Au-V alloys is probably because there is no ordered phase in these systems with Ni_2Mo type structure. The atomic size effects may also be very important in deciding what structures will exist in the sro state. The three structures DO_{22}, Dla and Ni_2Mo are very clsoely related to each other and it has been shown earlier[8] that DO_{22} structure can be derived from Dla by simply introducing a periodic distribution of $\{420\}\ \frac{1}{2}\langle 1\bar{1}0\rangle$ type APB's. It will be shown in the next section how the Ni_2Mo phase can be similarly derived from Ni_4Mo and vice-versa. In the sro state above T_c if the diffusion is fast enough, tiny regions with these various types of ordered structures may be continuously forming and disappearing in order to establish an equilibrium distribution. Statistically, there exists a finite probability for some other closely related structures to exist other than the above three, but their volume fraction may be very small to give rise to any appreciable diffraction effect. The degree of order within these various types of microdomains must be very low as it was impossible to reverse their contrast in the dark field of these diffuse spots. On quenching fast enough from above

T_c, the high temperature distribution of various types of microdomains is essentially retained and depending on the quenching rate the degree of order within these microdomains may be slightly enhanced as is reflected in the intensities of Dla spots in diffraction patterns of quenched Au_3Cr compared to those taken above T_c. The evidence for the presence of various types of microdomains is primarily based on their diffraction effects. Although the dark field micrographs do not reveal directly the microdomains when the spots are very diffuse, they do reverse contrast for respective microdomains after short time aging when the degree of order has increased slightly. For example the microdomains observed in Fig. 28(a) by dark fielding the $\{1\frac{1}{2}0\}$ spot together with the streaks may consist of predominantly imperfectly ordered DO_{22} regions.

The above discussion leads us to propose a structural model of the sro state that is different from the classical microdomain concept where the structure of microdomains was simply assumed to correspond to the equilibrium ℓro structure. In this modified microdomain concept the sro state consists of not one but several types of microdomains whose structures do not necessarily correspond to the equilibrium ℓro structure. In some cases, as in Ni_3Mo, the equilibrium ℓro structure may not exist at all in the sro state. It has been mentioned earlier that Clapp[37] has used a Probability Variation Method (PVM) derived earlier by him,[38] to determine the complete frequency distribution of nearest neighbor configurations for a number of cubic alloys from their experimentally

determined sro parameters. He used the word "cluster" in the general sense of the term to mean a group of atoms A and B arranged in some ordered fashion, and has been termed "microdomain" in this thesis. He calculated the "enhancement factor," defined as the ratio of a cluster's population in the sro state to its population in an ideal random alloy of the same composition, and also the percent of atoms in the lattice of a given kind (say A or B), that have that particular cluster configuration. His calcuations showed that the most enhanced configuration relative to the random state often corresponded to the perfectly ordered state, although its volume fraction may be very small. There were also departures from this simple expectation, although it is not clear how many cases (if any) result from data limitation. His calculations on Au_3Cu (Ll_2 structure) show a rather surprising result that the most enhanced clusters are the Ll_0 (CuAu) type and the fourth most enhanced clusters are Cu_3Au type. Unfortunately, for the systems investigated in this work there are no three-dimensional sro parameters available and so such probability calculations cannot be performed. However, there are some three-dimensional sro parameters available [39] for Ni - 10 at% W, which is quite similar to the Ni-Mo alloys. Clapp's calculations[40] using these sro parameters of Ni - 10 at% W show the most enhanced cluster to be DO_{22} type. The next most enhanced cluster is the Dla with one mistake ie one atom is in the wrong place as compared to the perfectly ordered state. It is not unreasonable to expect a similar distribution

in Ni-Mo alloys and so the previous choice for DO_{22} type microdomains to be present in the sro state of Au-Cr, Au-V, and Ni-Mo alloys instead of $L1_0$(M = 1) type is justified. Furthermore, the proposed modification of the microdomain concept of sro is in line with Clapp's theoretical calculations.

The results of diffuse scattering in Au_3Mn can also be explained qualitatively by structural models. The cigar shaped $\{1\frac{1}{2}0\}$ spots give rise to diffuse scattering at the superlattice reflections P, Q, R, S and their equivalent spots [Fig. 25(c)]. The superlattice reflections in Fig. 25(c) can be thought of as formed by the splitting of the reciprocal lattice points with mixed integers h_1, h_2, and h_3, the splitting distance being $\pm \frac{m_1}{2}$ along $[h_1 00]$ and $\pm \frac{m_2}{2}$ along $[0h_2 0]$, which arise from the presence of periodic APB's at every M_1 $(= \frac{a_1^*}{m_1})$ and M_2 $(\frac{a_2^*}{m_2})$ cells along the respective directions, as described earlier in sec. 3.1.6. At temperatures above T_c, if there exists microdomains with the Watanabe type structure, but without any fixed periodicities M_1 and M_2 then there will be no strong superlattice reflections, but a broad diffuse scattering near positions corresponding to all possible periodicities that are present as observed in Fig. 26(b). The superlattice reflections such as at A and C [Fig. 25(c)] that arise from the periodicities both M_1 and M_2 may be washed out if none of them are definite, and instead show a very broad scattering near all possible combinations of M_1 and M_2, which may be difficult to detect above the background level. Since the origin of the satellites in Fig. 25(c) is most likely to be due

to periodic lattice modulation or composition modulations in the ro state, these will be completely washed out in the sro state because then there will be hardly any such periodic modulation present. This explains the absence of any scattering near satellite positions above T_c. Thus the diffuse scattering in Au_3Mn can also be accounted for by the presence of microdomains with Watanabe type structure.

The presence of the microdomains of such long period Watanabe type structure in the sro state would necessarily imply that long range interatomic interactions are present. This would contradict the usual idea of short range interactions being present in the sro state. The justification for long range interactions being present in the sro state has been given by Cowley[41] and it has been argued that the presence of flat regions on the Fermi surface give rise to long range interatomic interactions. Moss[42] and Hashimoto and Ogawa[33] have tried to explain the diffuse split spots in Cu-Au alloys, and also Scattergood et al.[43] have tried to explain the diffuse scattering in Cu-Al alloys in terms of these flat regions on the Fermi surface. Although the presence of flat regions on the Fermi surface can explain some of the observed diffuse sro scattering in many systems, the structural aspect of the sro state should not be neglected. On the other hand the presence of long range interatomic interactions supports the idea that microdomains with Watanabe type long period supersturcture may be present in sro Au-Mn alloys. In all these descriptions of the microdomains it is not at all implied that they possess the perfectly ordered

structure, but an imperfectly ordered structure within which the degree of order may be very low.

4.3. The Formation of Metastable Ni_2Mo Phase: In this section we will try to give some thermodynamic justification for the occurrence of the metastable Ni_2Mo and Ni_4Mo phases at stoichiometric Ni_3Mo compositions. Usually during the decomposition of a supersaturated solid solution if the structure of the final equilibrium phase is not simply related to the parent phase a metastable phase may form. In some cases, it may go through several transition phases before the final equilibrium phase is reached as is well known in Al-Cu system. The structure of Ni_3Mo is not very simply related to the fcc α solid solution. On the other hand, the three fcc based structures Ni_4Mo, Ni_2Mo and DO_{22} are very simply derived from the basic fcc unit cell as described earlier in Figs. 3, 4 and 42 respectively. Recently Richards and Cahn[44] have outlined a procedure for deriving the ground state of binary ordering alloys as a function of composition and the second neighbor interaction parameter V. The ground state for a given basic crystal structure, composition and V is the state that has lowest configurational energy. The energy of mixing (E) for the three structures Ni_4Mo, Ni_2Mo and DO_{22} as a function of composition of solute B (C) and the first and second nearest neighbor interaction parameters (V_1 and V_2) can be written as,

$$\underline{\text{For } Ni_4Mo,} \quad \frac{E}{NV_1} = -\frac{3}{5} - 3C - 2C\left(\frac{V_2}{V_1}\right) \text{ for } 0.2 \leqslant C \leqslant 0.3 \qquad (2)$$

$$\frac{E}{NV_1} = -\frac{3}{5} - 3C - \frac{3}{5}\left(\frac{V_2}{V_1}\right) \text{ for } 0.3 \leqslant C \leqslant 0.4 \qquad (3)$$

$$\underline{\text{For } Ni_2Mo} \quad \frac{E}{NV_1} = -\left(3C + \frac{1}{2}\right) - 3C\left(\frac{V_2}{V_1}\right) \text{ for } 0.167 \leqslant C \leqslant 0.33 \qquad (4)$$

$$\text{For } DO_{22}, \quad \frac{E}{NV_1} = \left(-3C + \frac{3}{4}\right) - \left(\frac{V_2}{V_1}\right)\left(3C - \frac{1}{2}\right) \text{ for } 0.25 \leqslant C \leqslant 0.375 \qquad (5)$$

Using these equations the energy of mixing was calculated for the three structures for different values of the ratios $\frac{V_2}{V_1}$ and Figs. 43 (a) - (c) show some typical results. It can be seen that for $\frac{V_2}{V_1} = 0.1$, the DO_{22} structure has the lowest configurational energy and Ni_4Mo the next lowest and then Ni_2Mo. As $\frac{V_2}{V_1}$ is increased to 0.4 the energy of Ni_2Mo becomes lower than Ni_4Mo. The main result that comes out of these calculations is that the energies of these three structures are very close to each other for a ratio of $\frac{V_2}{V_1}$ between 0.4 and 0.5. If we recall the results of computed diffuse scattering maps for Ni_3Mo using Clapp-Moss theory, it will be seen that a ratio of $\frac{V_2}{V_1} = 0.4$ gave reasonable agreement with the experimental diffuse scattering results. Thus the ratio $\frac{V_2}{V_1} = 0.4$ is a good estimate for Ni_3Mo and for this value the configurational energies for Ni_2Mo and Ni_4Mo almost degenerate at 25 at. % solute [Fig. 43(b)], and that of DO_{22} is slightly lower. Because of the approximations involved in arriving at the configurational energies, there may be an error of 10-15% in the estimated values, and so it is rather difficult to say which, of the three structures DO_{22}, Ni_2Mo and Ni_4Mo, has the lowest energy. All we can really say is that the energies of the three

structures are close to one another. Of these three DO_{22} structure being the simplest may nucleate first. The microdomains observed after short time aging predominantly consist of imperfectly ordered regions of DO_{22} with some Ni_4Mo and Ni_2Mo. On further aging local composition fluctuations may continuously transform the DO_{22} regions to Ni_2Mo and Ni_4Mo that have similar energies. The stoichiometry is easily balanced if both Ni_2Mo and Ni_4Mo form simultaneously side by side. This explains why Ni_2Mo and Ni_4Mo coexist together during decomposition of Ni_3Mo. Similarly the presence of Ni_2Mo phase at Ni_4Mo composition can be explained because the configurational energies of the two structures degenerate at 20 at. % solute (the stoichiometric Ni_4Mo composition). The similar configurational energies of DO_{22} structure with those of Ni_2Mo and Ni_4Mo further support the earlier choice for the imperfectly ordered DO_{22} type microdomains to be responsible for $\{1\ \frac{1}{2}\ 0\}$ sro spots, rather than the $L1_0$ (M = 1) type.

Apart from the thermodynamic reasonings, a close examination of the two structures Ni_2Mo and Ni_4Mo shows why Ni_2Mo can be present in Ni_4Mo. It has been shown earlier[8] that the DO_{22} structure can be formed from D1a by introducing APB's of the nonconservative type. In a similar manner Ni_2Mo structure can also be created from Ni_4Mo. Figure 44 shows an example where an APB of the type $(420)\frac{1}{2}[\bar{1}01]$ has been introduced on the (420) plane in the fully ordered D1a structure. The notations used are the same as those in Figs. 3 and 4. The introduction of such an APB is equivalent to removing two layers of $\{420\}$ planes containing pure Ni atoms. A comparison of the area in the vicinity of the APB with Fig. 4 shows that the structure locally transforms to Ni_2Mo type, as if

there is a platelet of Ni_2Mo on (420) plane with a thickness of $3d_{420}$. Some of these local regions may act as nuclei for Ni_2Mo phase and may grow or some may stay as such. The observation of the weak <210> streaks extending from one superlattice reflection to another with a maxima at the Ni_2Mo position in Fig. 32(e) for Ni_3Mo and in Figs. 36(d) and 37 for Ni_4Mo can now be explained to be due to these thin plate-like Ni_2Mo regions formed on {420} planes. The Ni_4Mo structure can be formed in a similar manner from the Ni_2Mo structure by introducing an APB of the type $(420)\frac{1}{2}[101]$ as shown in Fig. 45. In the stacking of (420) planes near the APB, here there are five pure Ni planes in between the two pure Mo planes, which is typical of Ni_4Mo structure (Fig. 3).

4.4. <u>The Origin of Tweed Pattern</u>: Although the tweed striations observed in Figs. 35, 36 and 38 behave as if the displacement vector $\vec{R}$ is principally along <110>, the exact origin of the tweed is not quite clear. In the Cu-Be alloys this has been thought[30] to arise from the high elastic anisotropy of copper (A = 3.2). The elastic anisotropy is represented by the anisotropy factor (A) given by

$$A = G_{<100>} / G_{<110>} = 2C_{44}/(C_{11} - C_{12}) \qquad (8)$$

where $G_{<100>}$ and $G_{<110>}$ are the shear modulii for {100}<010> and {110} $<1\bar{1}0>$ respectively and C_{ij} are the stiffness constants. In Cu-Be the tetragonal distortion associated with the disc shaped GP zones give rise to elastic shear strains on {110} planes, because of this elastic anisotropy of Cu and these elastic shear strains give rise to striations parallel to {110} planes in the images. For nickel the anisotropy factor is also high (A = 2.5), but it is not certain whether the tweed

contrast in Ni-Mo alloys can also be attributed to elastic anisotropy. Recent work[46] on computer simulation of electron transmission images has questioned this origin of the tweed and the theoretical calculations show that the primary origin of the tweed striations may lie in some form of ordered arrangement of the misfit particles and the role of anisotropy may not be so important. The anisotropy is, of course, important in deciding the habit plane of the particles and when a cubic particle precipitates in a cubic matrix the particles usually have a {100} habit if $A > 1$. The results of this study lend good support to the origin of the tweed striations as being some periodic arrangement of the ordered domains. In the very early stages of ordering when the strain is minimum the particles may be random [e.g. Fig. 28(a)] and at a later stage when the misfit is high and so also the strain energy the particles arrange in an ordered array so as to minimize the strain, thus give rise to the tweed.

V. CONCLUSIONS

1. The high temperature electron diffraction patterns of Au_3Cr and Au_4Cr above T_c show a tetrahedral intensity distribution around the $\{1\frac{1}{2}0\}$ positions which gives rise to diffuse scattering at D1a positions. The comparison of the as quenched state with diffraction patterns taken above T_c show that the sro state is essentially retained on quenching in this alloy.

2. The diffraction patterns of Au_4V in the sro state also exhibit diffuse scattering at $\{1\frac{1}{2}0\}$ and D1a positions.

3. The diffuse scattering in Au_3Mn above T_c gives rise to an intensity distribution centered around $\{1\frac{1}{2}0\}$ in such a way that weak scattering is present near most of the superlattice reflections corresponding to Watanabe type two dimensional long period superstructure.

4. The sro state of Ni_4Mo and Ni_3Mo show diffuse scattering near D1a and Ni_2Mo superlattice positions in addition to that at $\{1\frac{1}{2}0\}$ position.

5. The statistical thermodynamic model of Clapp and Moss is unable to explain the shape of $\{1\frac{1}{2}0\}$ spots in Au-Cr and Au-V alloys but can explain the gross festures of diffuse scattering in Au-Mn and Ni-Mo alloys.

6. The microdomain concept is valid in general, but the sro state may not contain only one type of mcirodomain. The sro state is best described as a mixture of imperfectly ordered microdomains with various types of superstructures in different proportions. The sro

Au-Cr and Au-V alloys contain predominantly imperfectly ordered DO_{22} and Dla type microdomains. The Ni-Mo alloys contain imperfectly ordered DO_{22}, Dla and Ni_2Mo type microdomains whereas Au-Mn alloys may contain microdomains with a structure close to that of Watanabe type long period superstructure. On the whole it is concluded that the structural model gives a better physical description of the sro state and at the same time accounts for the observed diffuse scattering results.

7. Both Ni_2Mo and Ni_4Mo phases occur as metastable phases, during the initial stages of decomposition of Ni_3Mo, where Ni_2Mo forms as platelike particles on {420} planes but Ni_4Mo is more or less equiaxed.

8. The Ni_2Mo phase also occurs as a metastable phase during the decomposition of Ni_4Mo, but its volume fraction is restricted.

9. A structural model based on the presence of non conservative APB's, shows that such APB's are nuclei for Ni_2Mo in Ni_4Mo and vice-versa.

10. Thermodynamic calculations show that the energy of mixing of Ni_2Mo phase is very close to that of Ni_4Mo and this explains why this Ni_2Mo phase occurs as a metastable phase.

11. The origin of the tweed structure during ordering is most probably due to some sort of ordered arrangement of the domains and the anisotropy of the lattice may not be so important.

ACKNOWLEDGEMENTS

The author is deeply grateful to Professor Gareth Thomas for his guidance, encouragement and support throughout this investigation. He is indebted to Dr. P. R. Okamoto for many stimulating discussions and cooperation during his stay at Berkeley. He is also thankful to Dr. P. M. J. Fisher for helpful discussions, and to Mr. Glen Stone for his help in programming. Thanks are also due to Carol Zum Brunnen for her special effort in typing and to Gloria Pelatowski for line drawings, and finally to my wife for her understanding and moral support.

This work was carried out under the auspices of the United States Atomic Energy Commission through the Inorganic Materials Research Division of the Lawrence Berkeley Laboratory, University of California, Berkeley, California.

References

1. J. E. Spruiell and E. E. Stansbury, J. Phys. Chem. Solids 26, 811 (1965).
2. H. G. Baer, Z. Metallkde, 57, 318 (1966).
3. L. E. Tanner, P. C. Clapp and R. S. Toth, Mat. Res. Bull., 3, 855 (1968).
4. J. R. Castles, J. M. Cowley and A. E. C. Spargo, Univ. of Melbourne Rep. no. UM-P-70/11 (1970).
5. P. C. Clapp and S. C. Moss, Phys. Rev., 171, 754 (1968).
6. S. C. Moss and P. C. Clapp, Phys. Rev., 171, 764 (1968).
7. P. R. Okamoto and G. Thomas, Mat. Res. Bull., 6, 45 (1971).
8. P. R. Okamoto and G. Thomas, Acta Met., 19, 825 (1971).
9. E. Ruedl, P. Delavignette and S. Amelinckx, Phys. Status Solidi, 28, 305 (1968).
10. W. B. Snyder and C. R. Brooks in Ordered Alloys, Proceedings of Third Bolton Landing Conference Sept. 1969 Eds. B. H. Kear, C. T. Sims, N. S. Stoloff and J. H. Westbrook, Claitor's Publishing Division, 275 (1970).
11. B. Chakravarti, E. A. Starke, B. G. Lefevre, J. Mater. Sci. 5, 394 (1970).
12. T. Saburi, K. Komatsu and S. Nenno, Phil. Mag. 20, 1091 (1969).
13. F. Ling and E. A. Starke, Acta Met., 19, 759 (1971).
14. M. Yamamoto, S. Nenno, T. Saburi and Y. Mizutani, Trans. JIM, 11, 120 (1970).
15. G. Thomas in High Temperature, High Resolution Metallography, Gordon and Breach Science Publishers, N.Y., 217 (1967).
16. D. Harker, J. Chem. Phys., 12, 317 (1944).

17. S. Saito and P. A. Beck, Trans. AIME, 215, 938 (1959).

18. E. Ruedl and S. Amelinckx, Mat. Res. Bull., 4, 361 (1969).

19. L. E. Tanner, Phys. Status Sol., 30, 685 (1968).

20. H. Warlimont and G. Thomas, Metal Sci. Journal, 4, (1970).

21. S. K. Das and G. Thomas (unpublished research).

22. H. Sato, R. S. Toth, and G. Honjo, J. Phys. Chem. Solids, 28, 137 (1967).

23. E. Stolz and K. Schubert, Z. Metallkde, 53, 433 (1962).

24. D. Watanabe, J. Phys. Soc. Japan, 15, 1030 (1960).

25. D. Watanabe, J. Phys. Soc. Japan, 15, 1251 (1960).

26. D. P. Morris and J. L. Hughes, Acta Cryst., 15, 1062 (1962).

27. D. P. Morris and J. L. Hughes, Acta Cryst. 17, 209 (1964).

28. D. P. Morris, J. L. Hughes and G. Davies, Phil. Mag., 8, 1977 (1963).

29. H. Sato and R. S. Toth in Alloying BEhavior and Effects in Concentrated Solid Solutions, Ed. T. B. Massalski, Gordon and Breach Science Publishers, N.Y., 295 (1963).

30. L. E. Tanner, Phil. Mag. 14, 111 (1966).

31. L. E. Tanner, in Ordered Alloys, Proceedings of Third Bolton Landing Conference, Sept. 1969, Eds. B. H. Kear et al., Claitor's Publishing Division 253 (1970).

32. M. J. Marcinkowski and L. Zwell, Acta Met. 11, 373 (1963).

33. S. Hashimoto and S. Ogawa, J. Phys. Soc. Japan 29, 710 (1970).

34. K. Sato, D. Watanabe and S. Ogawa, J. Phys. Soc. Japan 17, 1647 (1962).

35. D. Watanabe and P.M.J. Fisher, J. Phys. Soc. Japan, 20, 2170 (1965).

36. W. Lin, J. E. Spruiell and R. O. Williams, J. Appl. Cryst. 3, 297 (1970).

37. P. C. Clapp, Tech. Rep. No. 249, Ledgemont Laboratory, Kennecott Copper Corporation (1970).

38. P. C. Clapp, J. Phys. Chem. Solids, 30, 2589 (1969).

39. A. M. Ammons and J. E. Spruiell, J. Appl. Phys. 39, 3682 (1968).

40. P. C. Clapp (private communication)

41. J. M. Cowley in The Chemsitry of Extended Defects in Non-metallic Solids, Eds. L. Eyring and M. Okeeffe, North Holland, London 259 (1970).

42. S. C. Moss, Phys. Rev. Letters, 22, 1108 (1969).

43. R. O. Scattergood, S. C. Moss and M. B. Bever, Acta Met. 18, 1087 (1970).

44. M. J. Richards and J. W. Cahn, Acta Met. 19, 1263 (1971).

45. M. J. Richards, Sc. D. Thesis, M.I.T. (1971).

46. P. J. Fillingham, H. J. Leamy and L. E. Tanner, Proceedings of 5th International Materials Symposium, University of California, Berkeley, 163 (1971).

FIGURE CAPTIONS

Fig. 1. Calibration curve for the Siemens hot stage.

Fig. 2. Partial phase diagram of the Ni-Mo system.

Fig. 3. The crystal structure of ordered Ni_4Mo (a) the body centered tetragonal unit cell as related to the disordered fcc lattice, (b) atoms on the (001) plane, the full circles represent atoms on the zeroth layer and the open circles represent atoms on a layer $\frac{a}{2}$ above or below.

Fig. 4. The crystal structure of ordered Ni_2Mo (a) the orthorhombic unit cell as derived from the original fcc lattice (b) atomic packing on (001) plane.

Fig. 5. (a) [001] reciprocal lattice section containing Dla, Ni_2Mo, $\{1\frac{1}{2}0\}$ sro spots, (b) $[\bar{1}30]$ reciprocal lattice section.

Fig. 6. [001] diffraction pattern of Ni_4Mo quenched in iced brine from 1100°C.

Fig. 7. The X-ray diffuse intensity at 86°K in the $\{h_1, h_2, 0\}$ plane of reciprocal space for a sample of Ni_4Mo quenched from 1000°C in iced brine (after Spruiell and Stansbury[1]).

Fig. 8. Iso-intensity contour map of the [001] electron diffraction pattern of quenched Ni_4Mo. The dotted line outlines the portion traced.

Fig. 9. $[\bar{1}30]$ electron diffraction pattern of quenched Ni_4Mo.

Fig. 10. (a) [110] diffraction pattern of Ni_4Mo.

(b) the indexed pattern.

Fig. 11. Diffraction patterns of Ni_3Mo after quenching in iced brine from 1270°C (a) [001] pattern (b) [110] pattern (c) $[\bar{1}30]$ pattern

Fig. 12. (a) Bright field micrograph of quenched Ni_4Mo (b) another area with $\vec{g}$<220>.

Fig. 13. Ni_3Mo after quenching from 1270°C in iced brine (a) B.F. $\vec{g}[002]$, (b) D.F. $\vec{g}[00\bar{2}]$, (c) B.F. $\vec{g}[\bar{1}13]$, (d) B.F. $\vec{g}[1\bar{1}\bar{1}]$.

Fig. 14. Partial phase diagram of Au-Cr system.

Fig. 15. Evaporated thin film of Au_3Cr after aging for 67 hrs at 270°C (a) [001] orientation, (b) $[\bar{1}30]$ orientation.

Fig. 16. (a) [001] diffraction pattern of Au_3Cr film taken at 330° ± 10°C (b) $[\bar{1}30]$ pattern of same Au_3Cr film taken at 370°C.

Fig. 17. Electron diffraction patterns of bulk Au_3Cr after quenching in water from 550°C (a) [001] pattern (b) $[\bar{1}30]$ pattern.

Fig. 18. (a) [121] diffraction pattern of bulk Au_3Cr, quenched into water (b) the indexed pattern.

Fig. 19. Three-dimensional reciprocal lattice models of Au_3Cr showing (a) the distribution of diffuse scattering in the sro state, (b) the six variants of Dla in the ℓro state.

Fig. 20. Diffraction patterns of thin film of Au_3Cr slowly cooled from 400°C (a) [001] (b) $[\bar{1}30]$.

Fig. 21. [001] electron diffraction pattern of thin film of Au_4Cr taken at 340°C.

Fig. 22. Partial phase diagram of the Au-V system.

Fig. 23. [001] diffraction pattern of bulk Au_4V quenched in iced brine from 900°C.

Fig. 24. Au-rich portion of the Au-Mn phase diagram.

Fig. 25. (a) [001] diffraction pattern of evaporated thin film of Au_3Mn showing two-dimensional long period superstructure (Watanabe type) (b) another [001] pattern showing additional Dla superlattice spots (c) sketch of [001] pattern corresponding to Watanabe type structure.

Fig. 26. (a) [001] diffraction pattern of ordered thin film of Au_3Mn taken at 450°C (b) the same pattern as (a) but taken at 500°C.

Fig. 27. [121] diffraction patterns of Ni_3Mo sample (a) after quenching in iced brine from 1270°C, (b) after subsequent aging for 30 mins. at 650°C.

Fig. 28. Microstructure of Ni_3Mo sample after aging for 1 hour at 650°C, (a) dark field micrograph of the $\{1\frac{1}{2}0\}$ spot encircled in (b), $[1\bar{2}0]$ diffraction pattern corresponding to (a).

Fig. 29. [001] diffraction patterns of Ni_3Mo sample obtained after aging at 650°C for (a) 4 hrs., (b) 49 hrs., (c) the indexed pattern.

Fig. 30. Ni_3Mo sample after aging for 49 hrs. at 650°C, (b) $[1\bar{2}0]$ diffraction pattern, (b) dark field micrograph of Ni_2Mo spot whose position is shown in (a) by the superimposed image of the objective aperture, (c) the indexed $[1\bar{2}0]$ pattern.

Fig. 31. [121] diffraction patterns of Ni_3Mo sample after aging at 650°C for (a) 4 hrs. and (b) 14 hrs. (c) the indexed pattern.

Fig. 32. Microstructure of Ni_3Mo sample after aging for 163 hrs. at 650°C, (a) dark field micrograph of Ni_2Mo spot [marked B in Fig. (c)], (c) the corresponding [121] diffraction pattern.

Fig. 33. Antiphase boundaries in Ni_3Mo after aging for 244 hrs. at 650°C, (a) bright field micrograph, (b) dark field micrograph of the same area. Foil orientation $[121]_f$ or $[001]_\gamma$

Fig. 34. (a) [121] diffraction pattern from a single domain of Ni_3Mo from an area similar to that in Fig. 33, (b) the indexed pattern where γ refers to the Ni_3Mo phase.

Fig. 35. Microstructure of Ni_4Mo after aging for 2 hrs. at 650°C (a) bright field micrograph, (b) dark field micrograph of Ni_4Mo superlattice reflection encircled in (c), (c) the corresponding [012] diffraction pattern.

Fig. 36. Ni_4Mo sample after aging for 8 hrs. at 650°C, (a) bright field micrograph, (b) dark field micrograph of Ni_4Mo superlattice spot marked B in (a), (c) [001] diffraction pattern taken from another area, (d) the [121] diffraction pattern corresponding to the area in Fig. 36(a), the foil has been tilted from that in (a) to obtain a symmetrical diffraction pattern.

Fig. 37. Ni_4Mo diffraction patterns after aging for various times at 650°C. (a) [121] pattern after 1 hr. aging, (b) [121] pattern after 24 hrs. aging, (c) $[1\bar{2}0]$ pattern after 24 hrs. aging.

Fig. 38. (a) and (b) microstructures of Ni_4Mo after aging for 24 hrs. at 650°C showing the heterogeneous reaction at the grain boundaries.

Fig. 39. Locations of the minima of V(k) at $\{1\frac{1}{2}0\}$ positions for various values of $\frac{V_2}{V_1}$ and $\frac{V_3}{V_1}$ for a positive V_1 in an fcc lattice.

Fig. 40. Theoretical diffuse scattering map for Ni_3Mo.

Fig. 41. Theoretical diffuse scattering map for Au_3Mn.

Fig. 42. (a) Unit cell of $L1_2$ structure, (b) unit cell of $L1_2$ (M=1), the antiphase derivative of $L1_2$ structure, (c) unit cell of $L1_0$ structure, (d) unit cell of $L1_0$ (M=1), the antiphase derivative of $L1_0$ structure.

Fig. 43. The theoretical curves for energy of mixing versus composition for DO_{22}, Ni_4Mo and Ni_2Mo structures calculated using (a) $\frac{V_2}{V_1} = 0.1$, (b) $\frac{V_2}{V_1} = 0.4$, (c) $\frac{V_2}{V_1} = 0.5$.

Fig. 44. An APB model showing how the Ni_2Mo structure can be derived from Ni_4Mo structure by introducing a non-conservative APB of the type $(420)\frac{1}{2}[\bar{1}01]$.

Fig. 45. An APB model showing how Ni_4Mo structure can be derived from the Ni_2Mo structure by an APB of the type $(420)\frac{1}{2}[101]$.

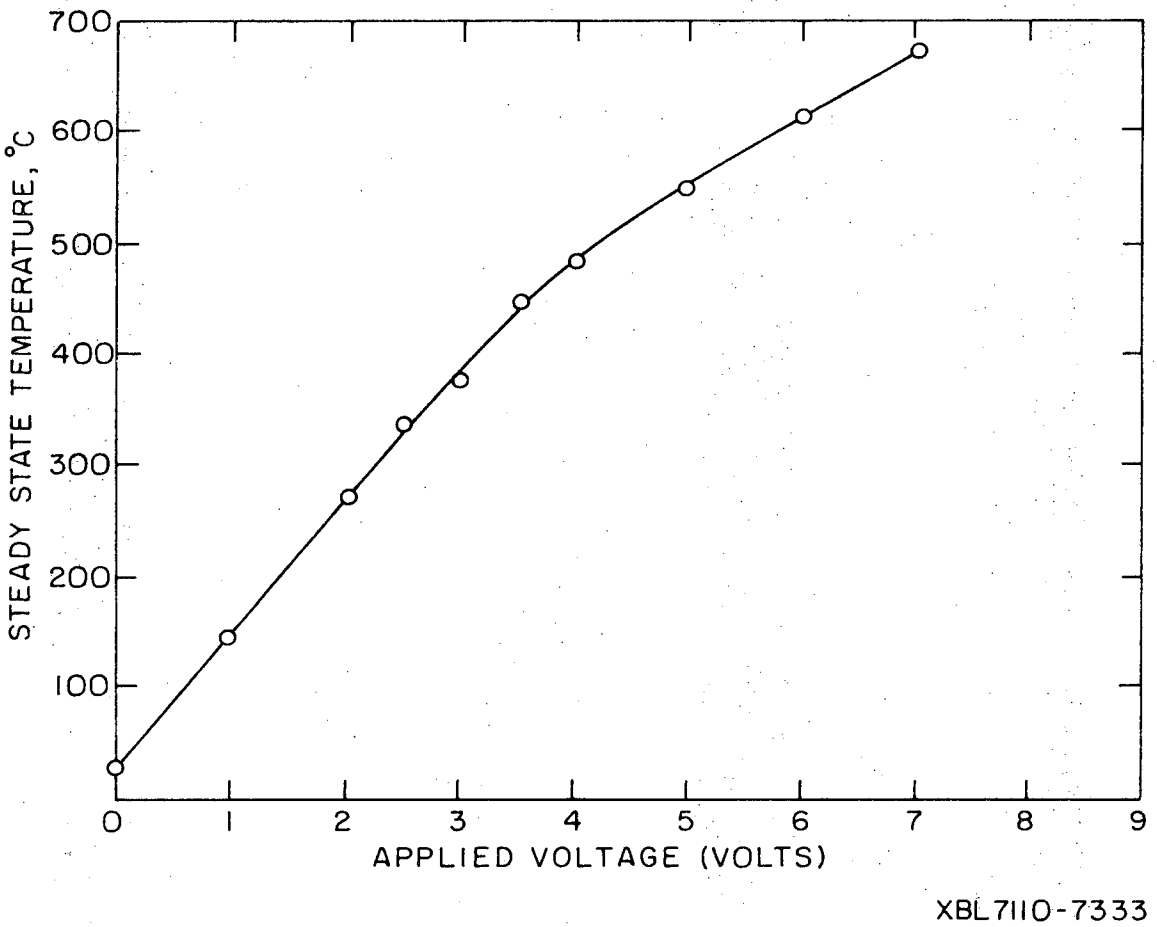
700
600
500
400
300
200
100
STEADY STATE TEMPERATURE, °C
0
1
2
3
4
5
6
7
8
9
APPLIED VOLTAGE (VOLTS)
XBL7110-7333

Fig. 1

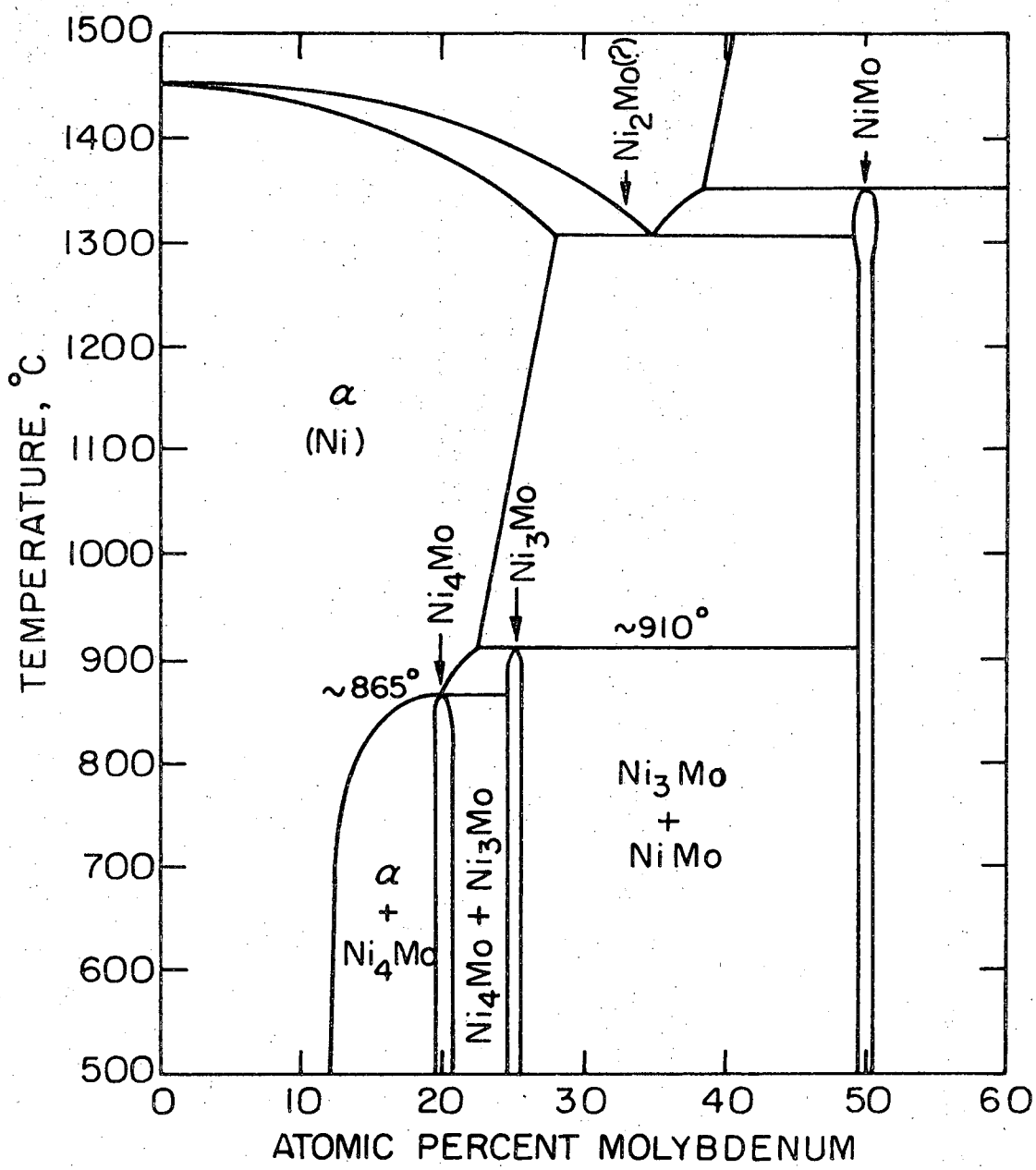

XBL7110-7329

Fig. 2

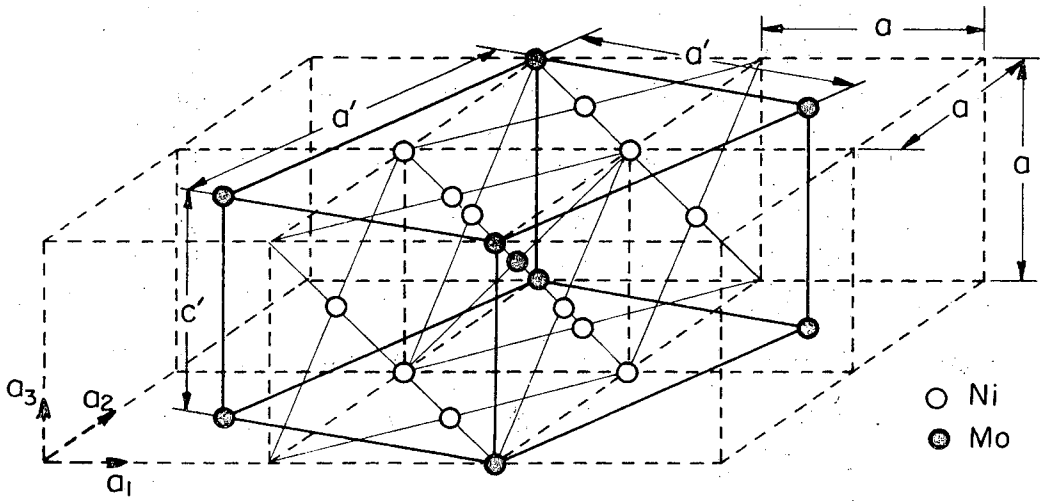

(a)

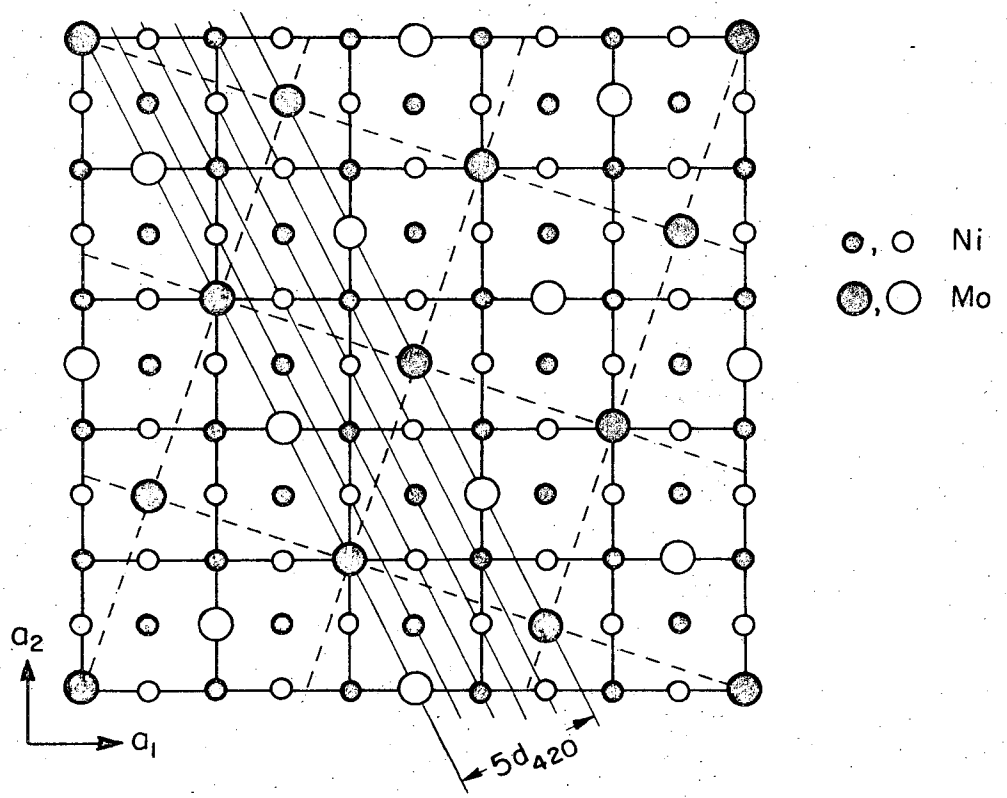

(b)

XBL7110-7433

Fig. 3

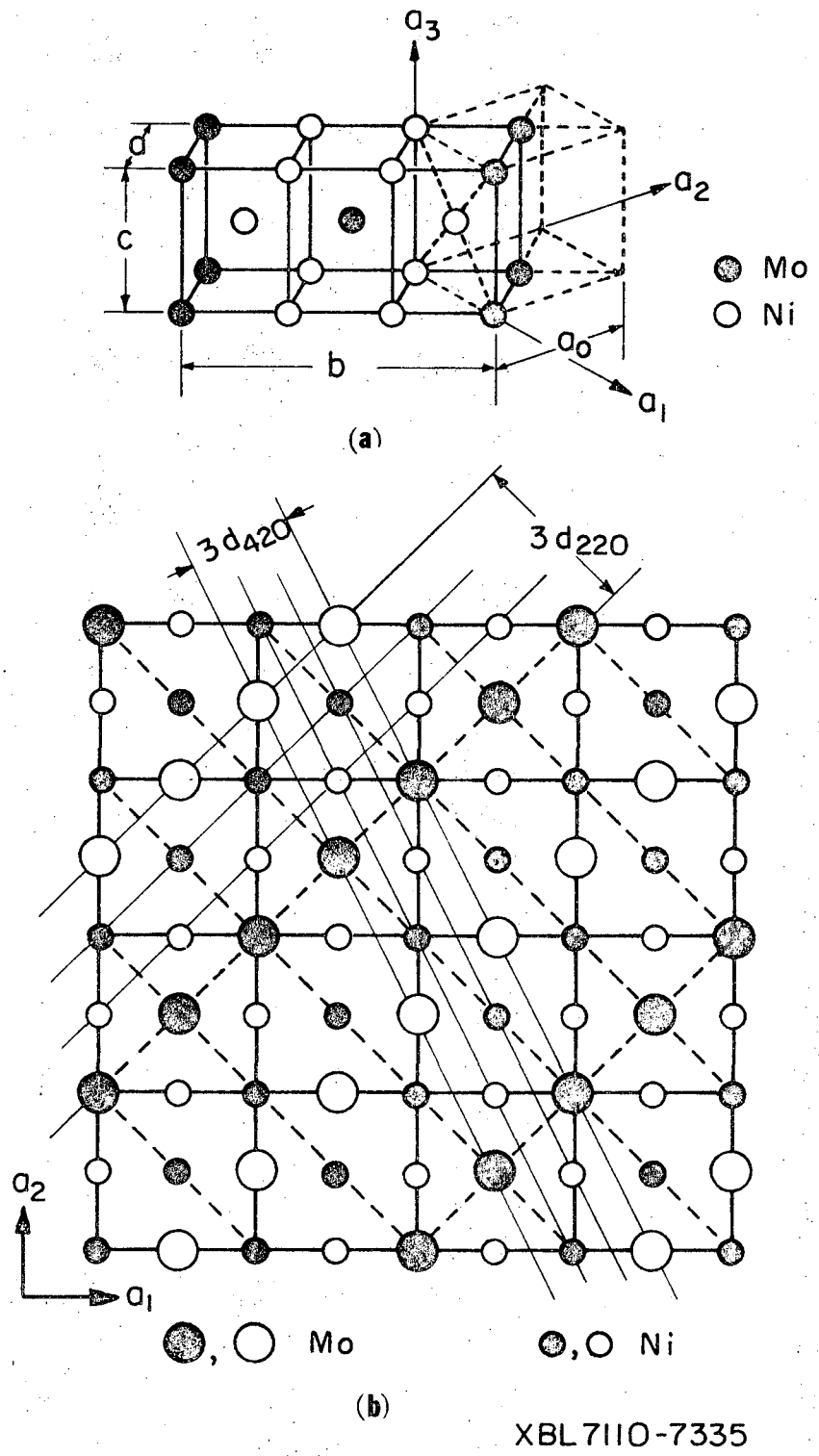

Fig. 4

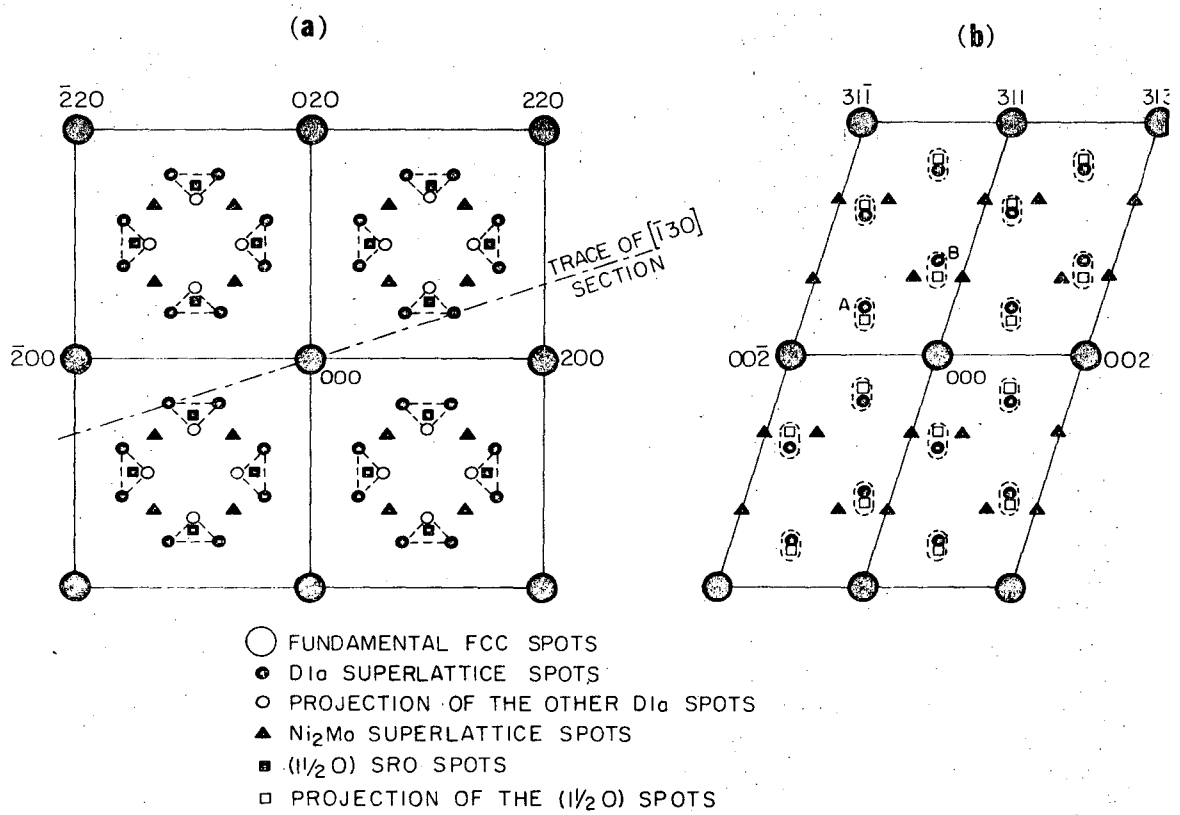

XBL717-7009

Fig. 5

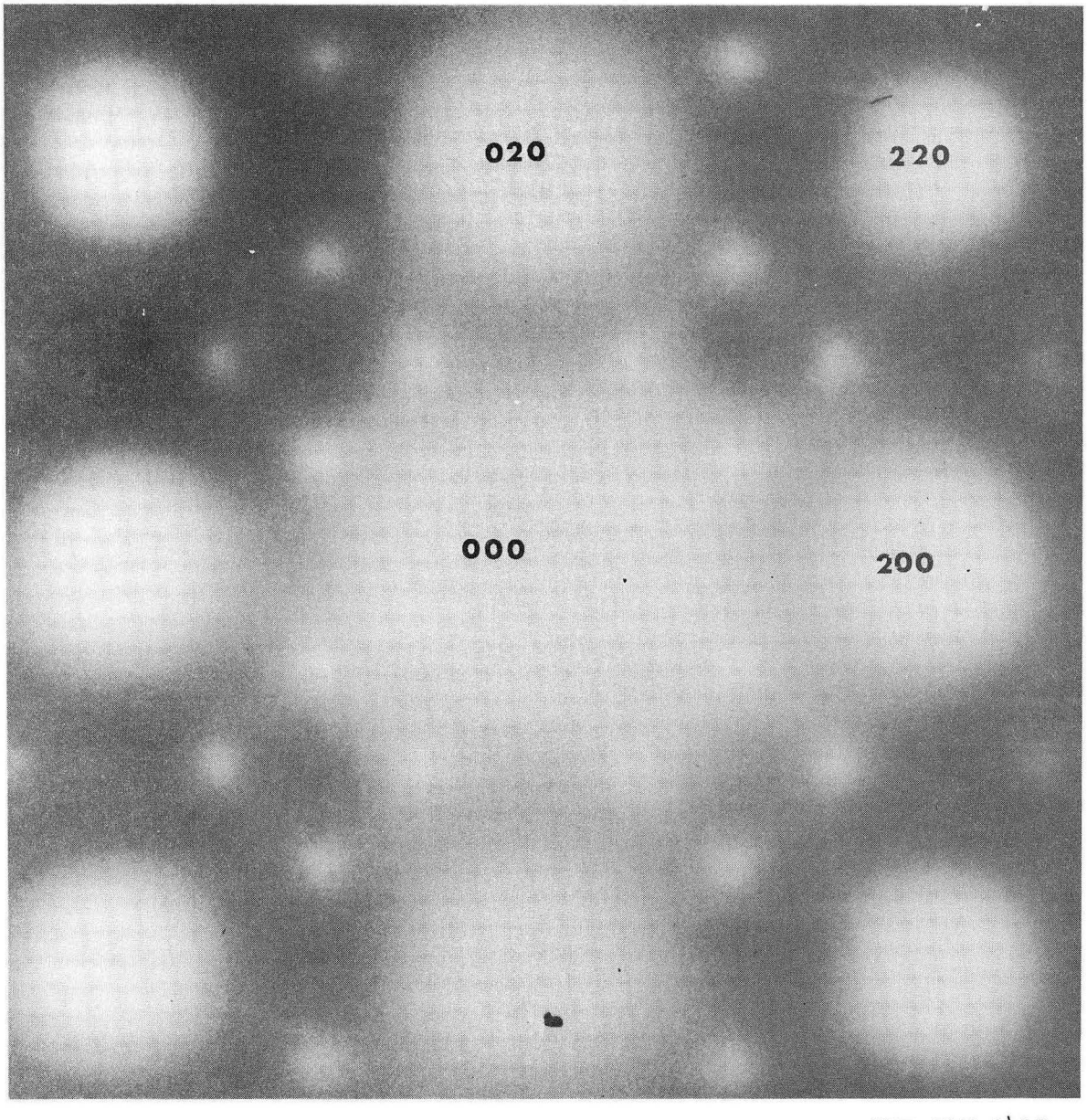

XBB 717-3410

Fig. 6

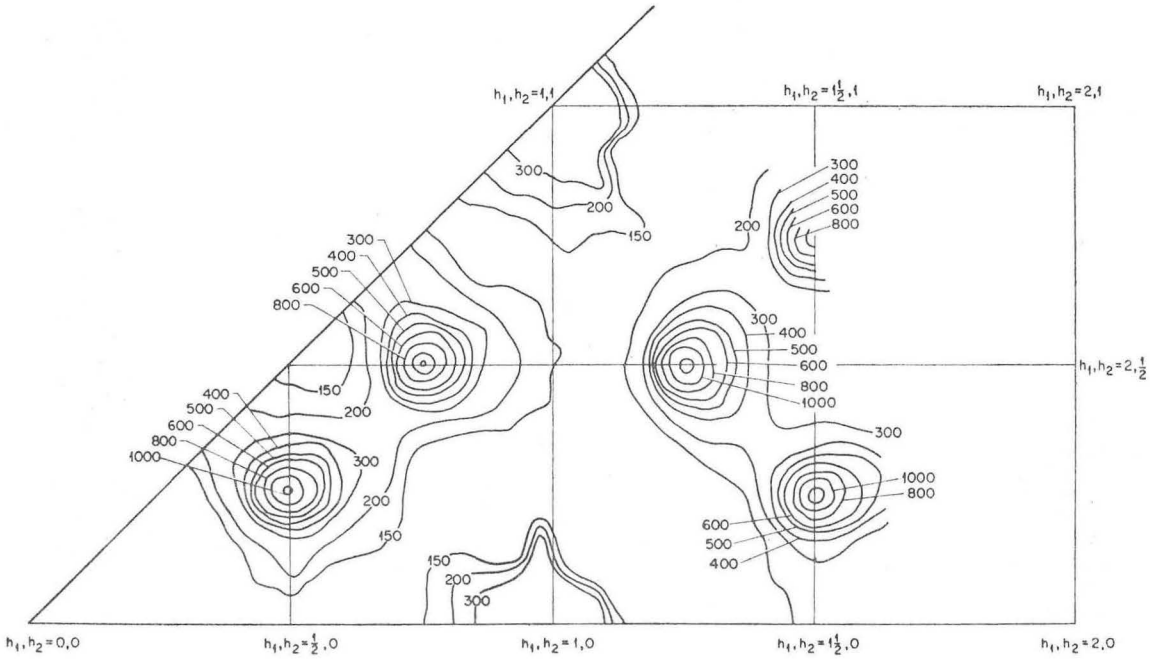

XBL 717-1218

Fig. 7

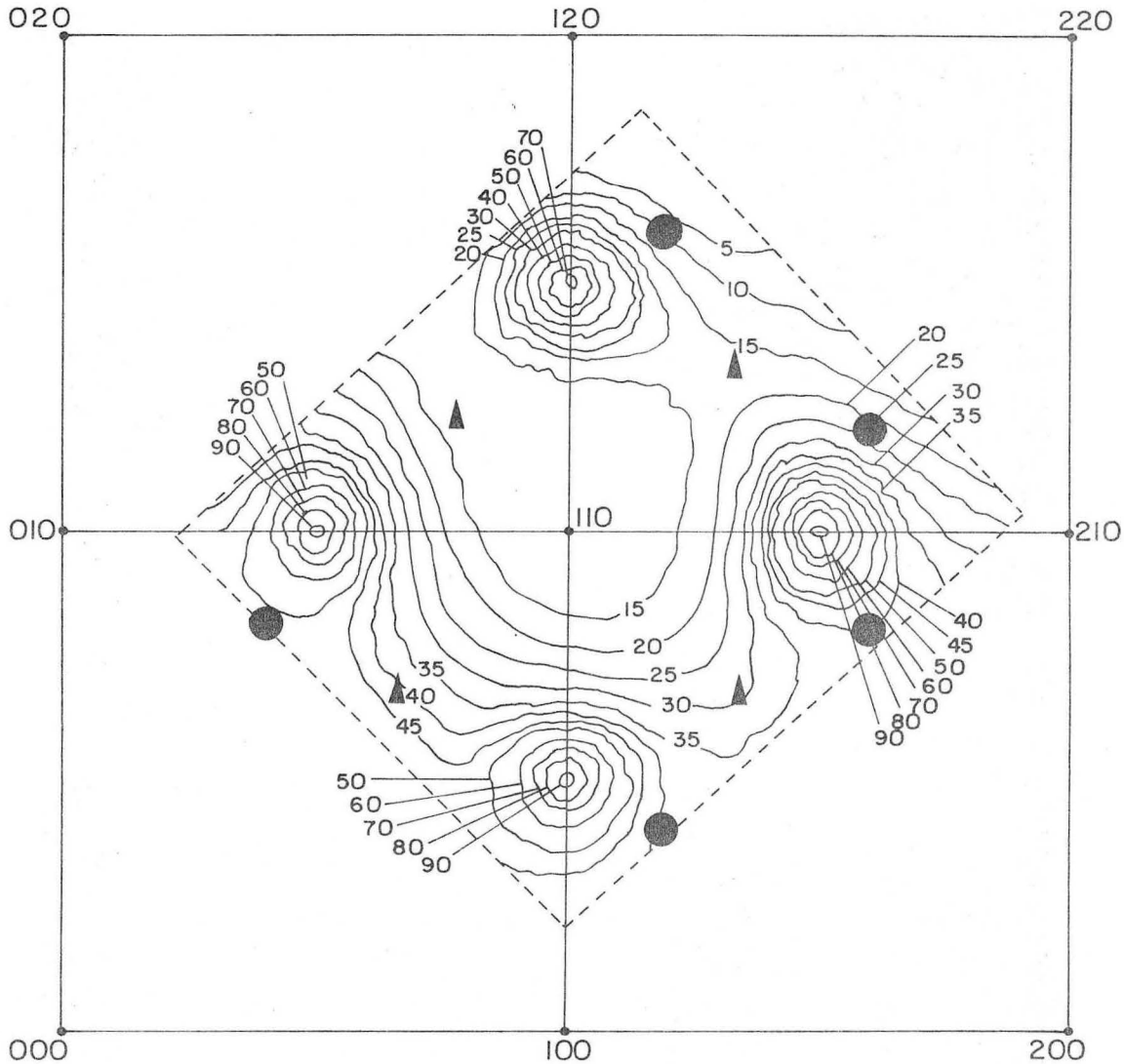

XBL7110-7338

Fig. 8

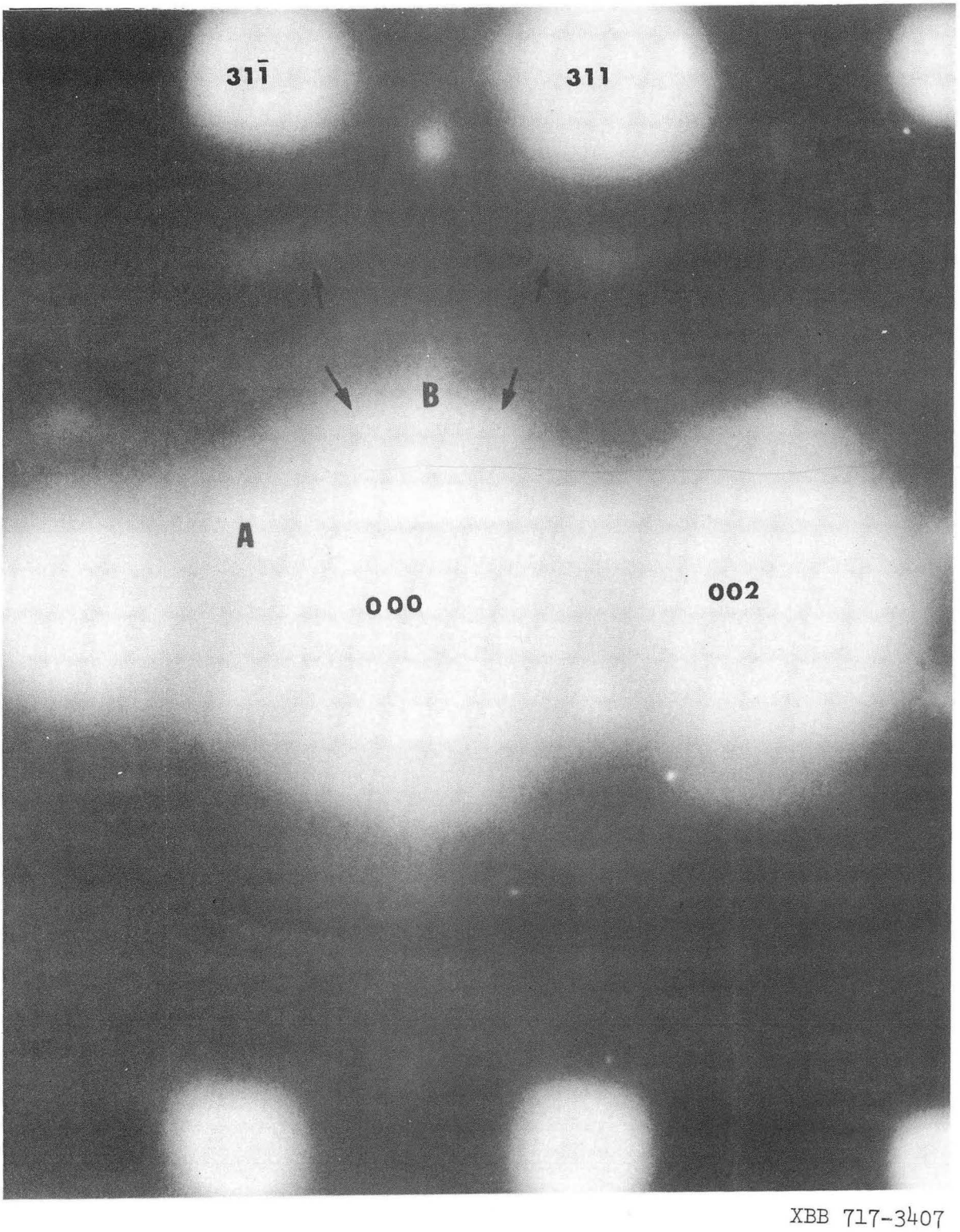

XBB 717-3407

Fig. 9

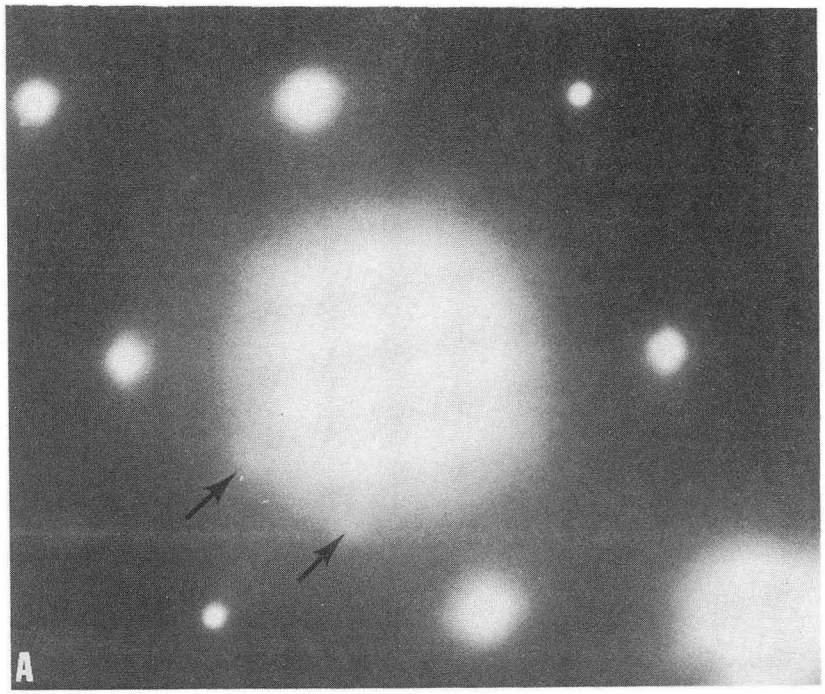

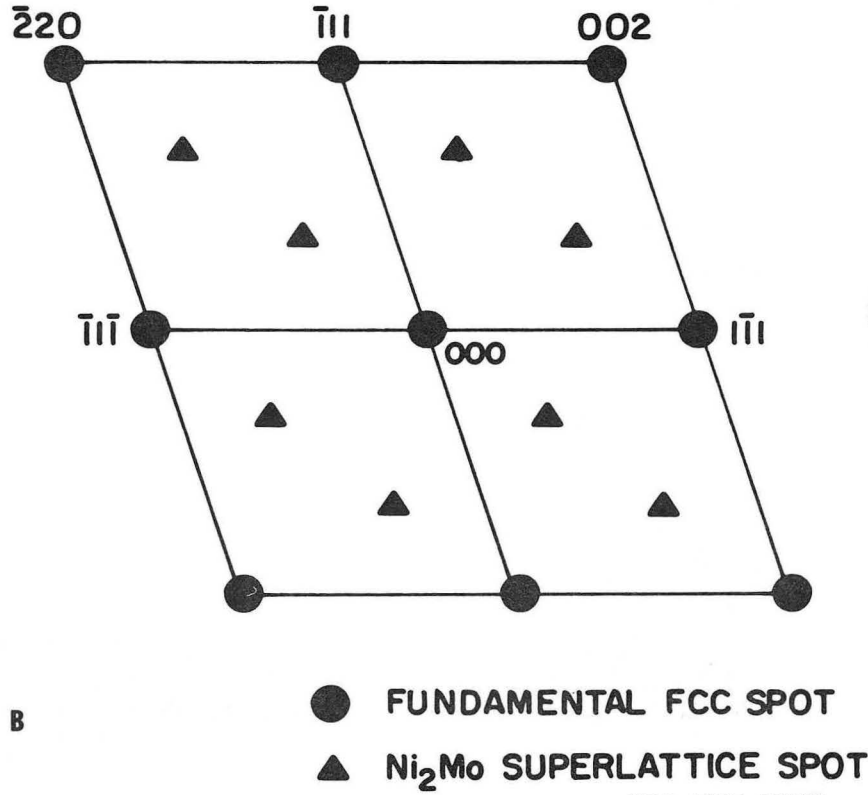

XBB 717-3397

Fig. 10

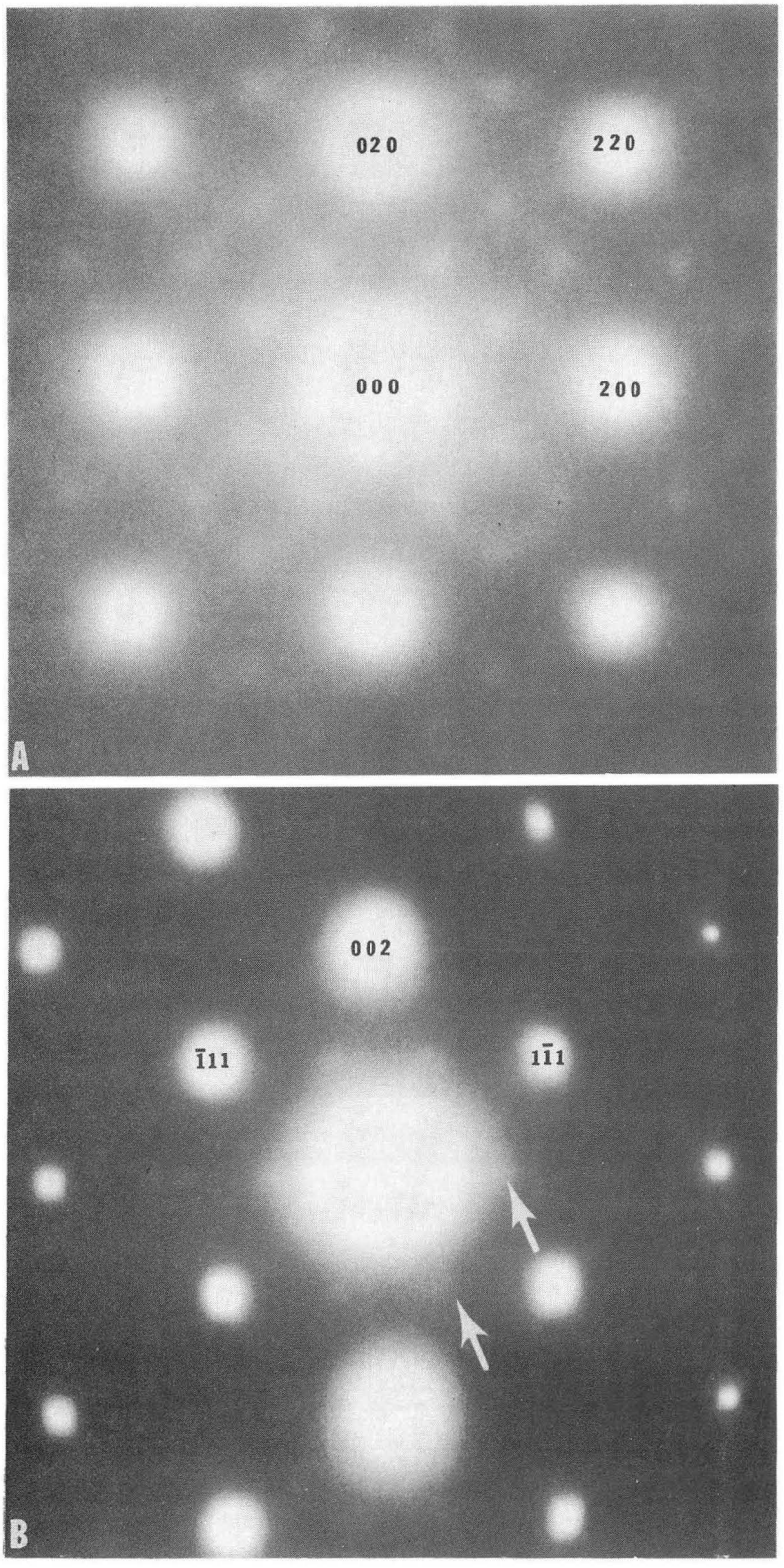

XBB 717-3406

Fig. 11

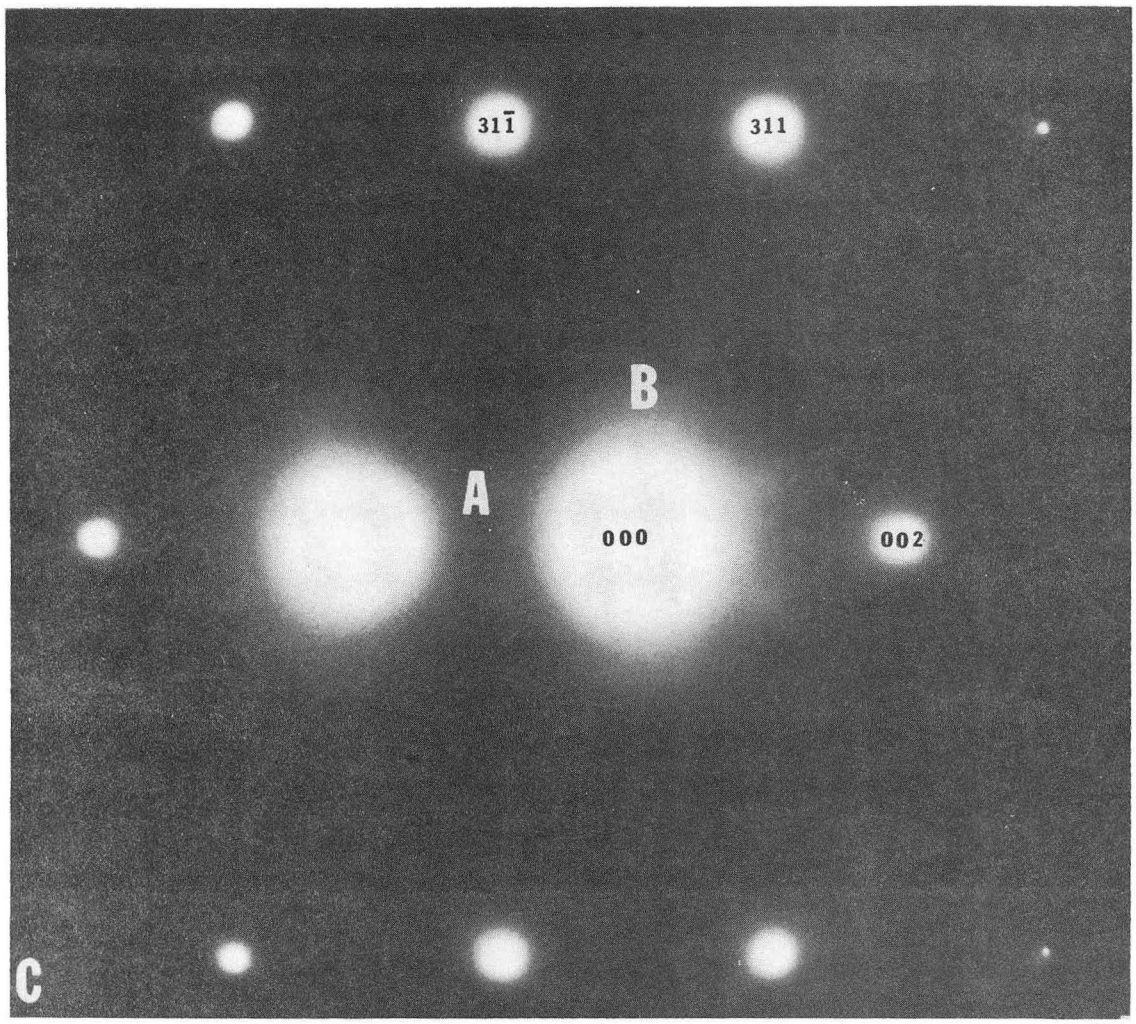

XBB 7110-4981

Fig. 11 continued.

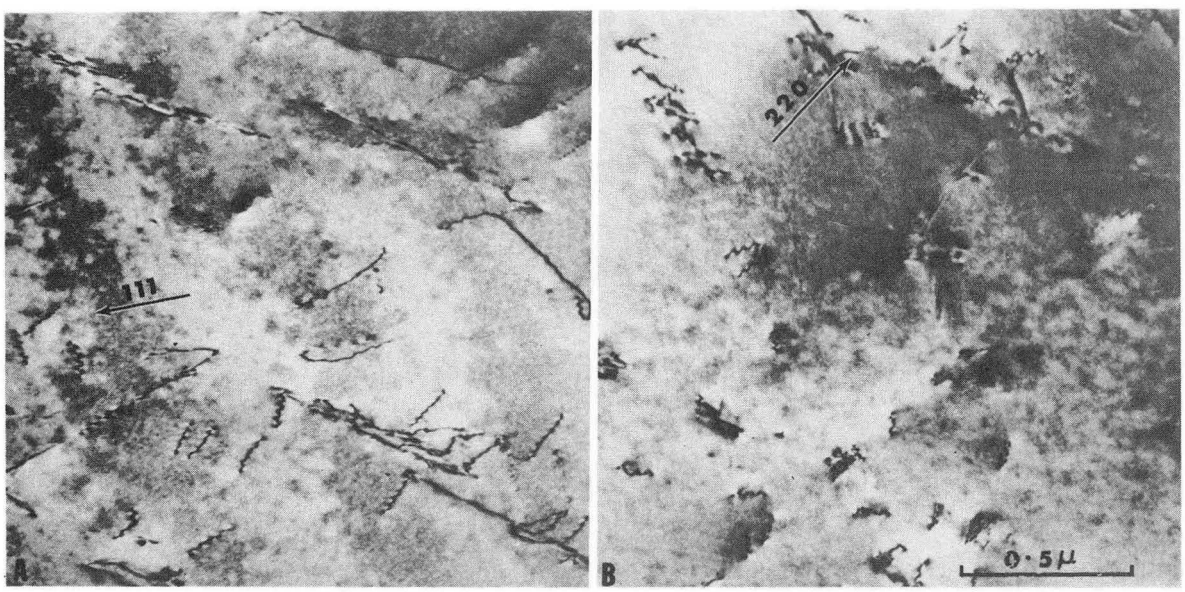

XBB 7110-4763

Fig. 12

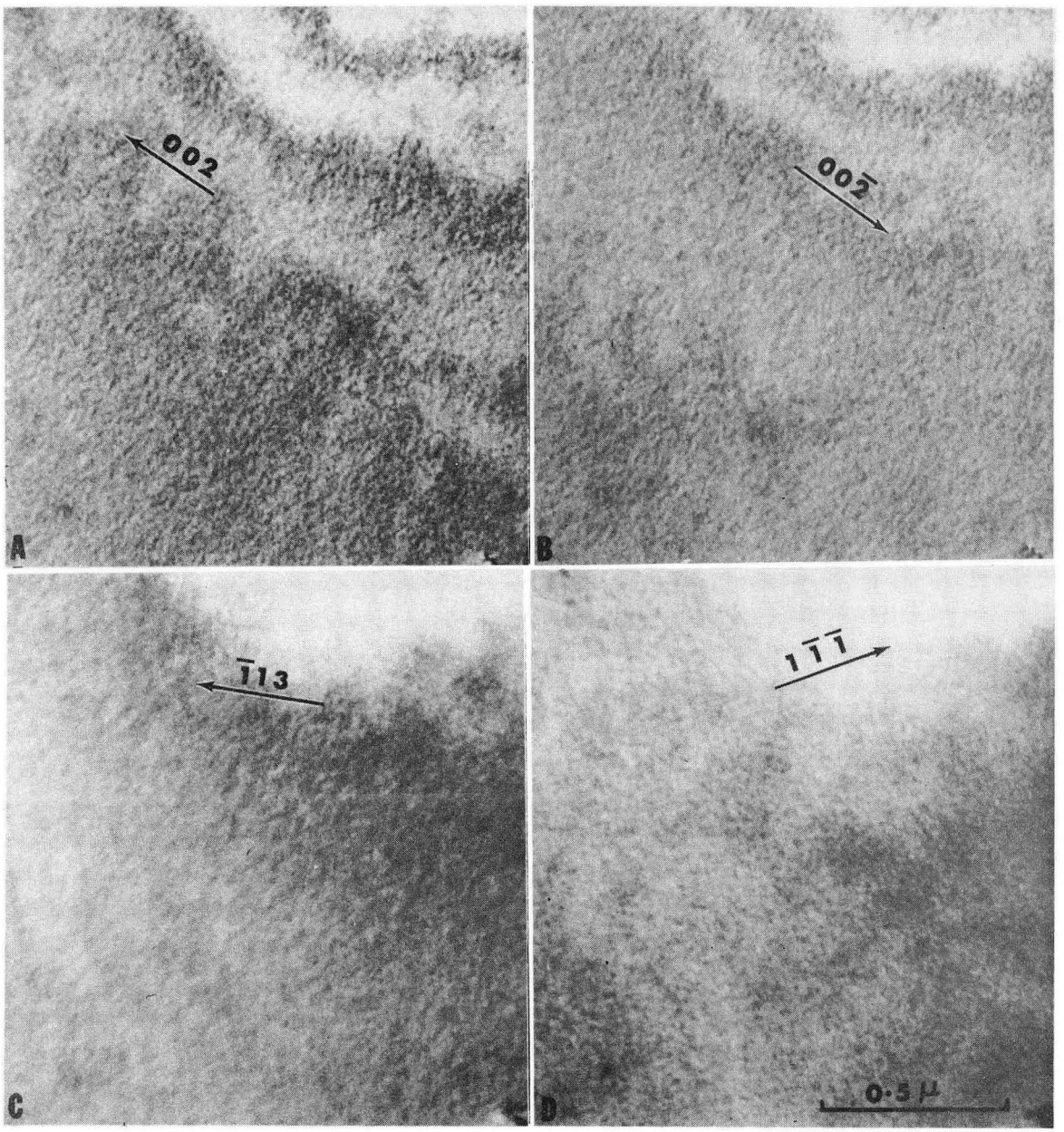

XBB 7110-4761

Fig. 13

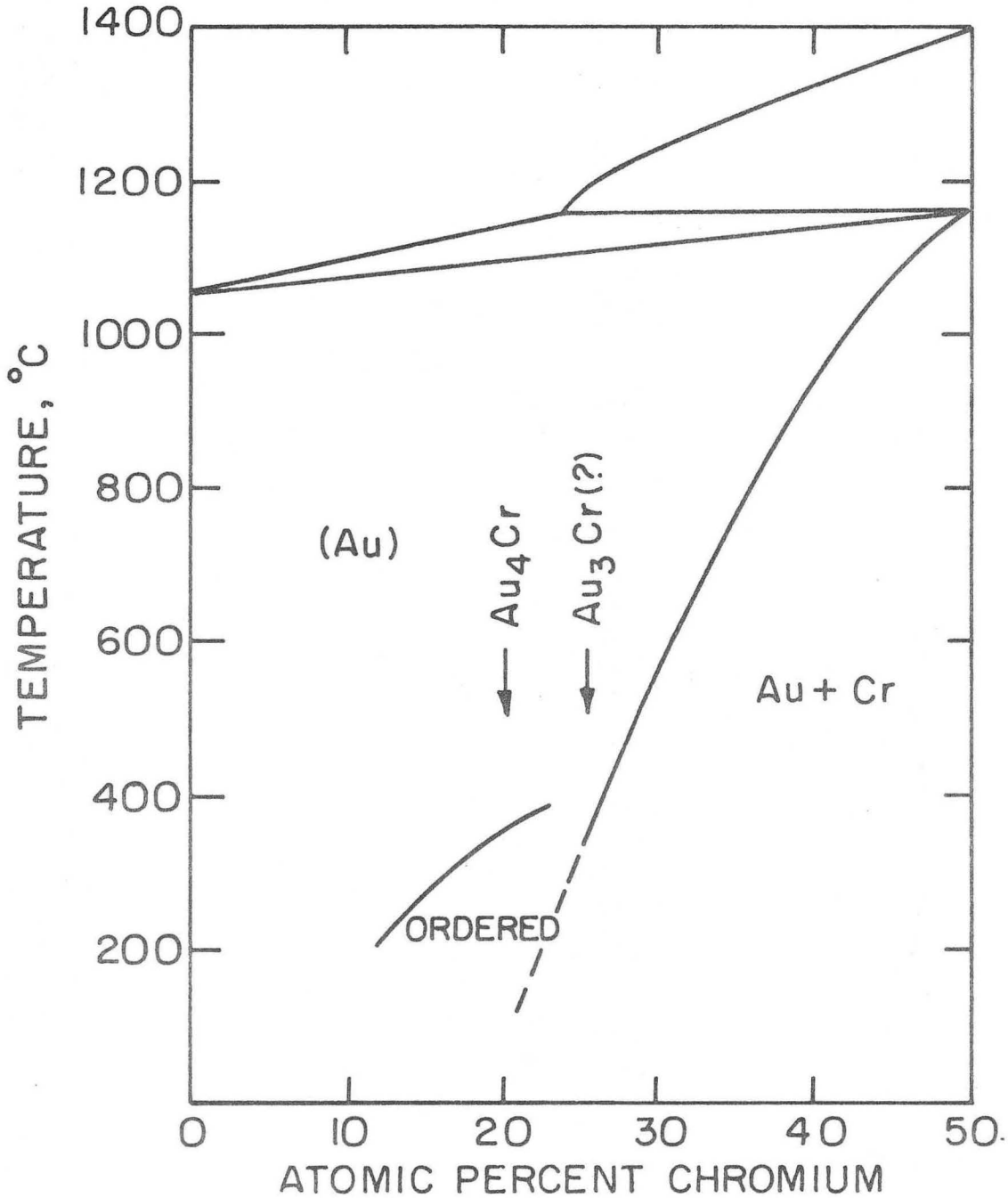

XBL 7110-7332

Fig. 14

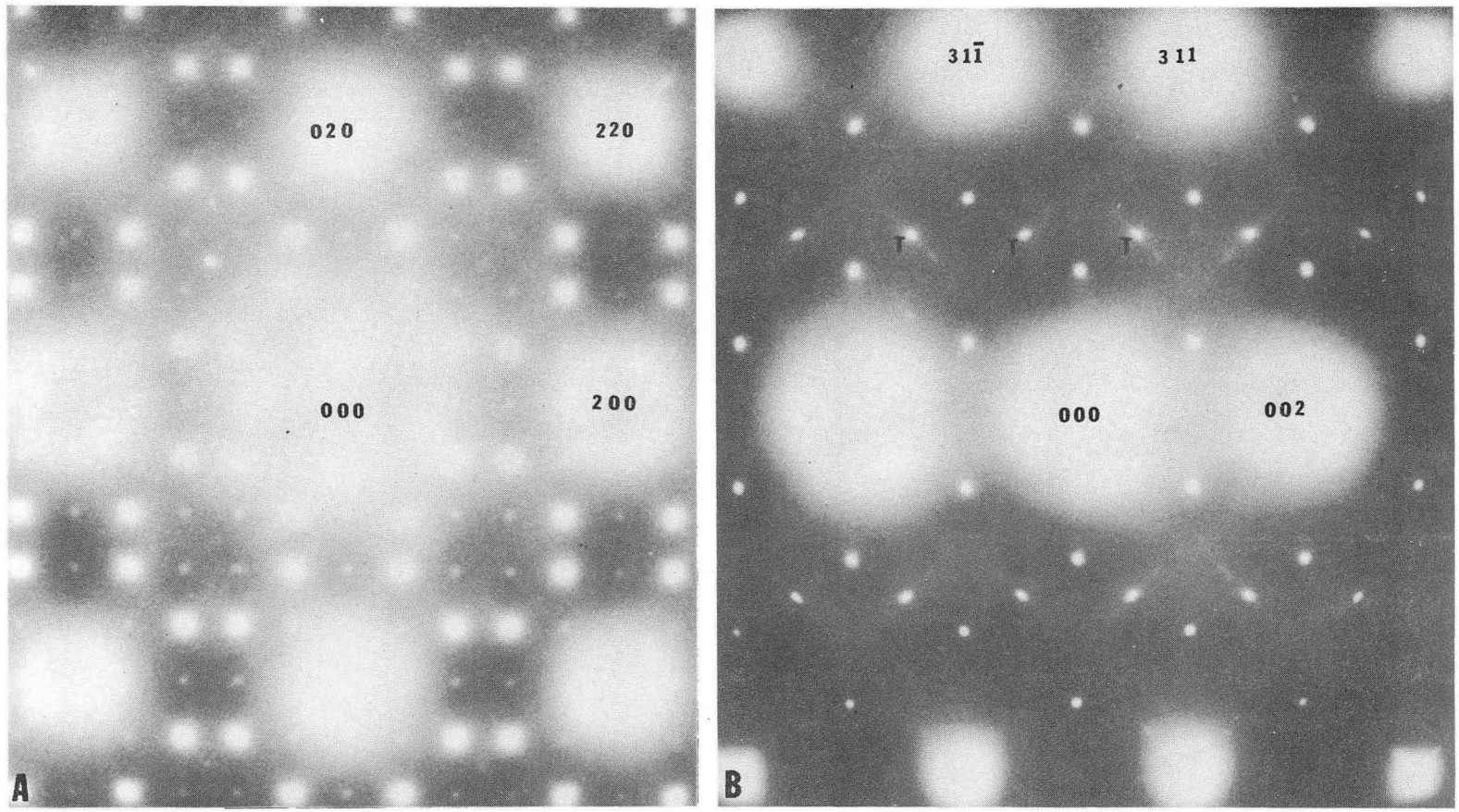

XBB 717-3405

Fig 15

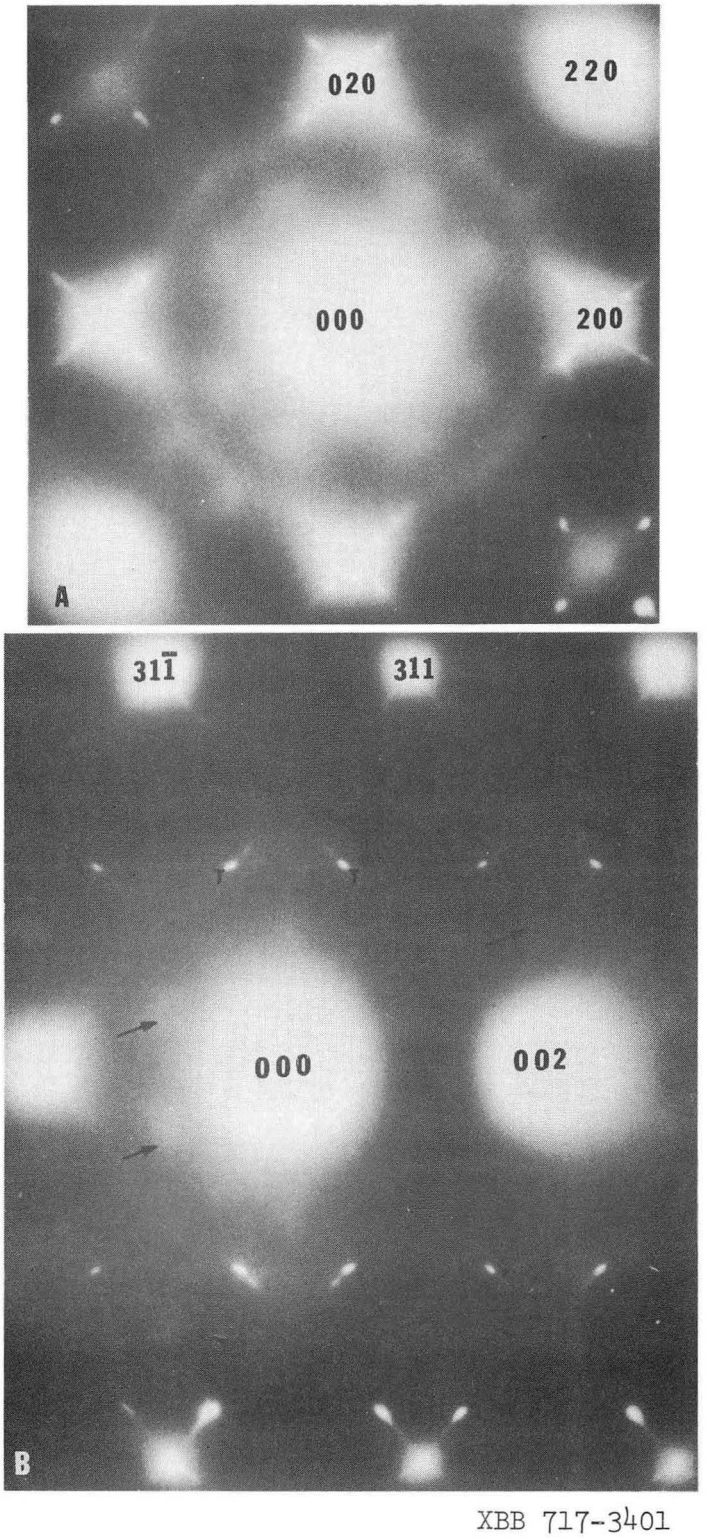

XBB 717-3401

Fig. 16

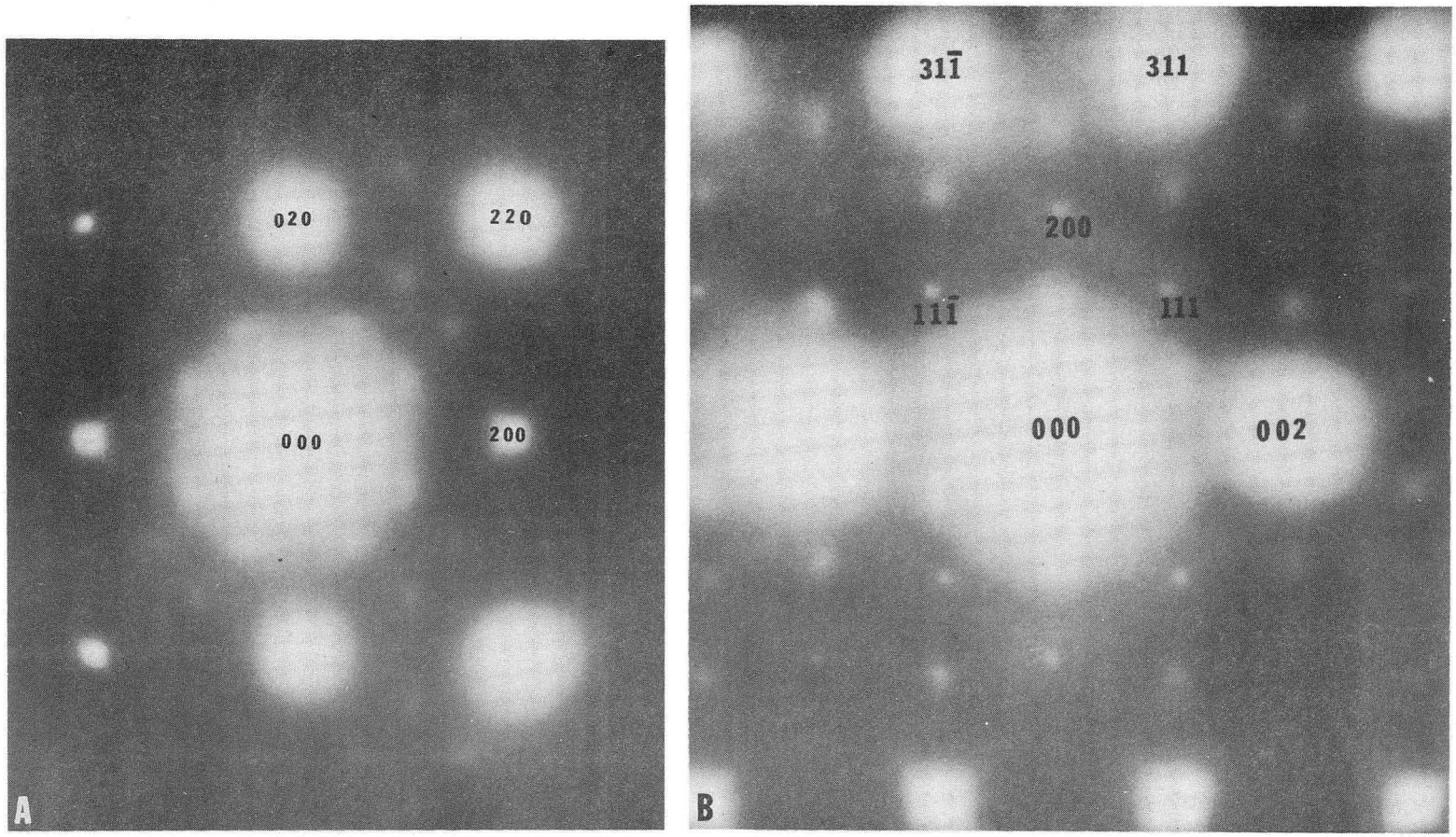

XBB 717-3404

Fig. 17

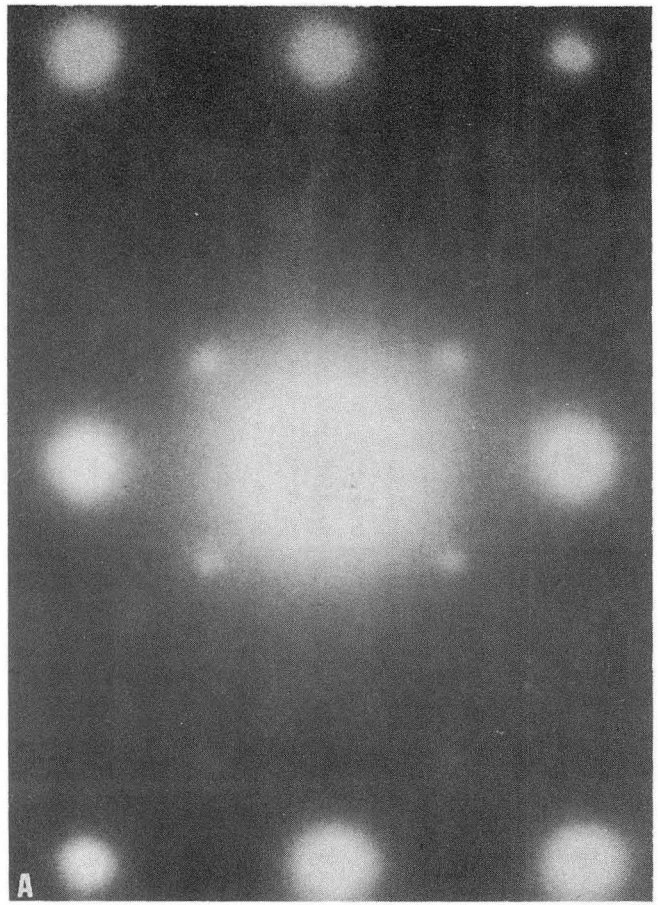

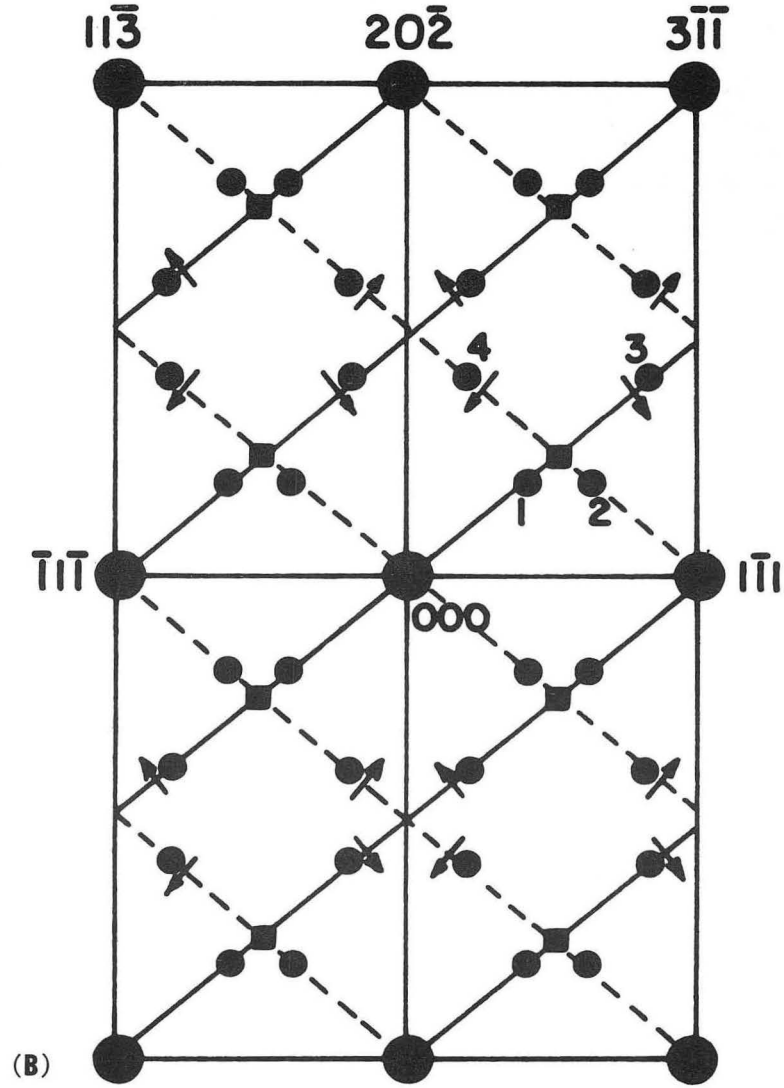

XBB 717-3390

Fig. 18

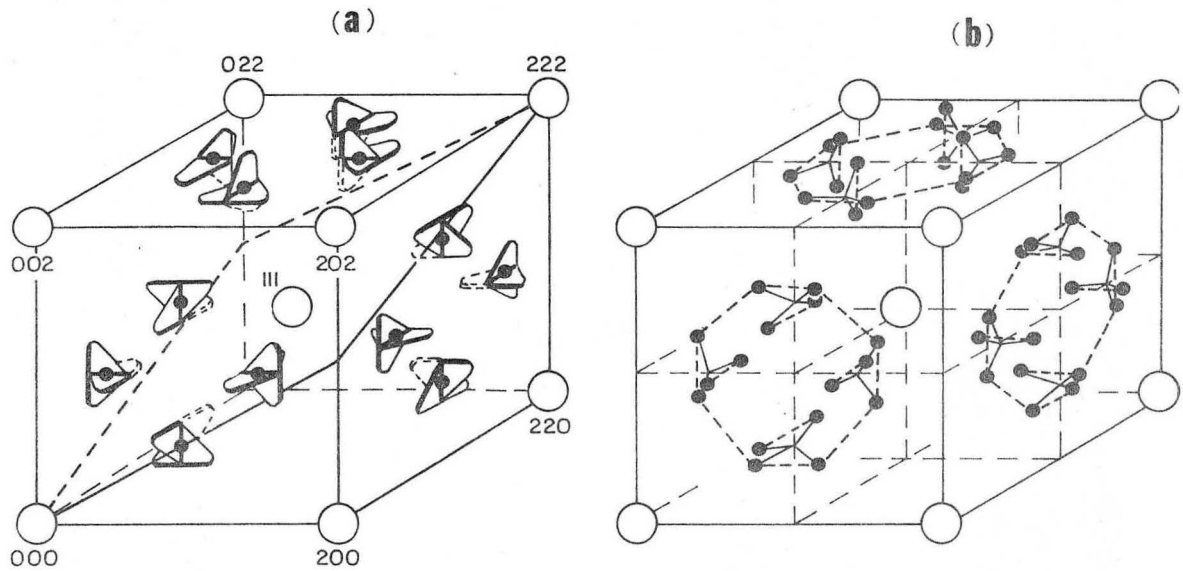

Disordered state

LRO state: 6 variants of D1a

Reciprocal lattices of Au_3Cr

XBL713-6626

Fig. 19

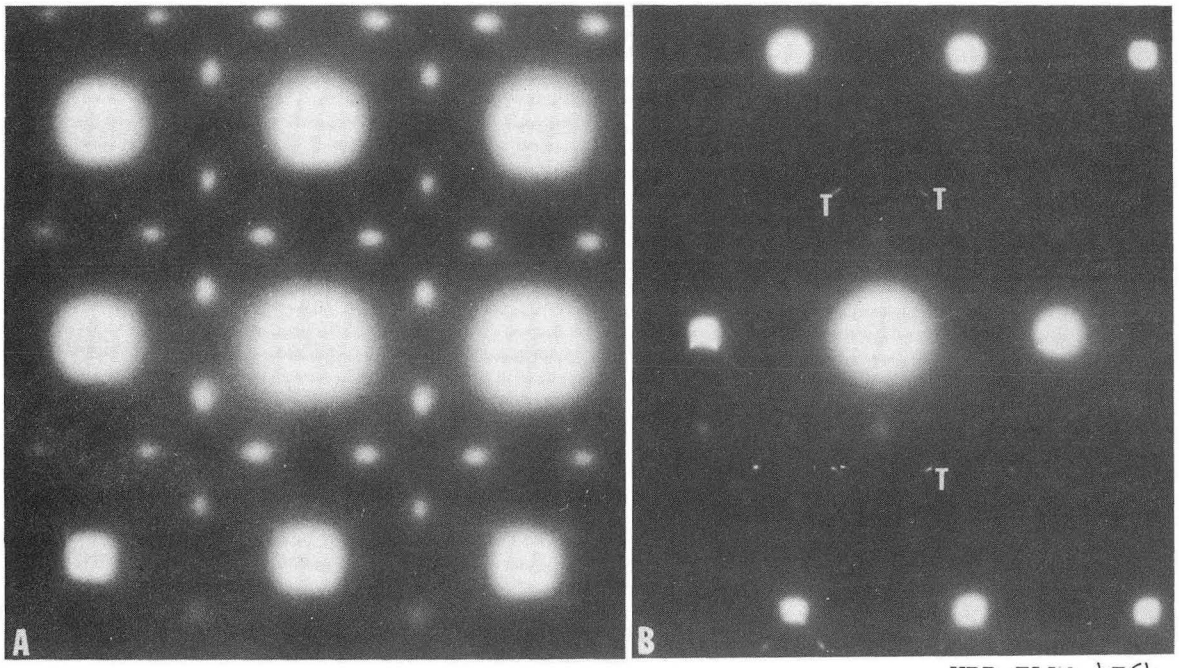

XBB 7110-4764

Fig. 20

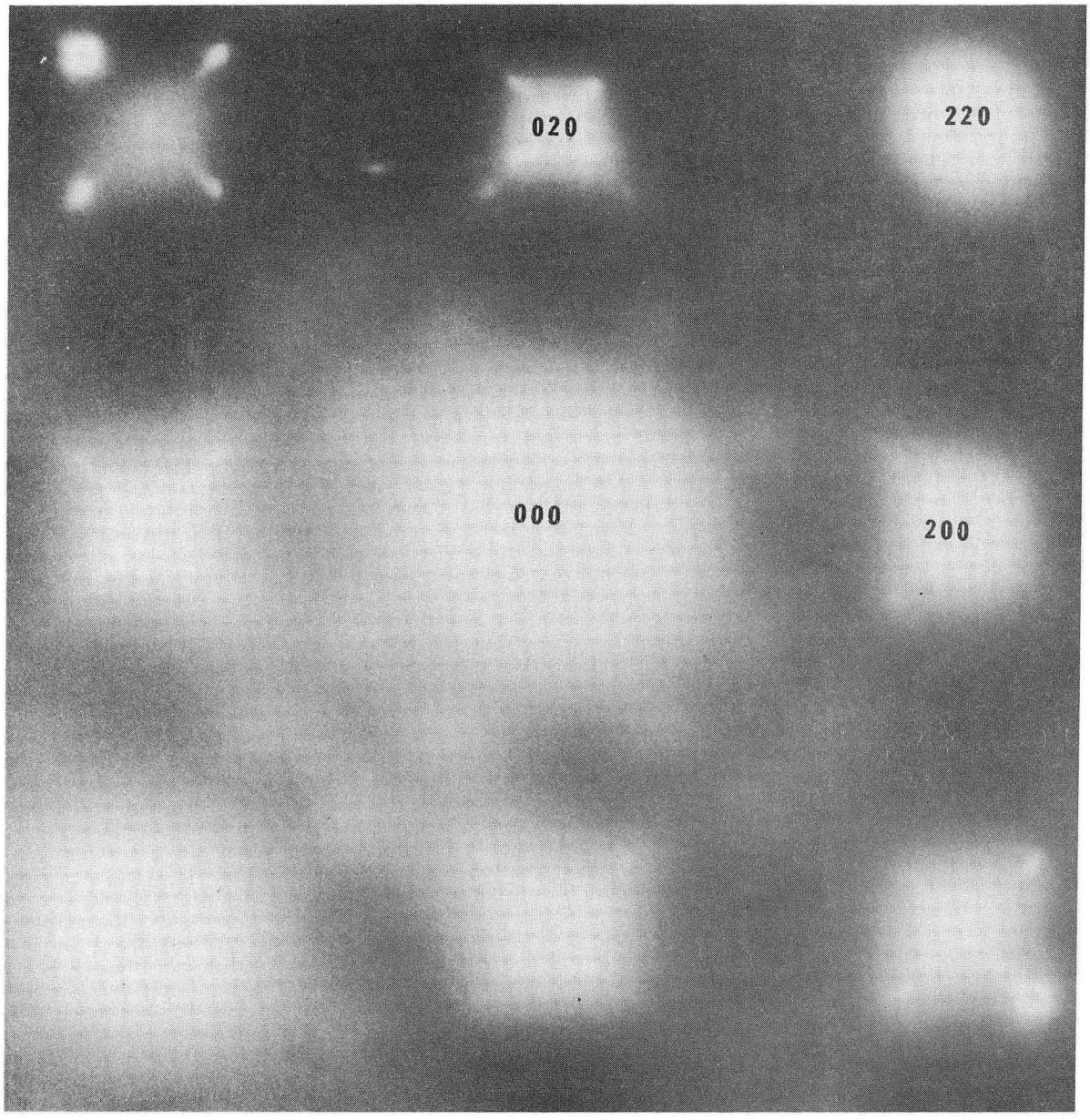

XBB 717-3412

Fig. 21

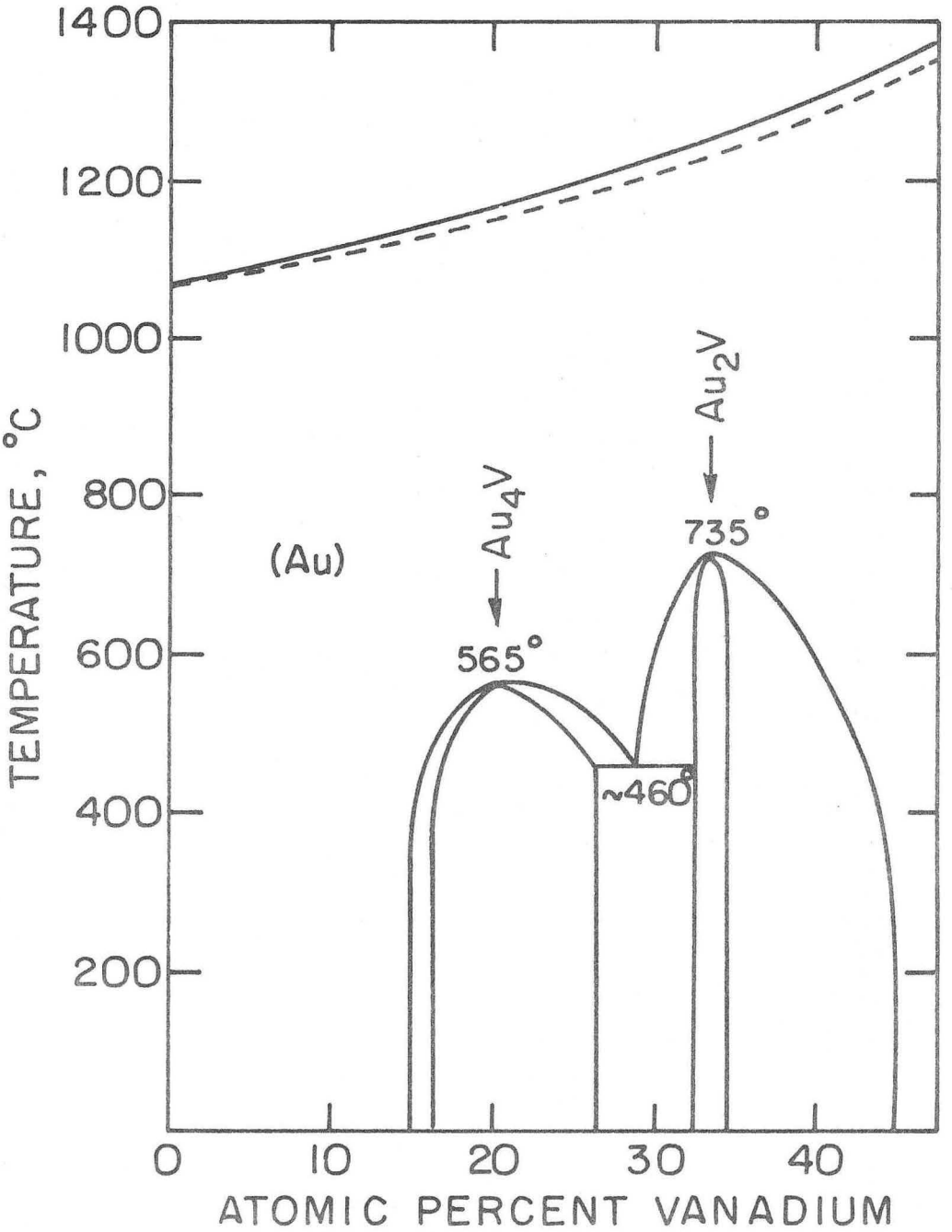

XBL7110-7331

Fig. 22

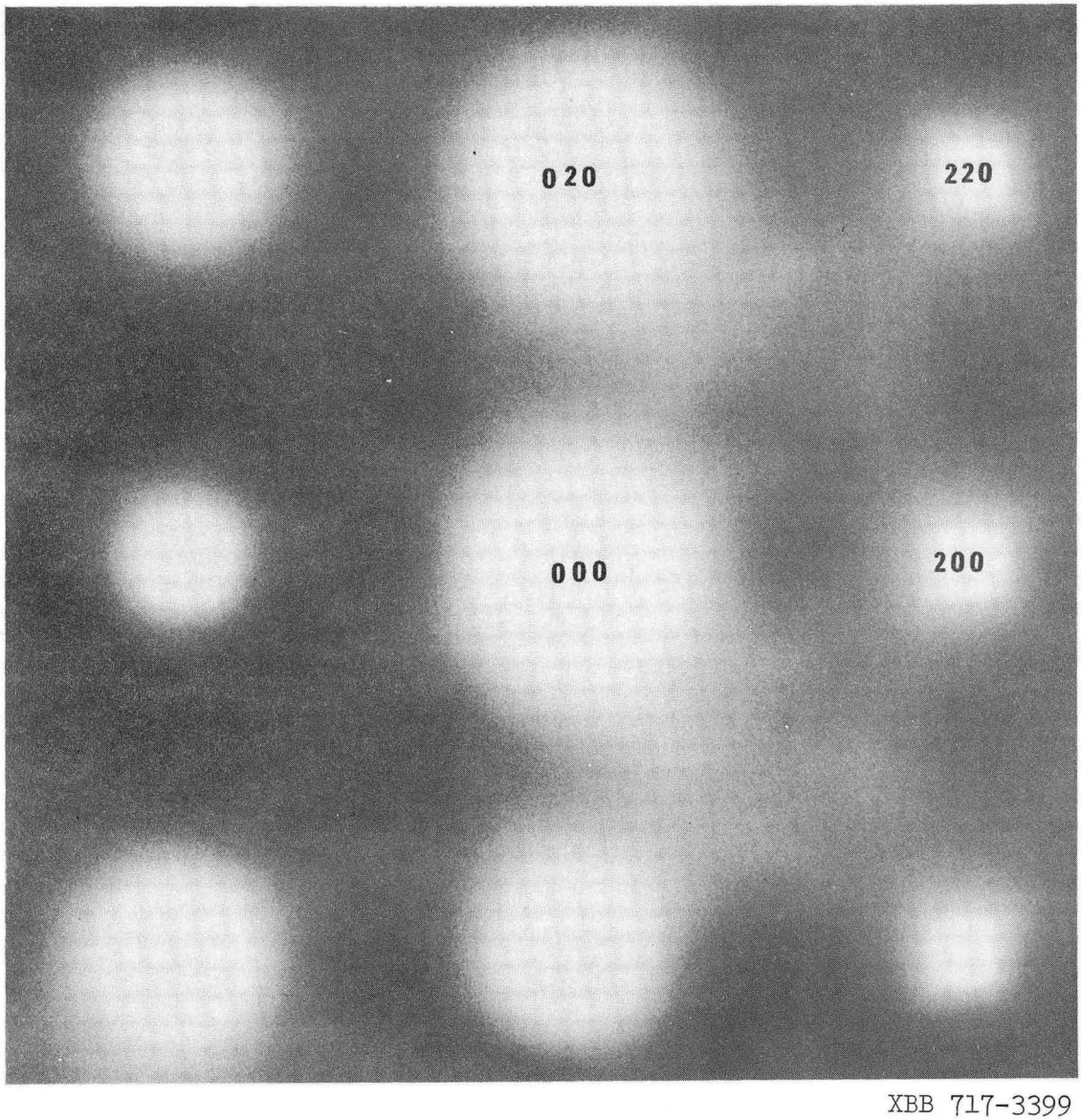

XBB 717-3399

Fig. 23

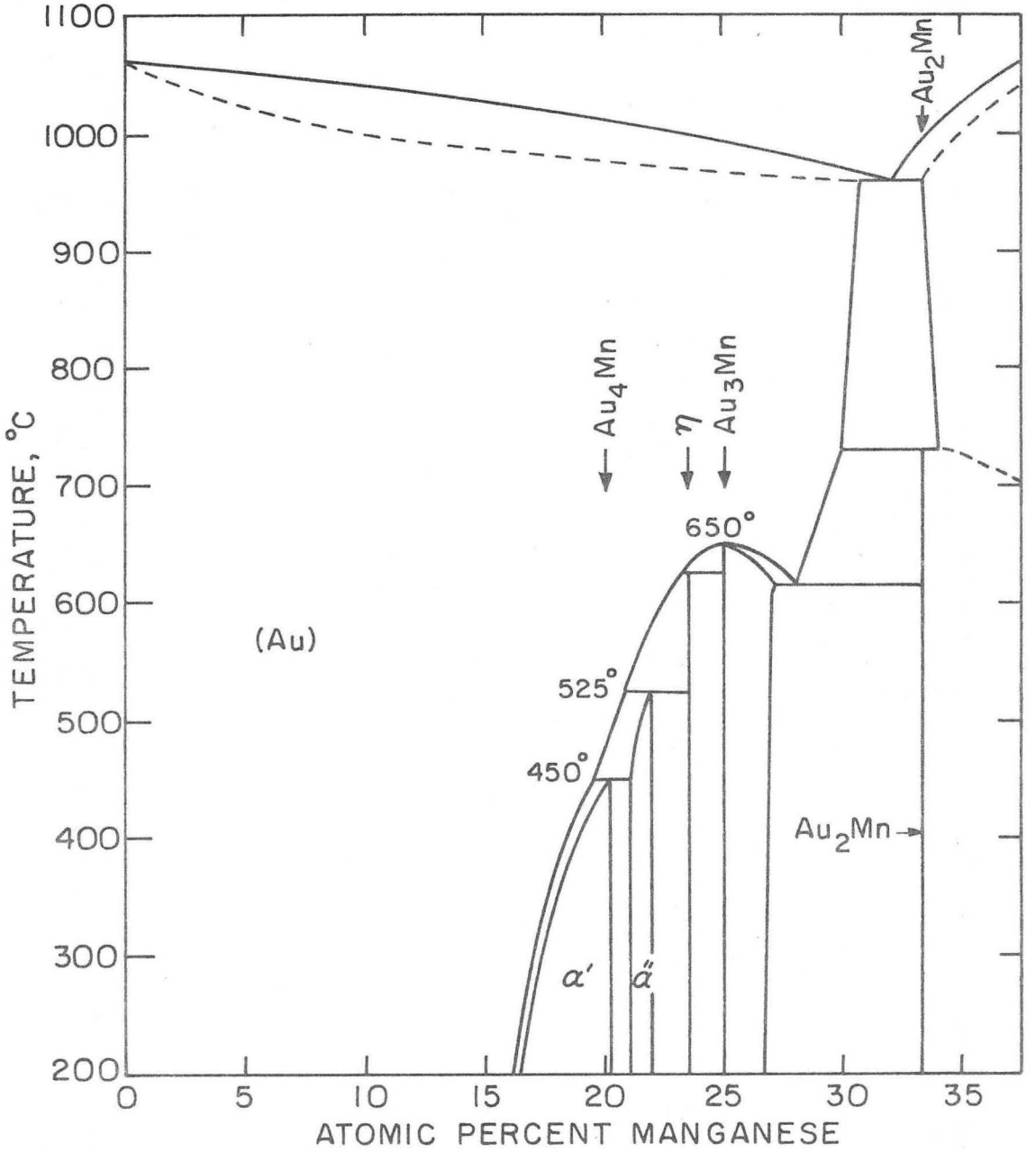

XBL 7110-7330

Fig. 24

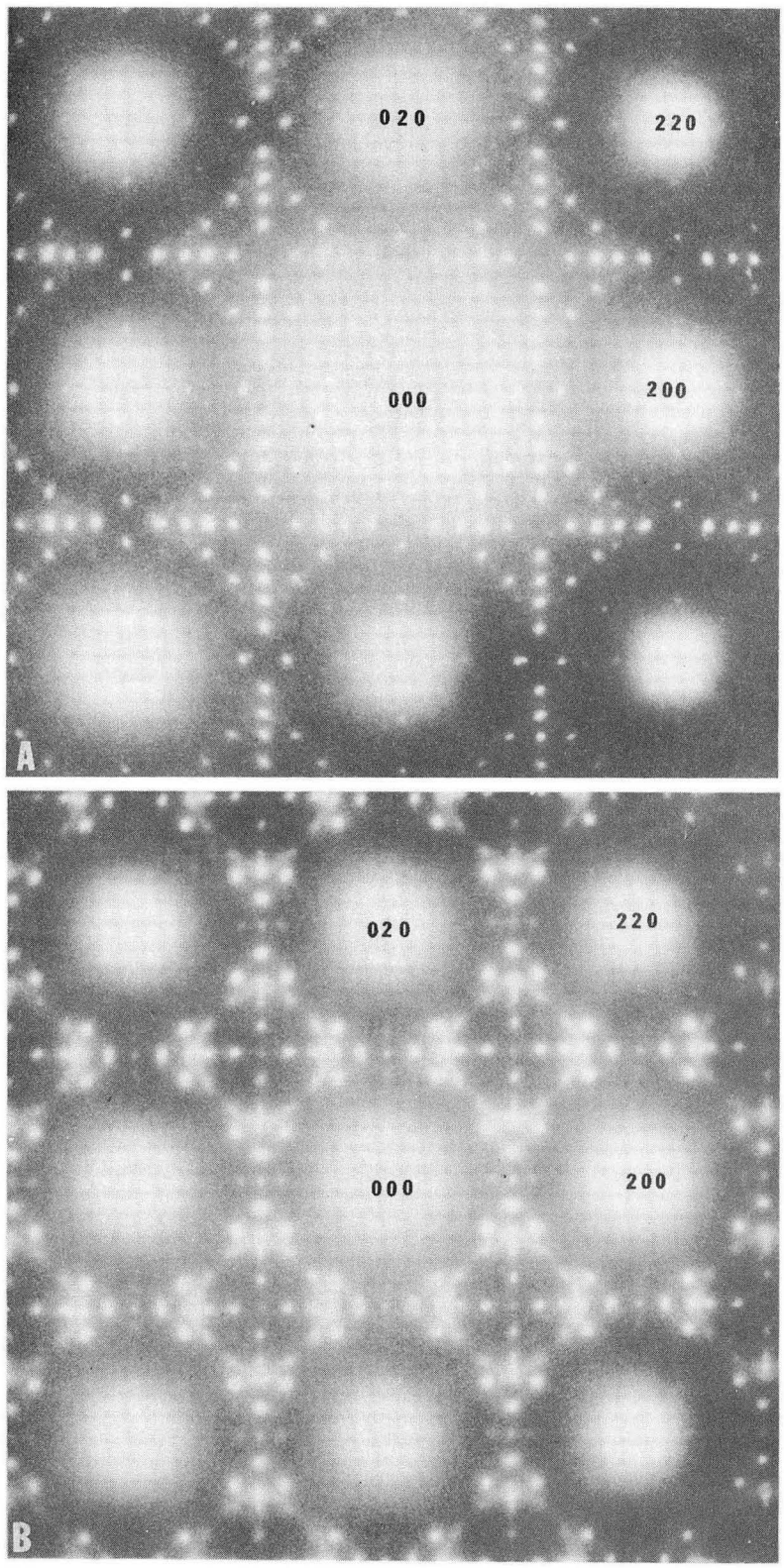

XBB 717-3414

Fig. 25

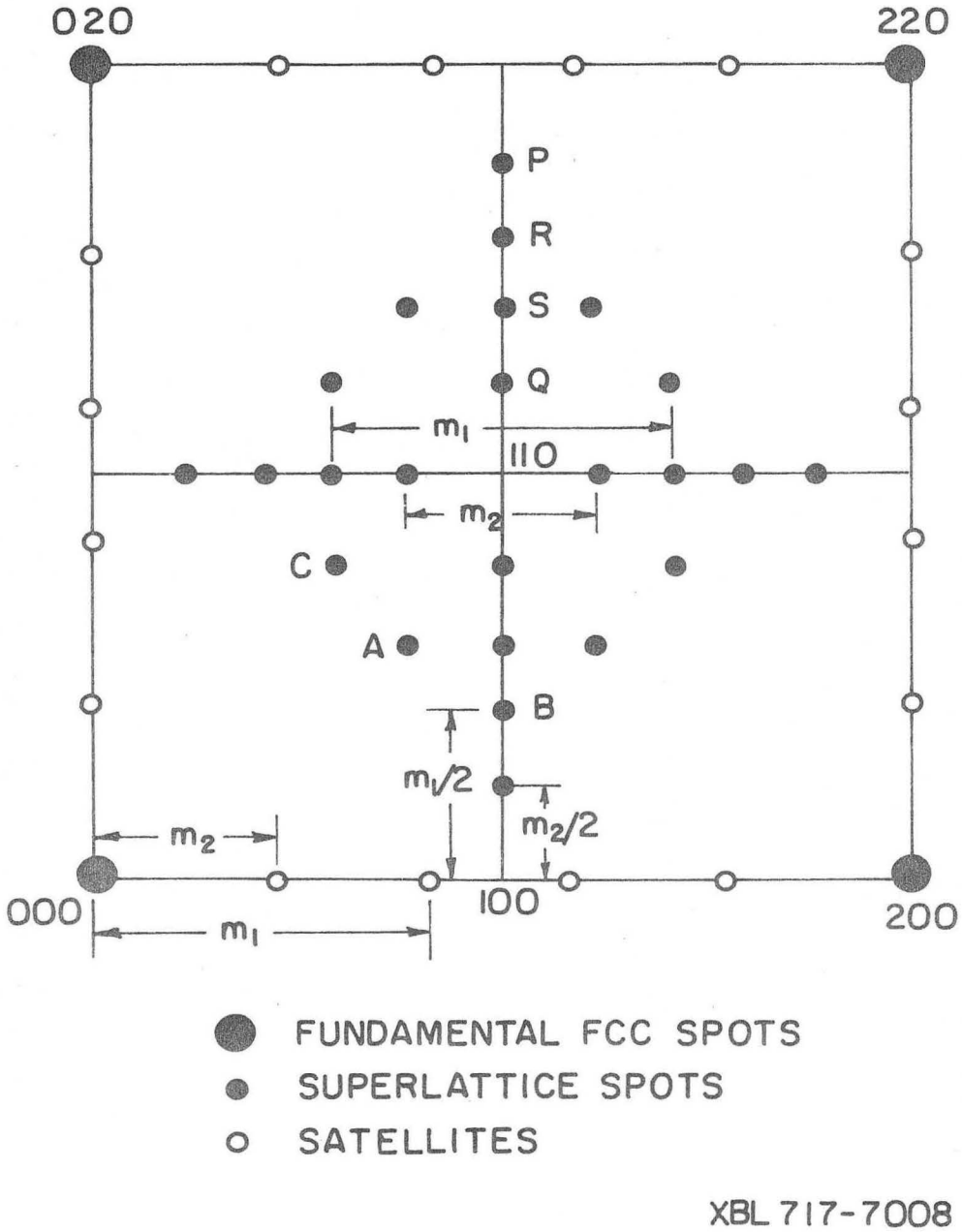
020
220
P
R
S
Q
m_1
110
m_2
C
A
B
$m_1/2$
$m_2/2$
m_2
000
100
200
m_1
FUNDAMENTAL FCC SPOTS
SUPERLATTICE SPOTS
SATELLITES
XBL 717-7008

Fig. 25c

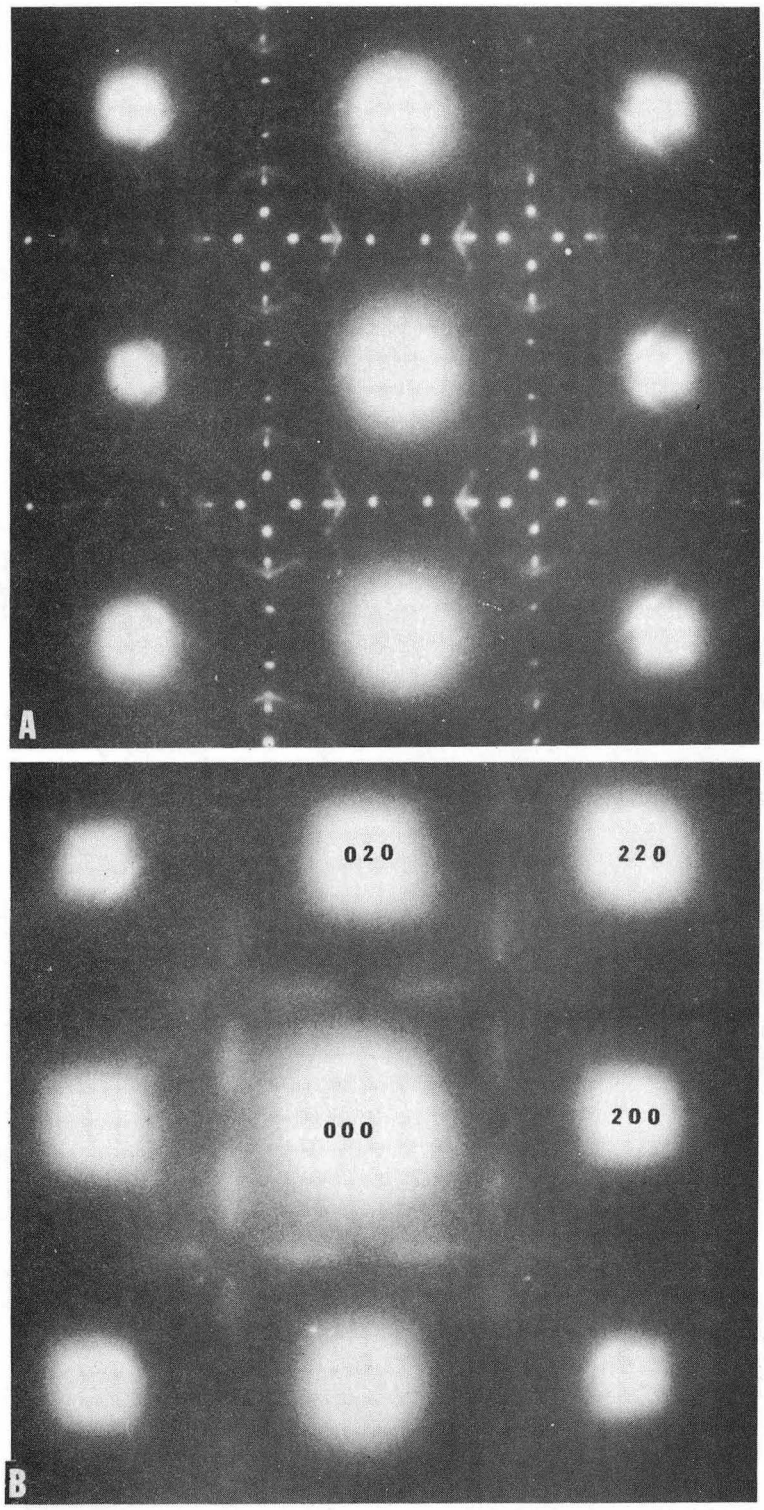

XBB 7110-4762

Fig. 26

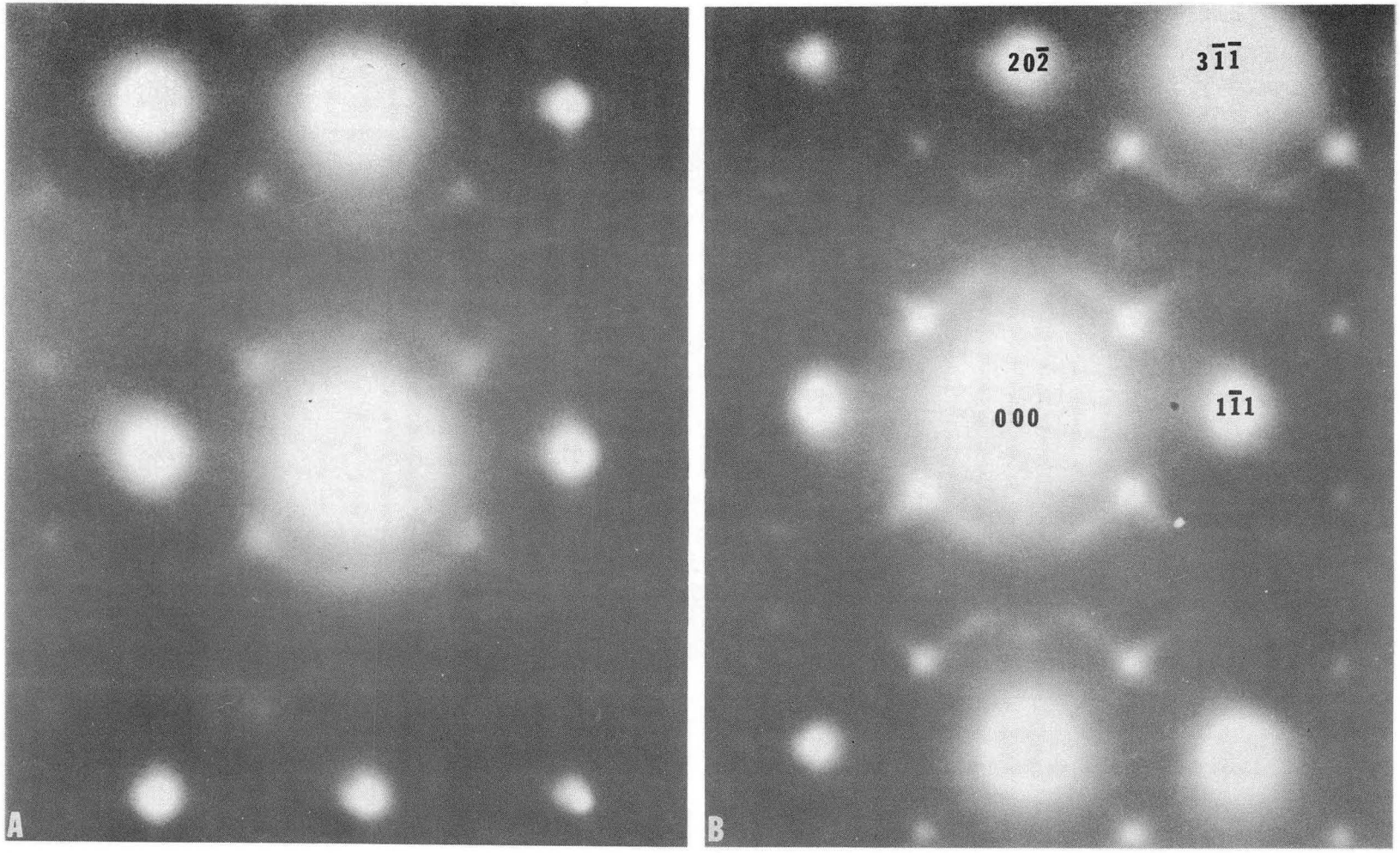

Fig. 27

XBB 717-3413

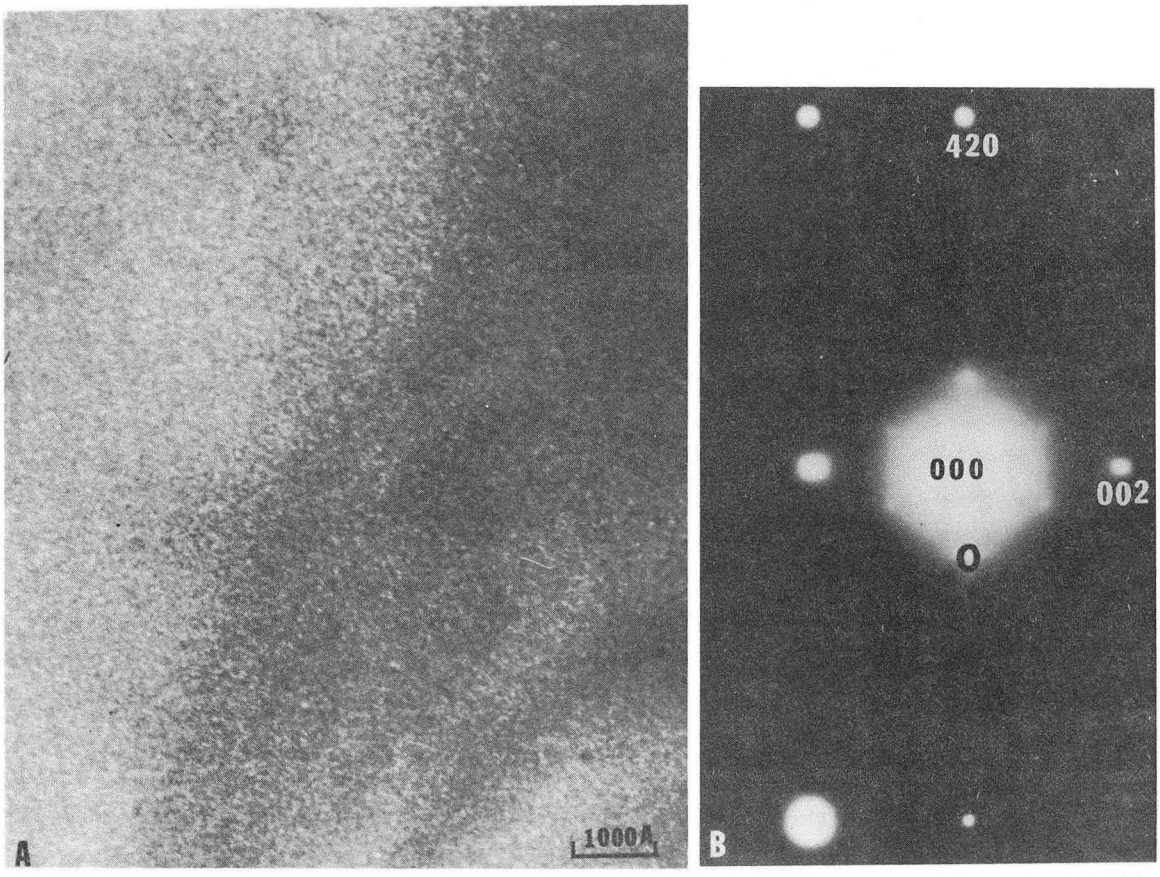

XBB 7110-4766

Fig. 28

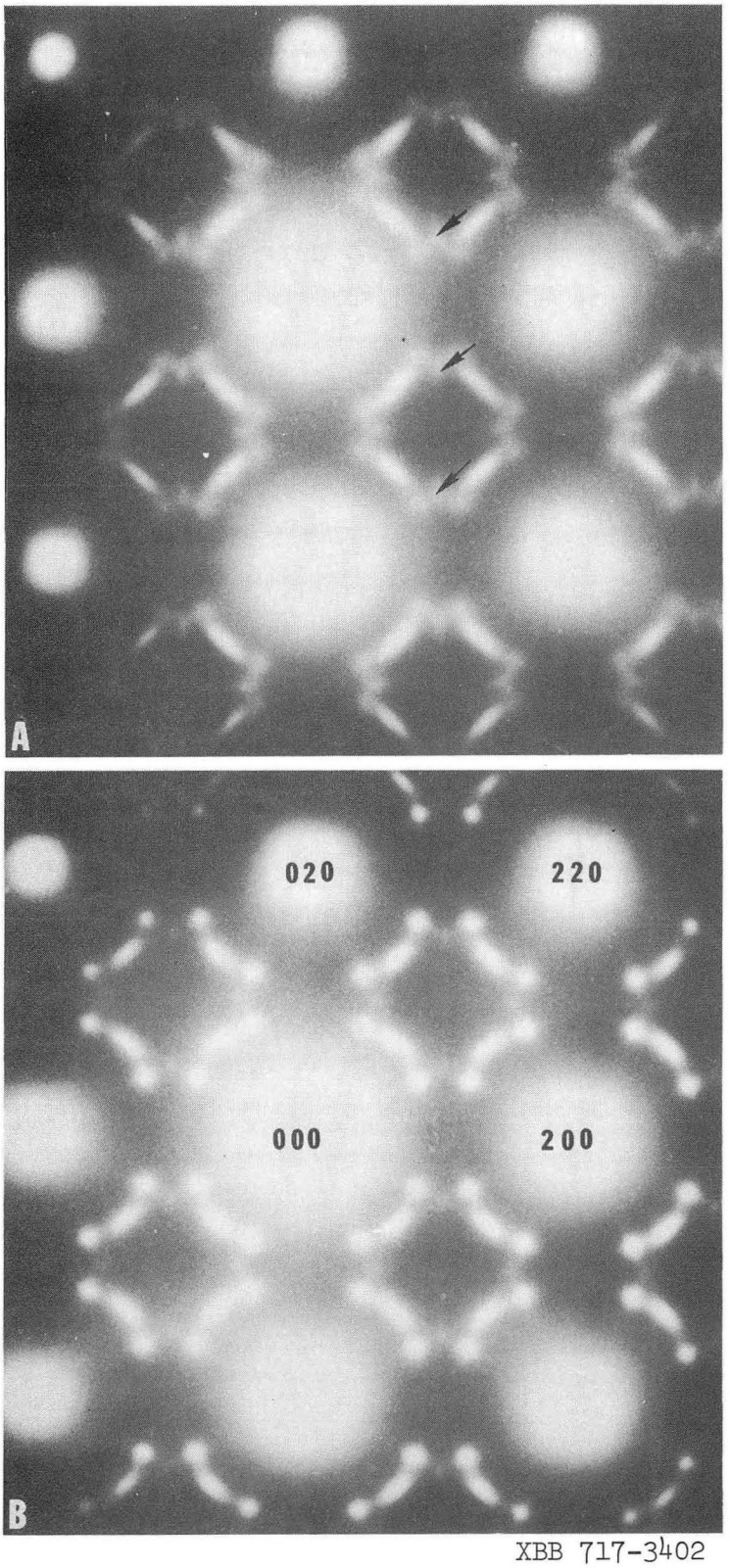

XBB 717-3402

Fig. 29

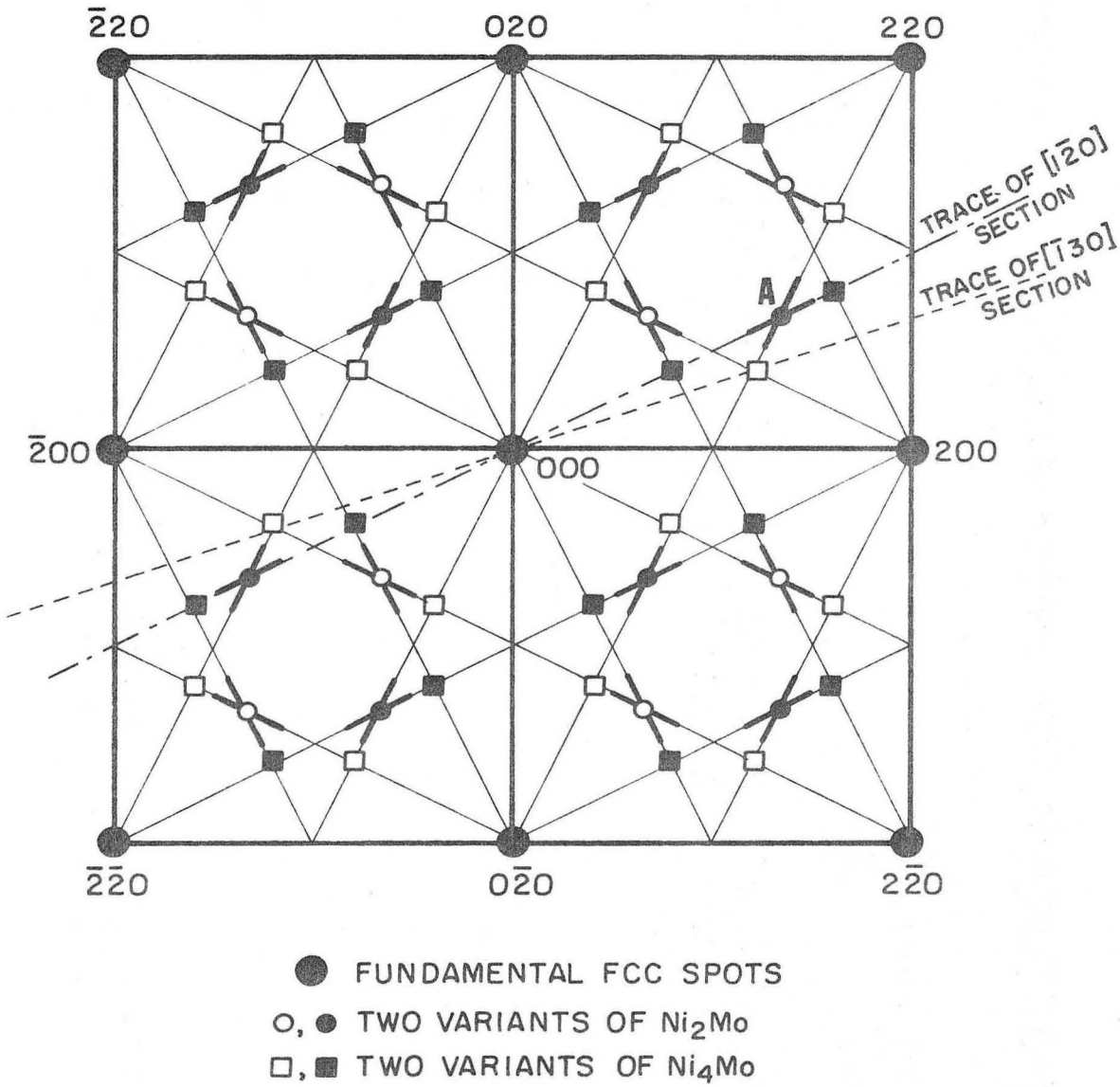

XBL 717-1217

Fig. 29c

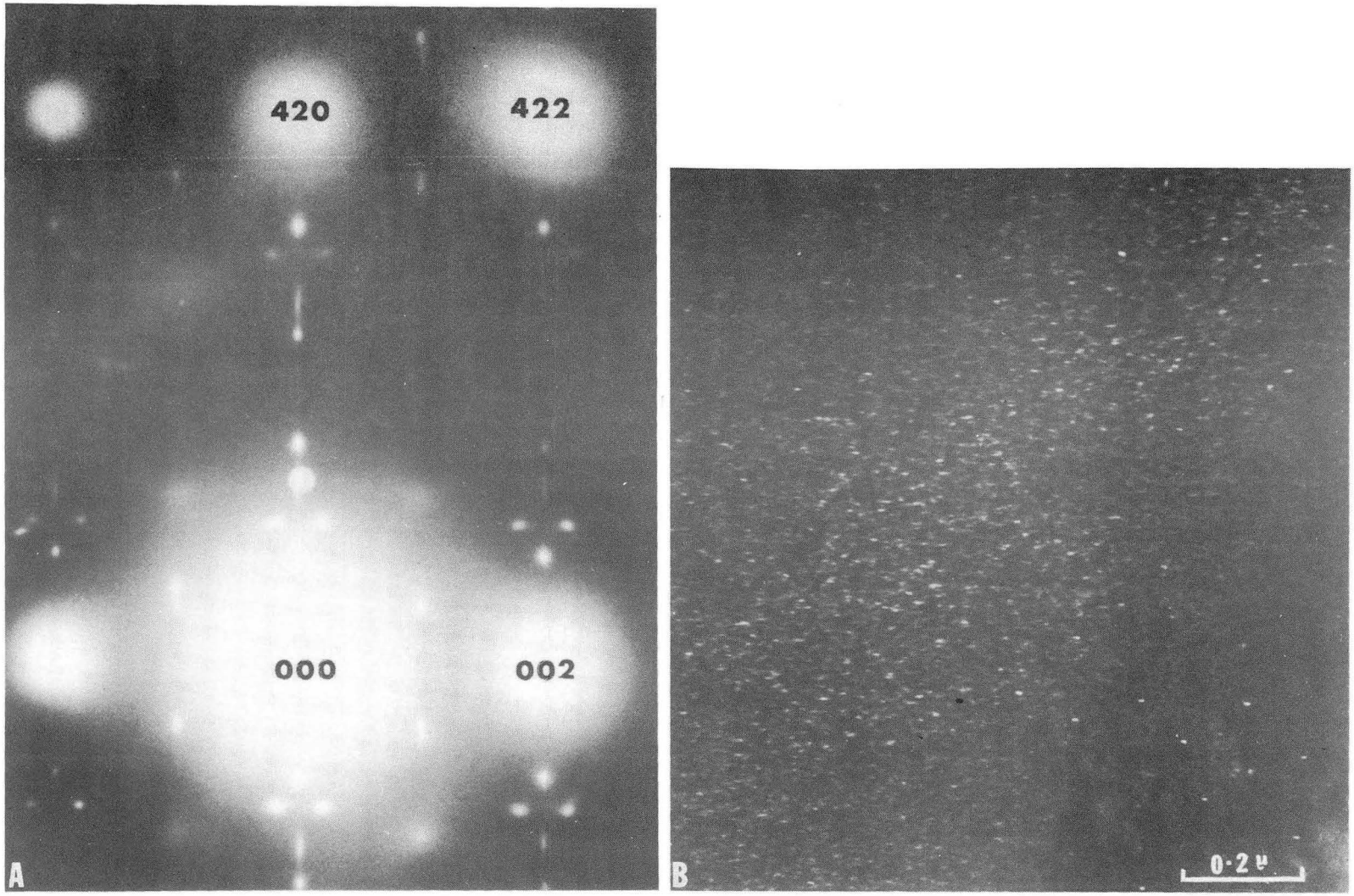

Fig. 30

XBB 717-3403

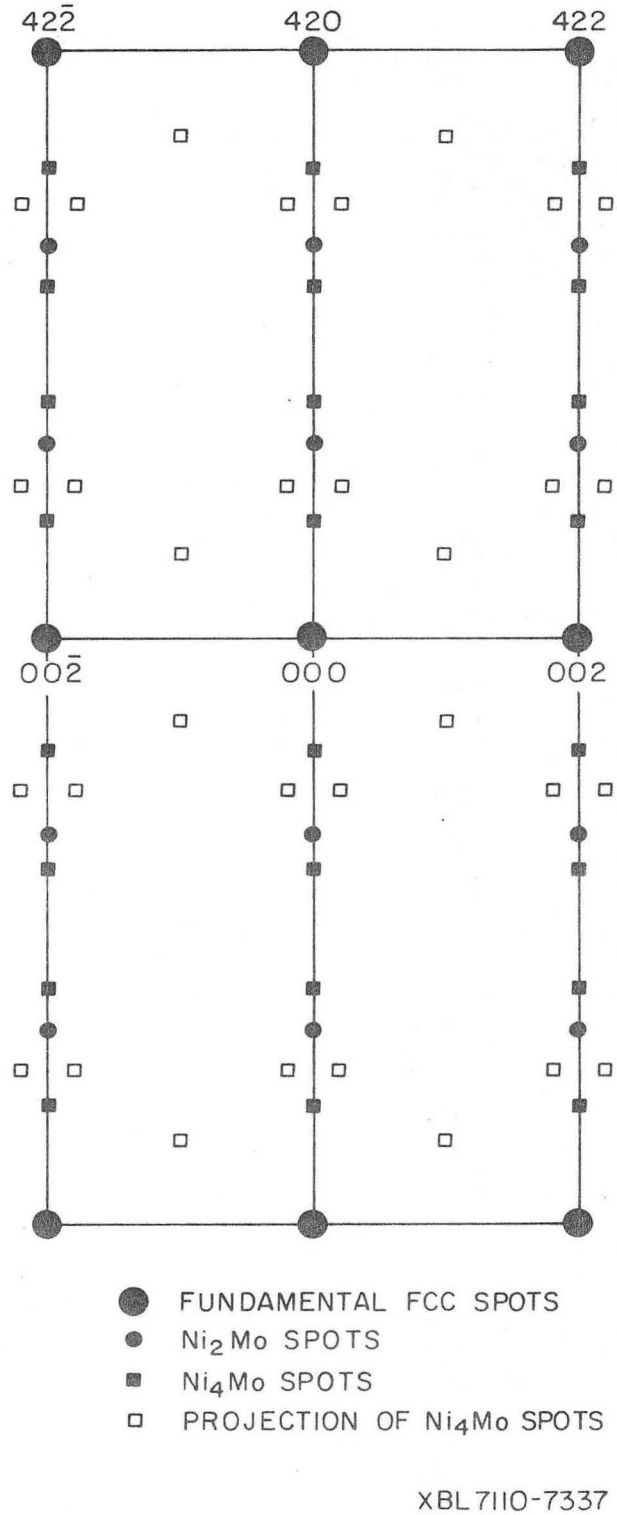
42$\bar{2}$
420
422
00$\bar{2}$
000
002
FUNDAMENTAL FCC SPOTS
Ni_2Mo SPOTS
Ni_4Mo SPOTS
PROJECTION OF Ni_4Mo SPOTS
XBL 7110-7337

Fig. 30c

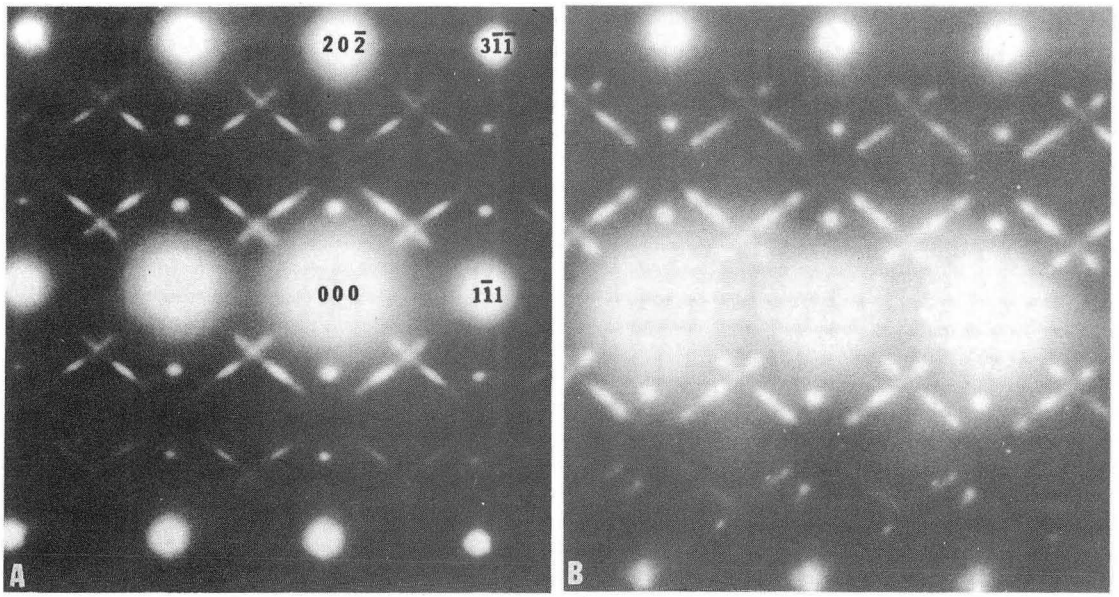

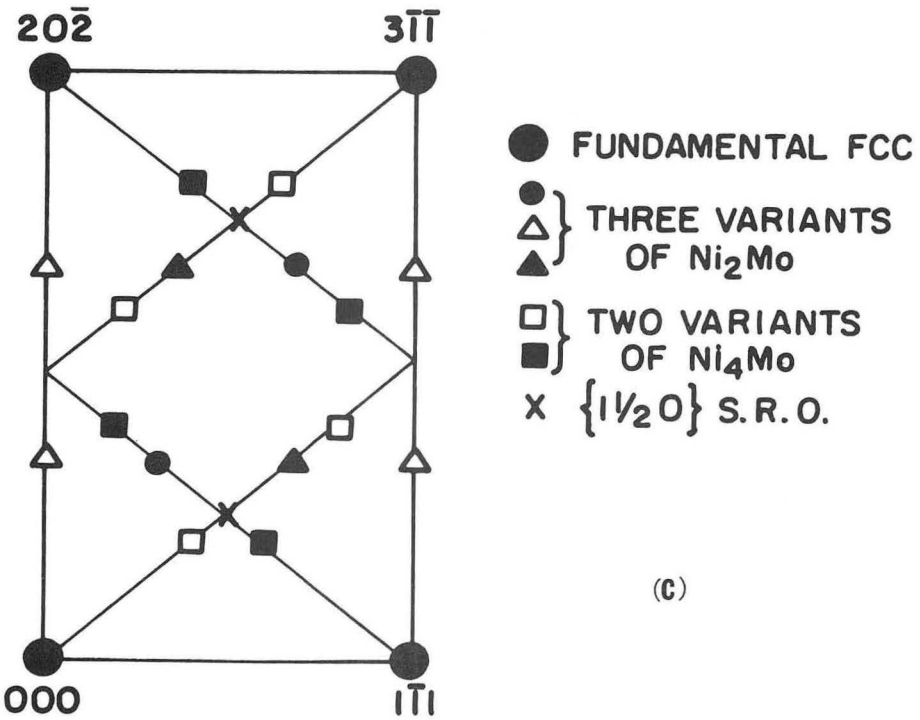

(C)

XBB 717-3398

Fig. 31

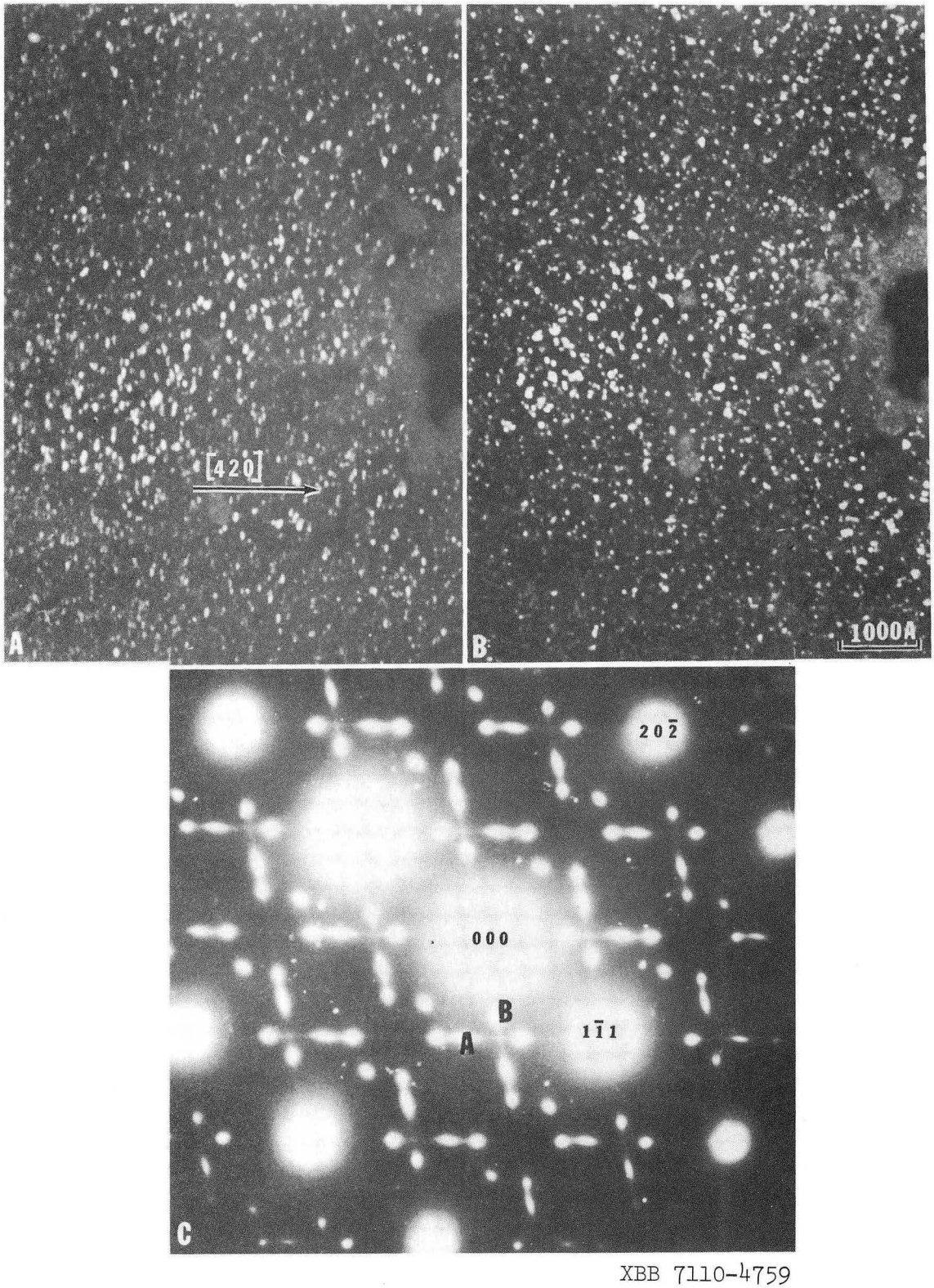

XBB 7110-4759

Fig. 32

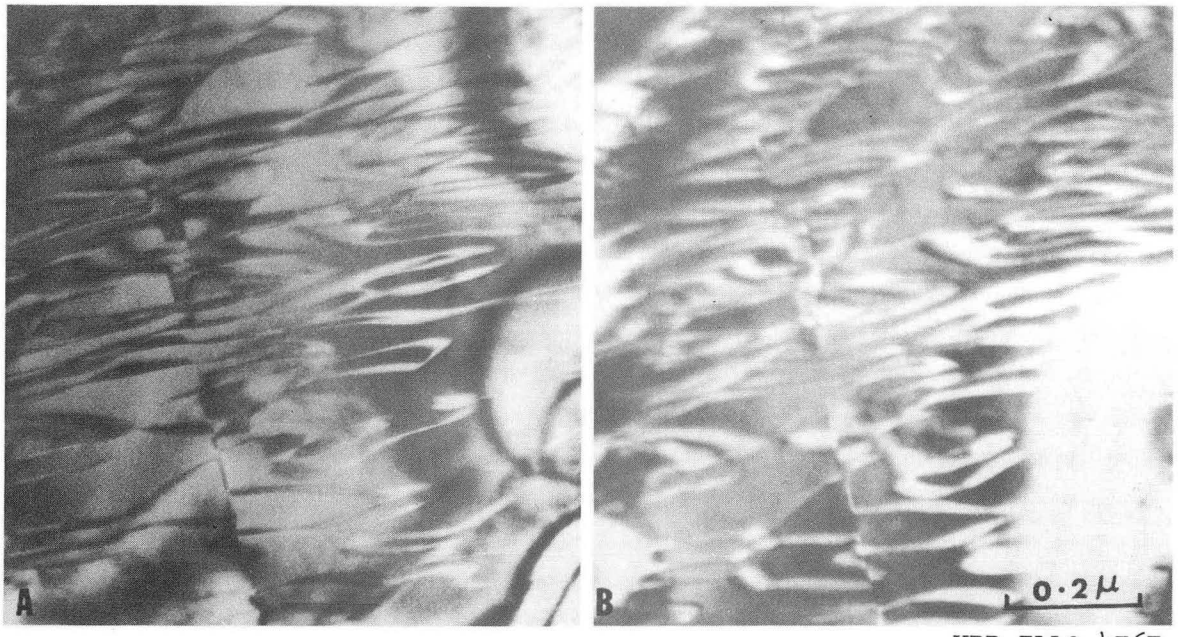

XBB 7110-4767

Fig. 33

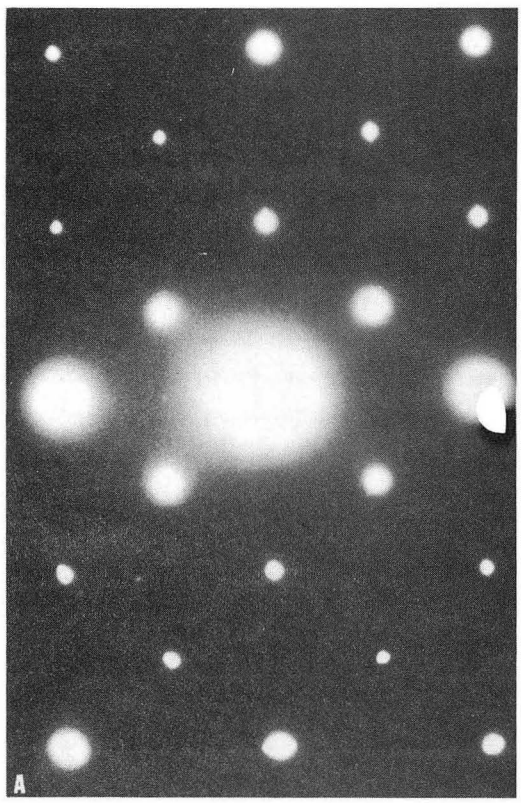

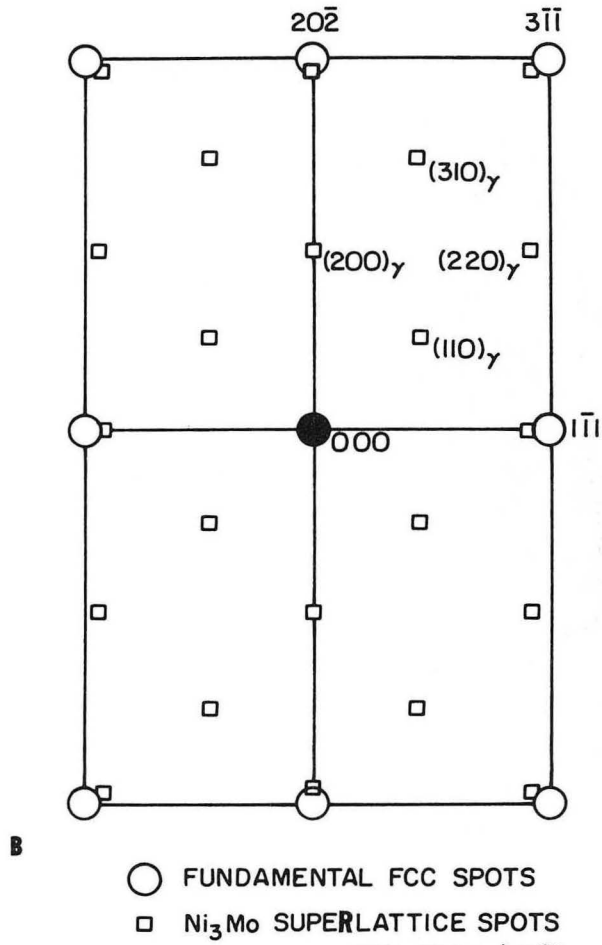

XBB 7110-4768

Fig. 34

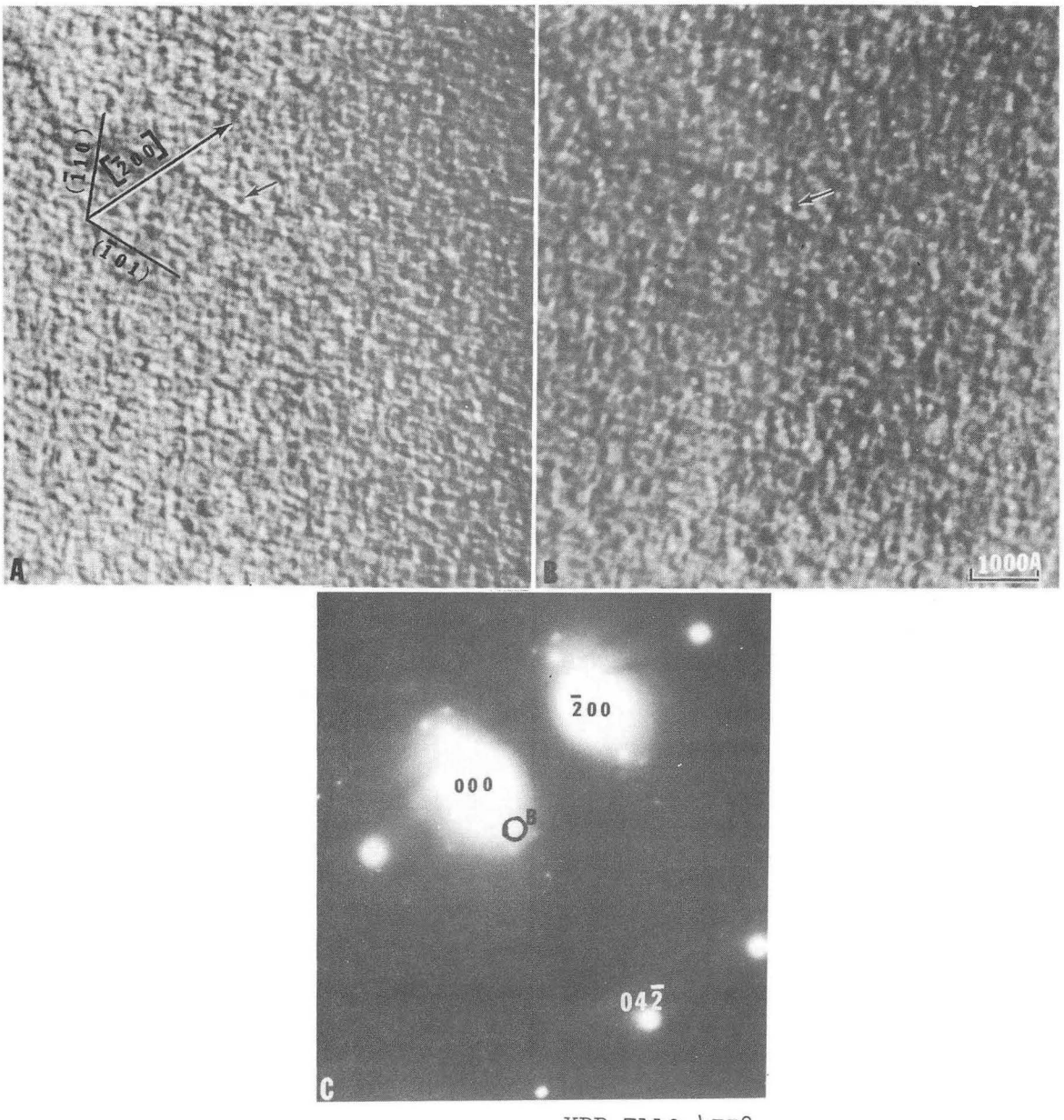

XBB 7110-4758

Fig. 35

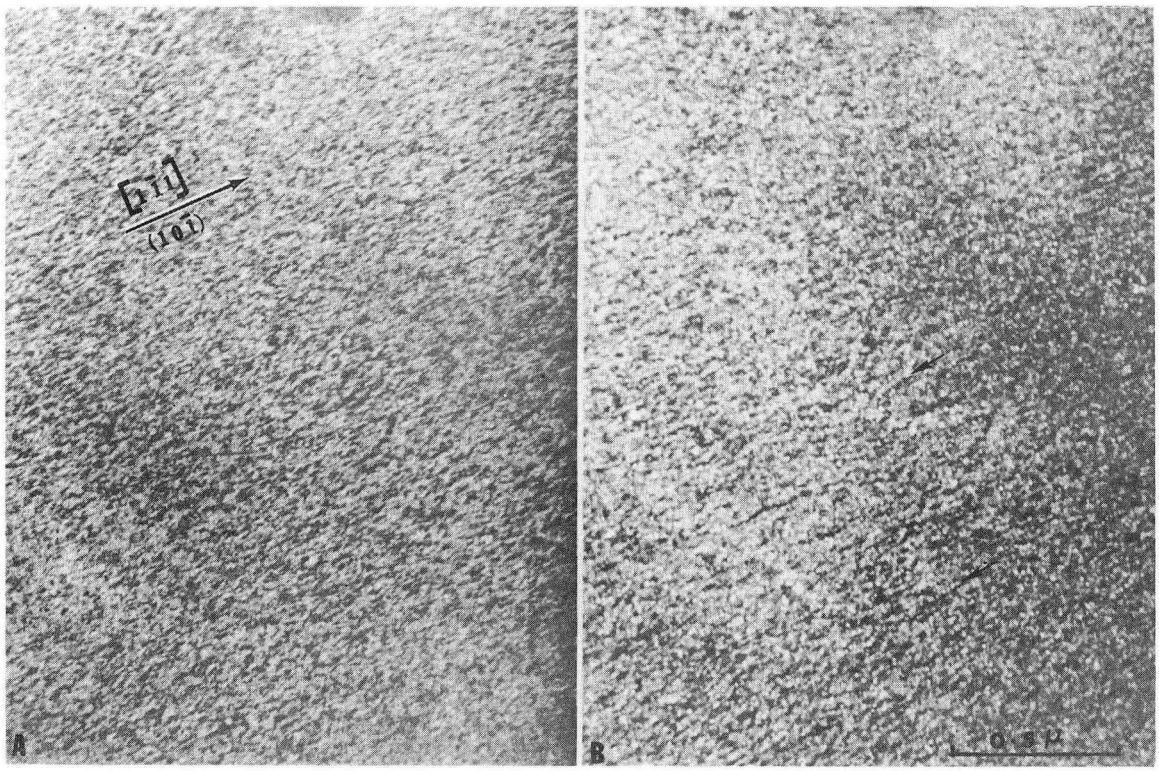

XBB 7110-4760

Fig. 36

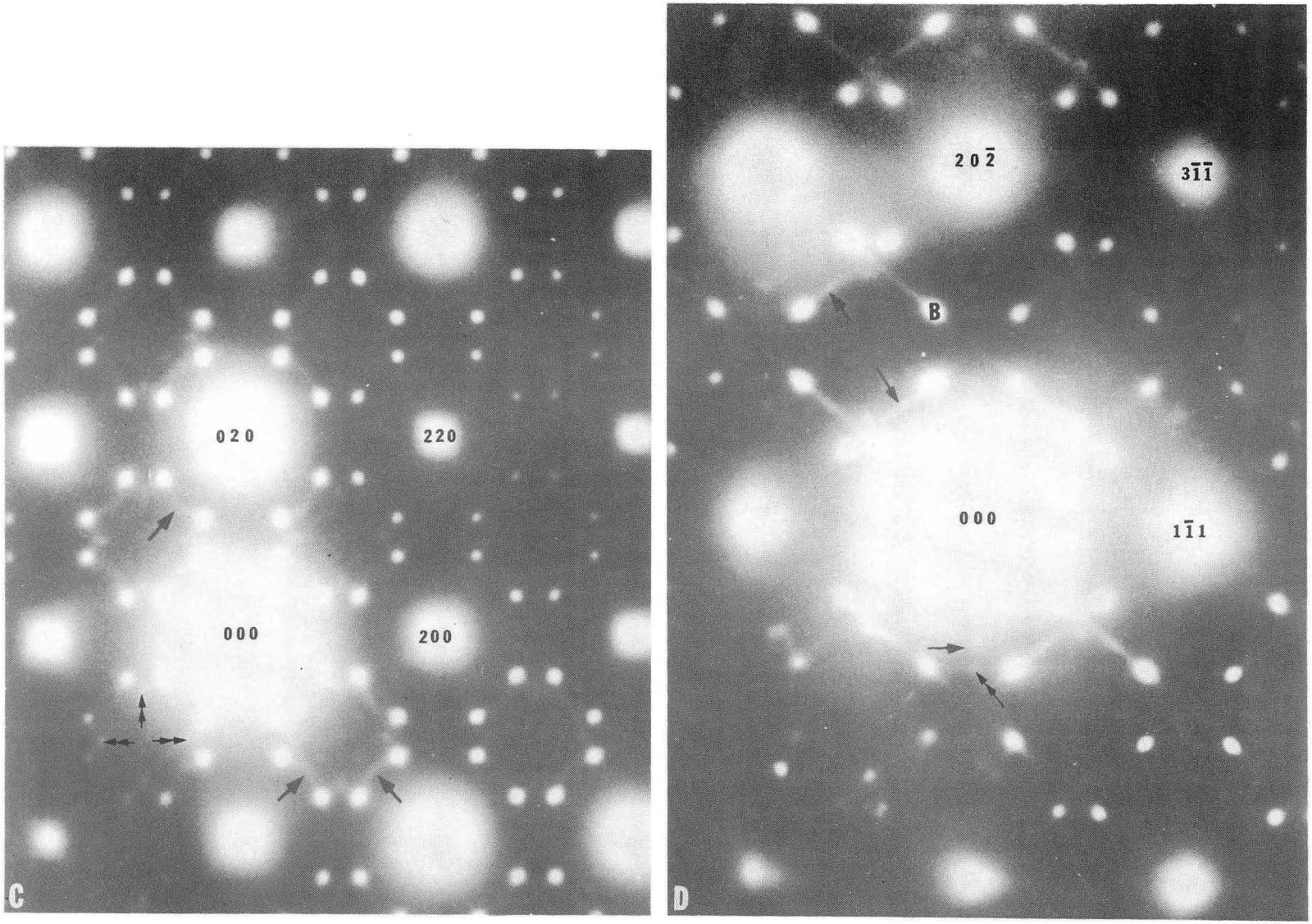

XBB 717-3407

Fig. 36 Continued

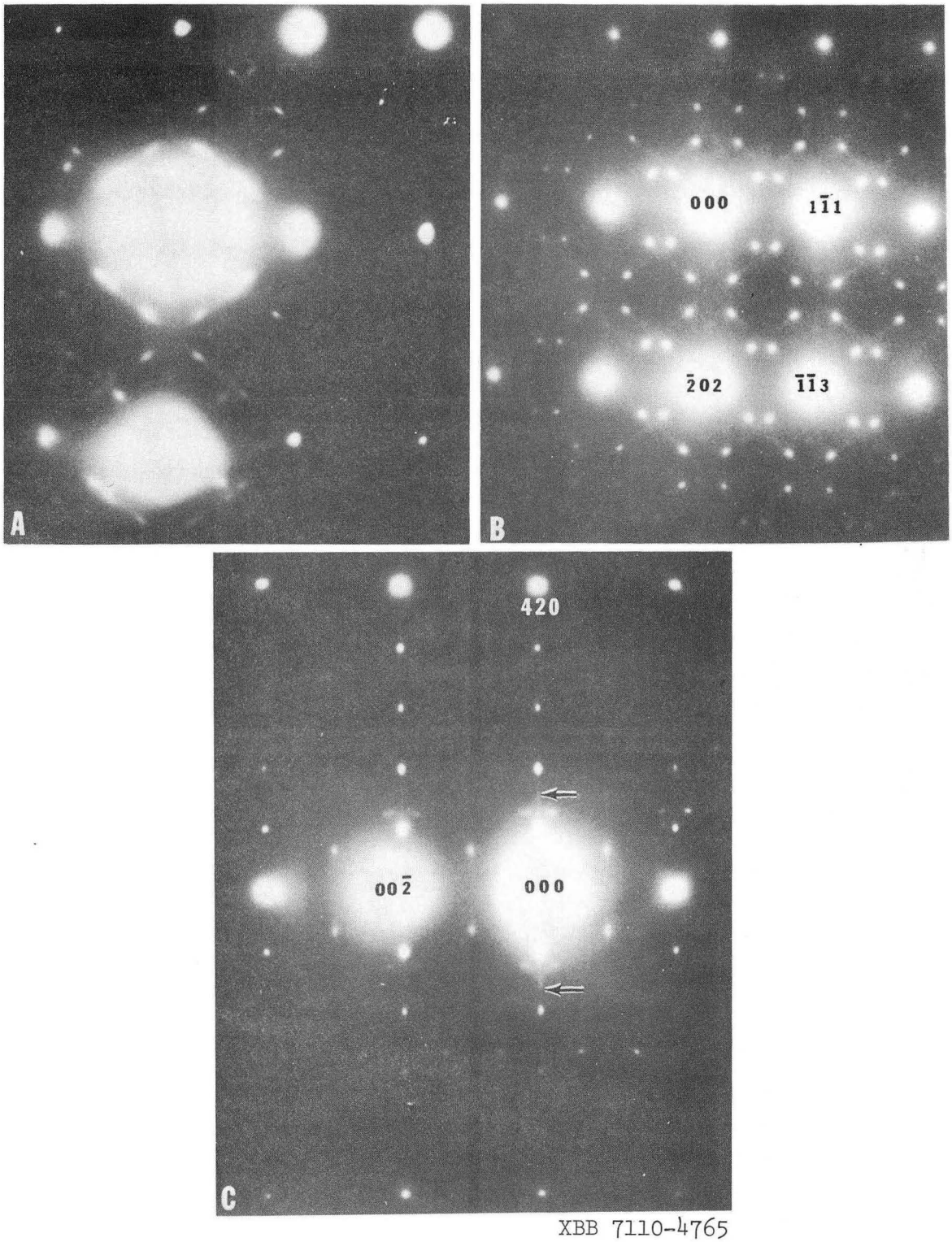

XBB 7110-4765

Fig. 37

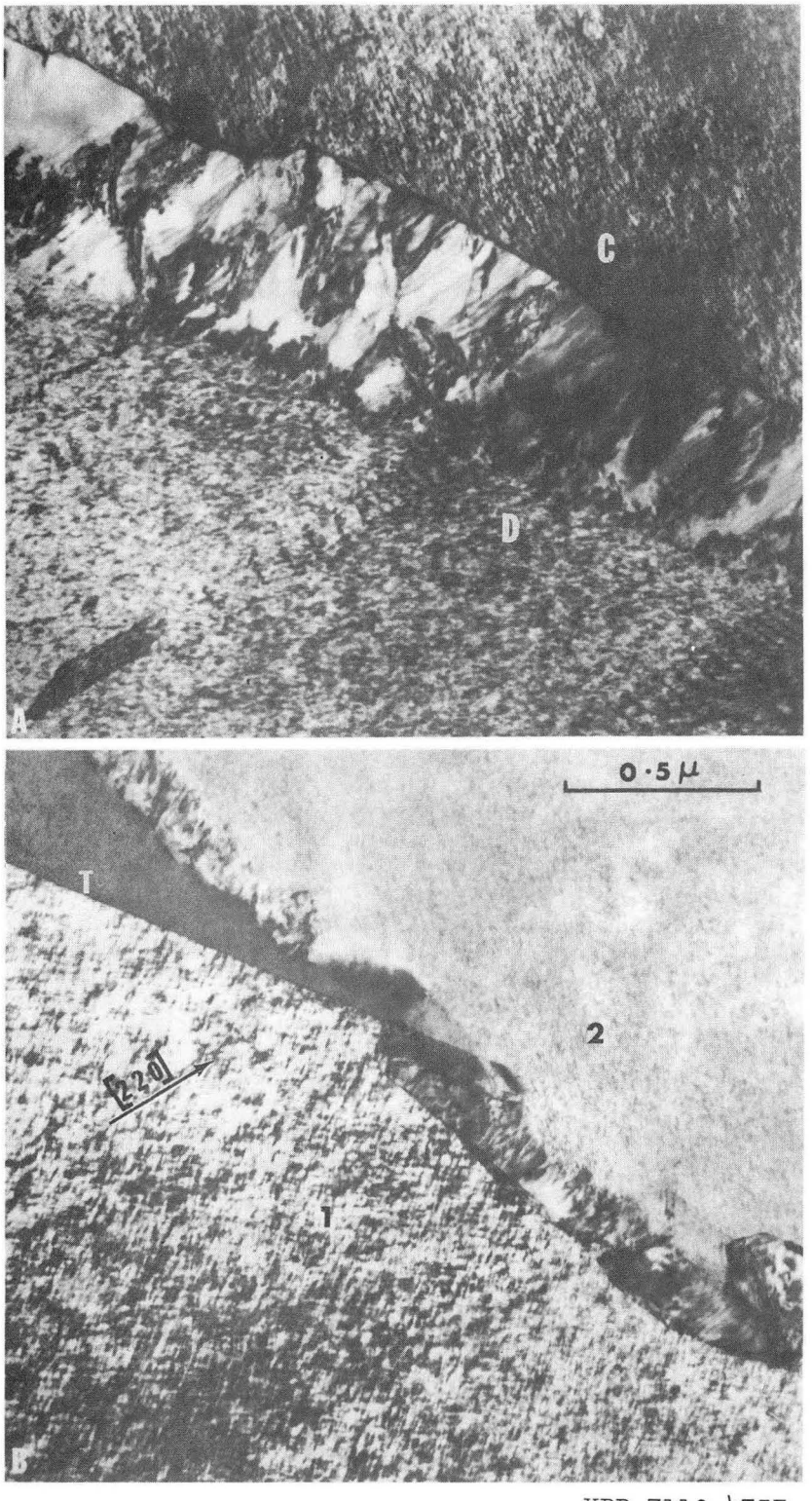

XBB 7110-4757

Fig. 38

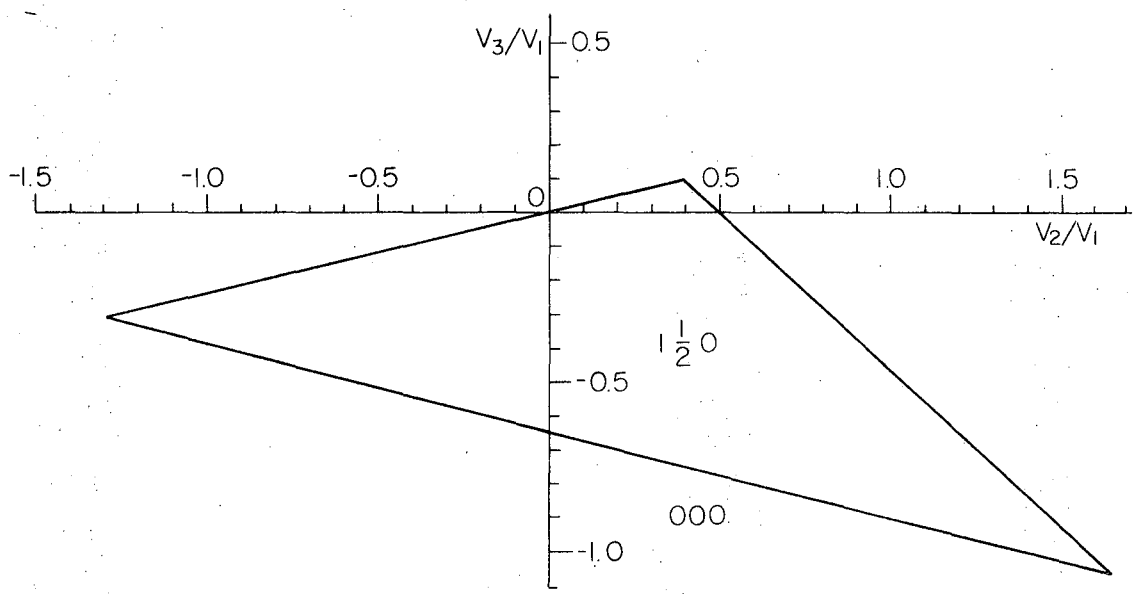

XBL 7110-7336

Fig. 39

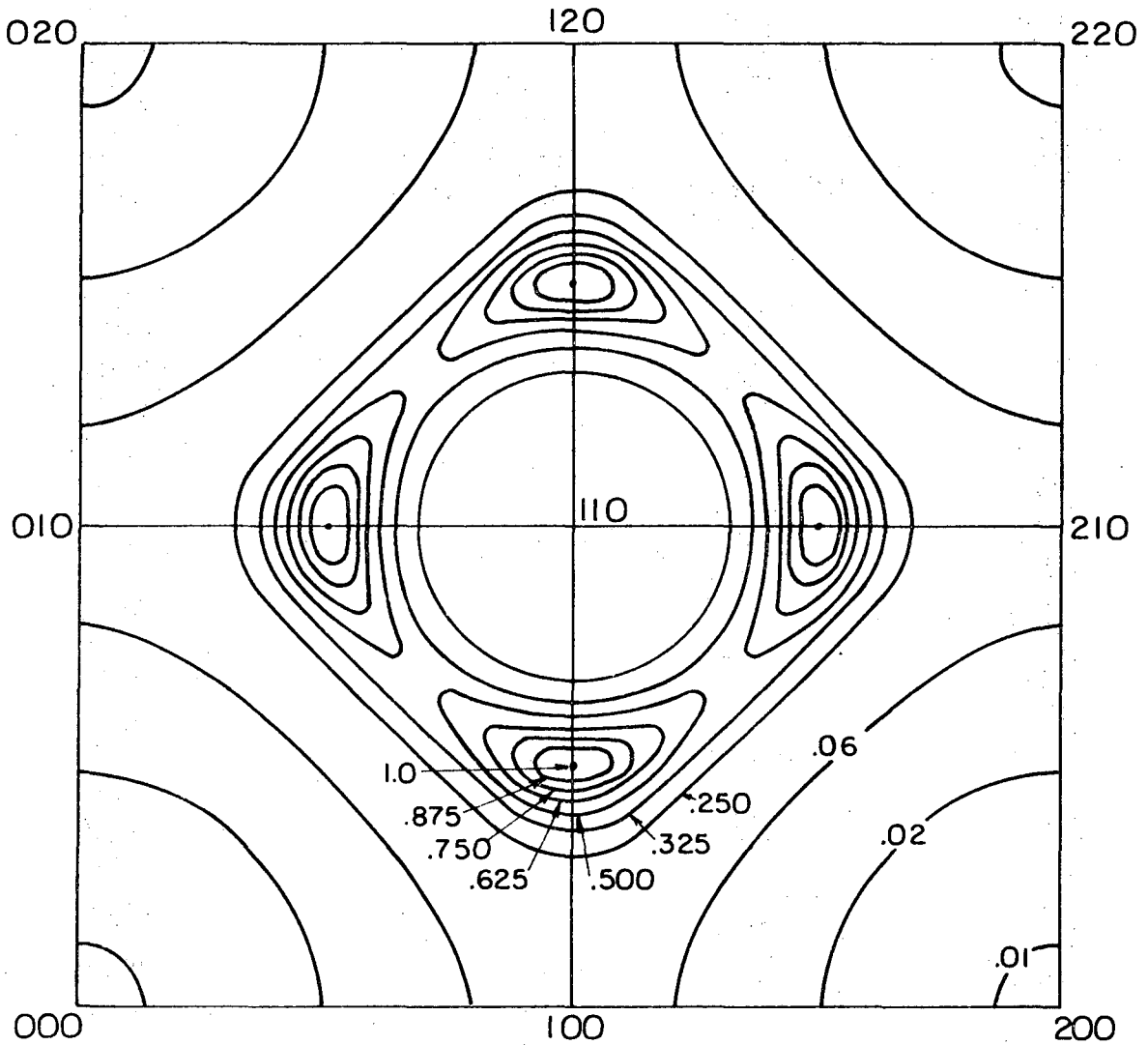

$T_c/T = 0.95$; $V_2/V_1 = 0.4$; $V_3/V_1 = 0.00$

XBL 717-7007

Fig. 40

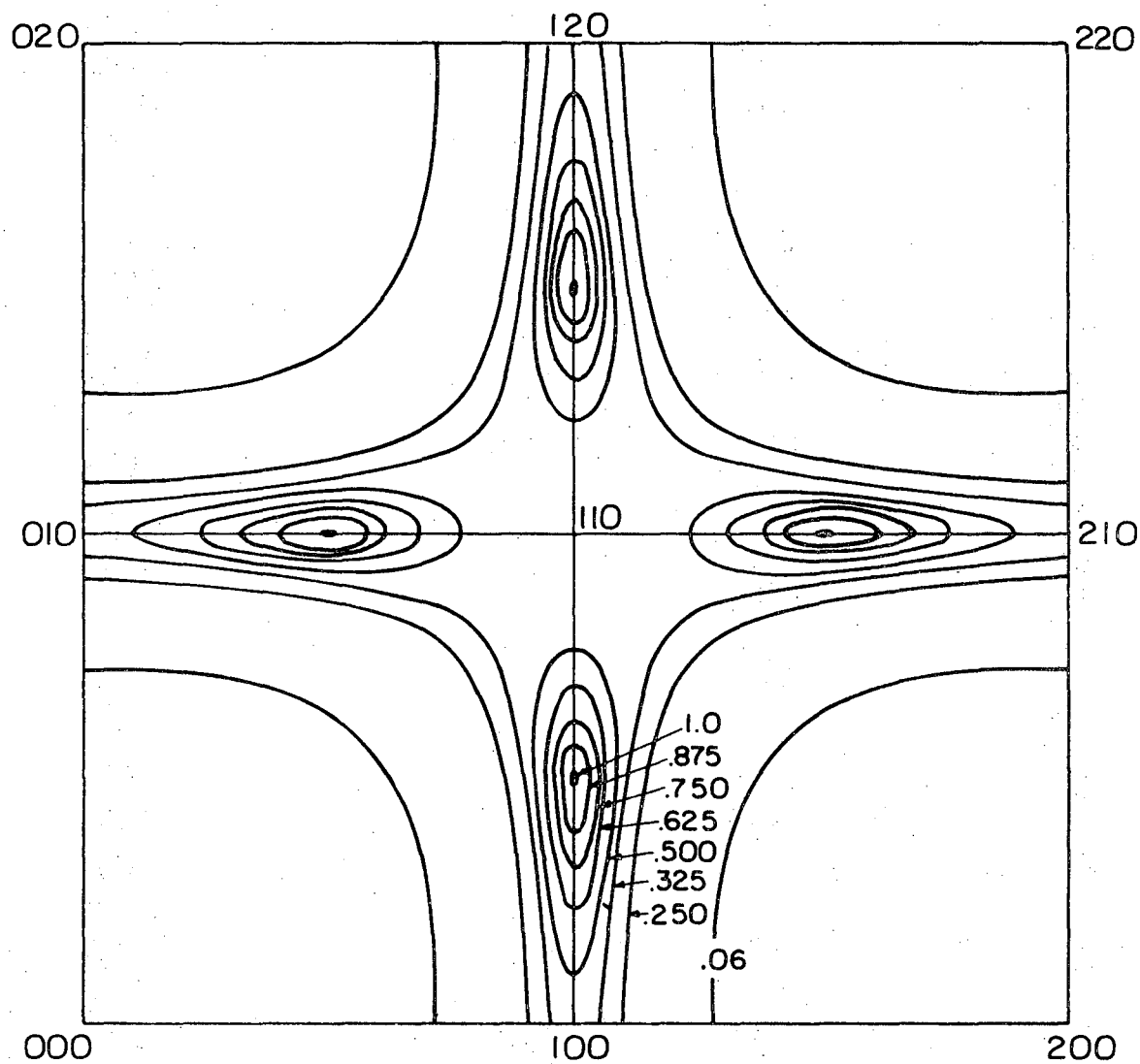

$T_c/T = 0.95$; $V_2/V_1 = 0.7$; $V_3/V_1 = -0.2$

XBL717-7010

Fig. 41

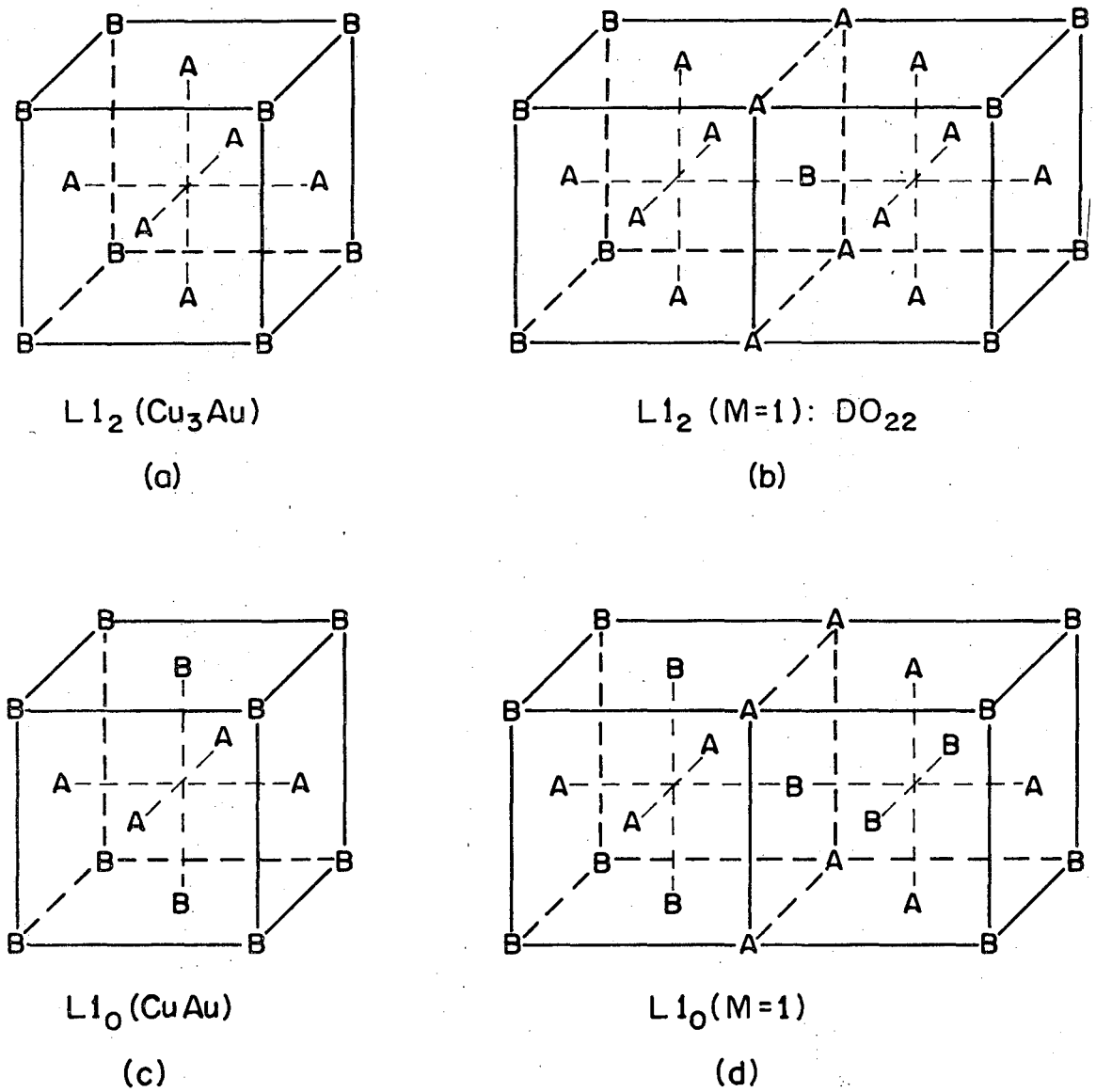

fcc based ordered structures for compositions A_3B (top) and AB (bottom)

XBL713-6622

Fig. 42

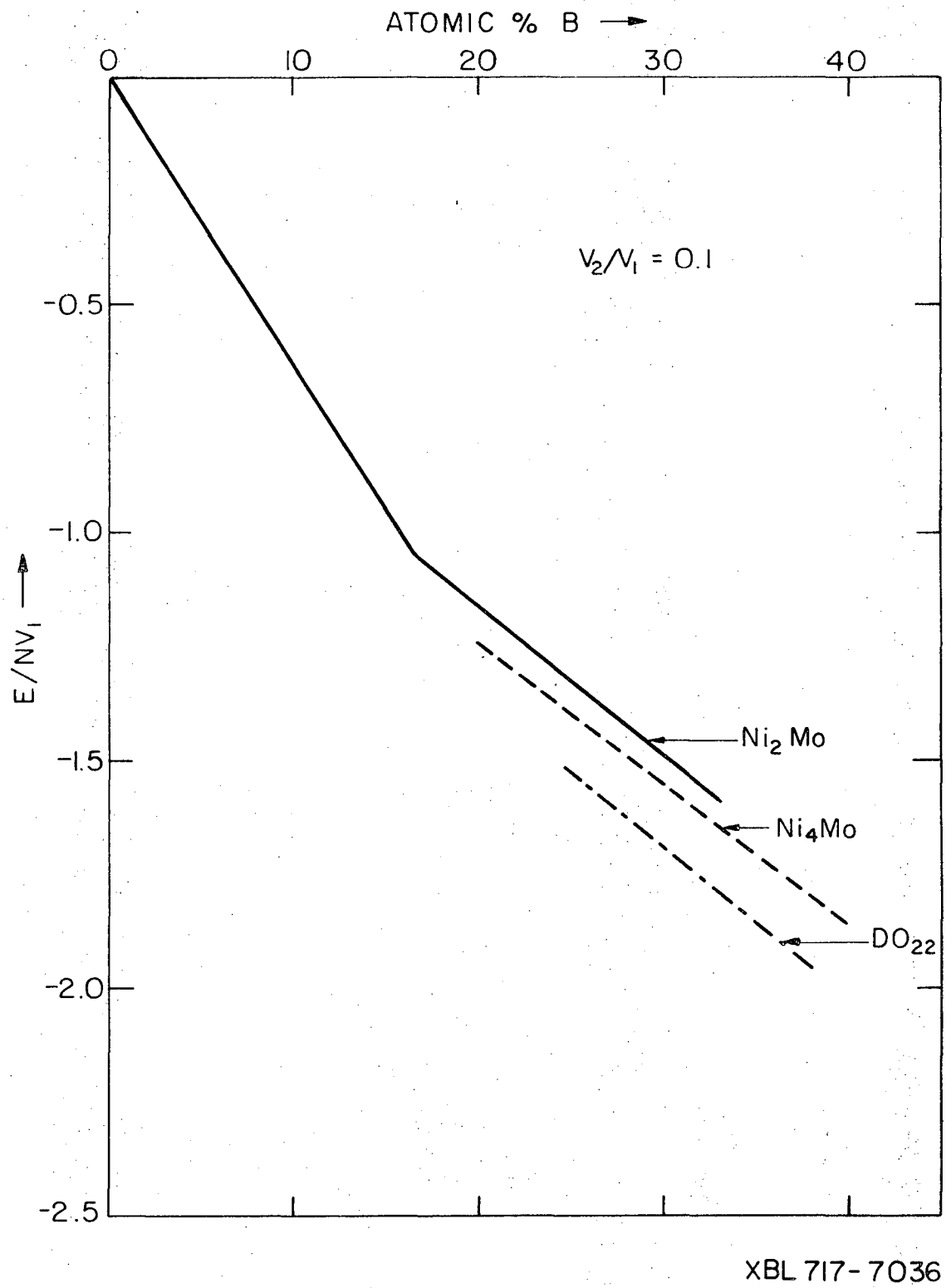
ATOMIC % B
0
10
20
30
40
$V_2/V_1 = 0.1$
-0.5
-1.0
-1.5
-2.0
-2.5
E/NV_1
Ni_2Mo
Ni_4Mo
DO_{22}
XBL 717-7036

Fig. 43a

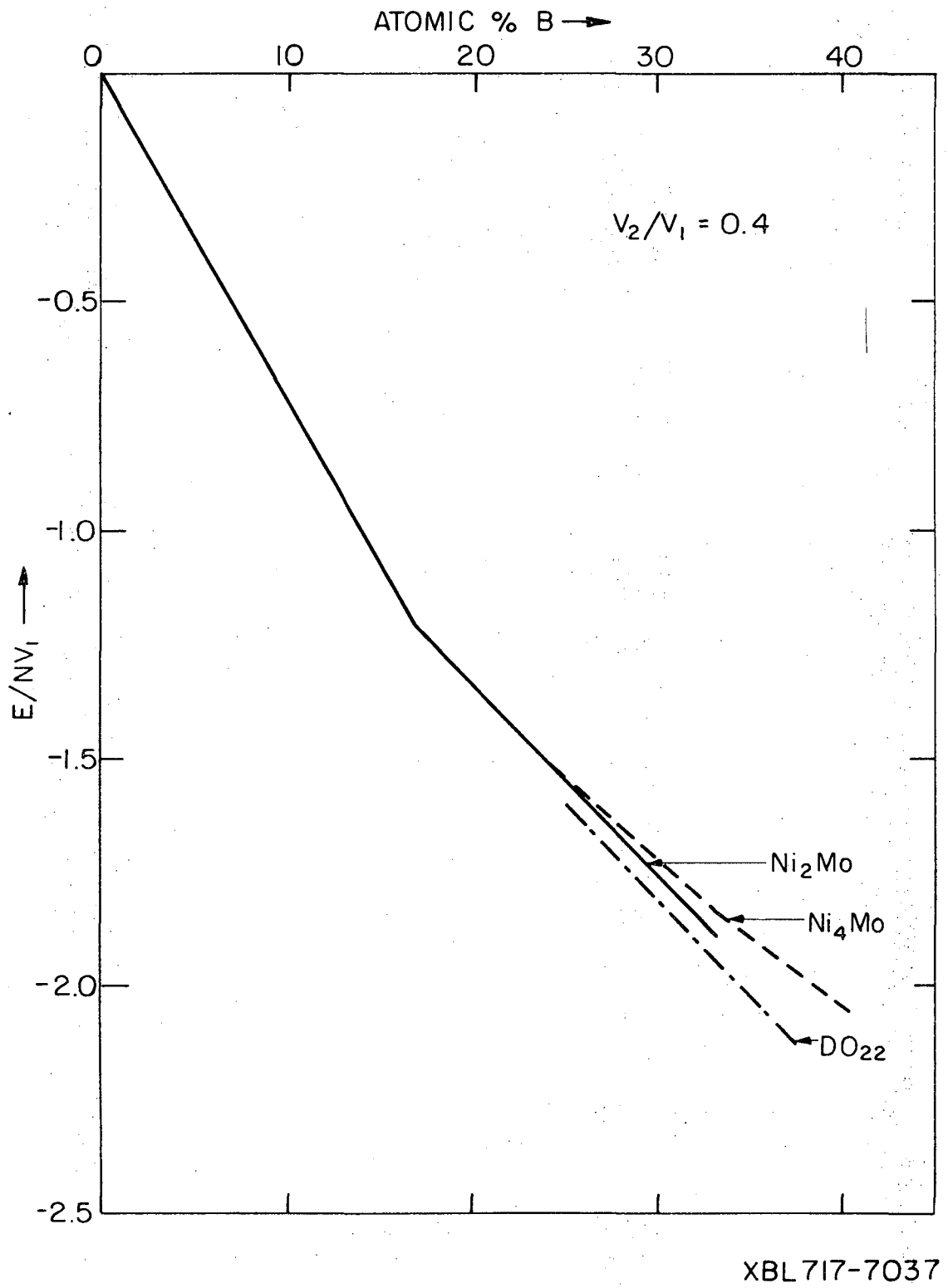
ATOMIC % B
0
10
20
30
40
$V_2/V_1 = 0.4$
-0.5
-1.0
-1.5
-2.0
-2.5
E/NV_1
Ni_2Mo
Ni_4Mo
DO_{22}
XBL 717-7037

Fig. 43b

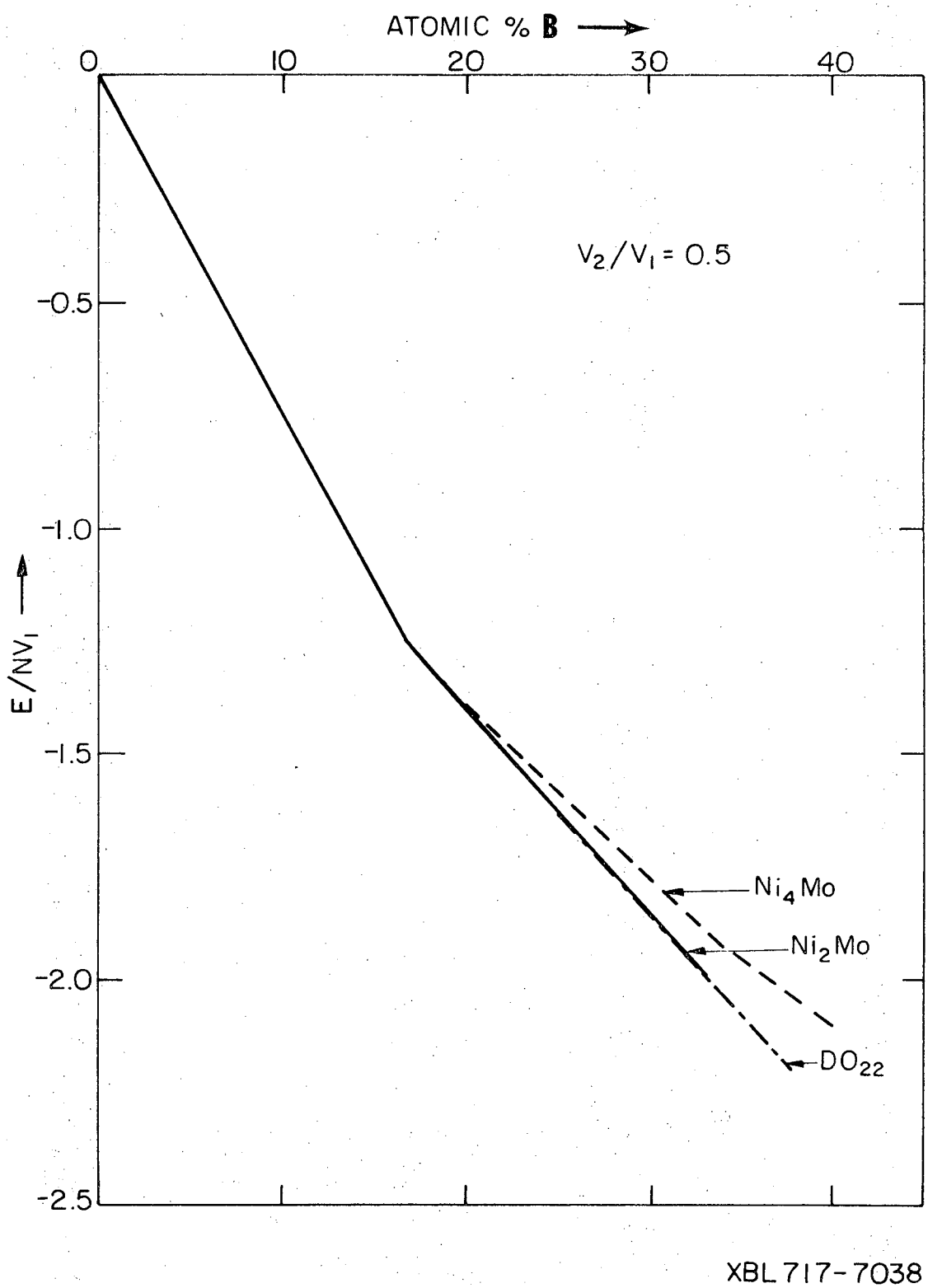
ATOMIC % B
0
10
20
30
40
$V_2/V_1 = 0.5$
-0.5
-1.0
-1.5
-2.0
-2.5
E/NV_1
Ni_4Mo
Ni_2Mo
DO_{22}
XBL 717-7038

Fig. 43c

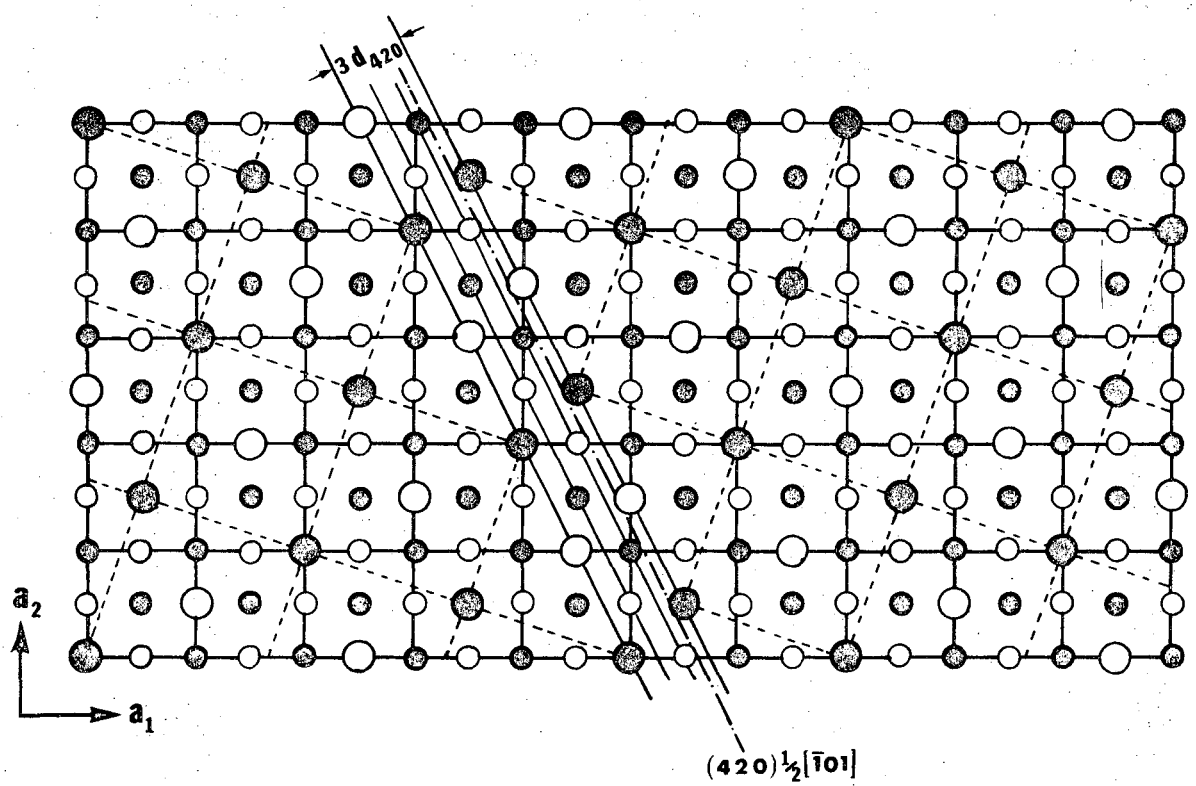

XBL 717-1216

Fig. 44

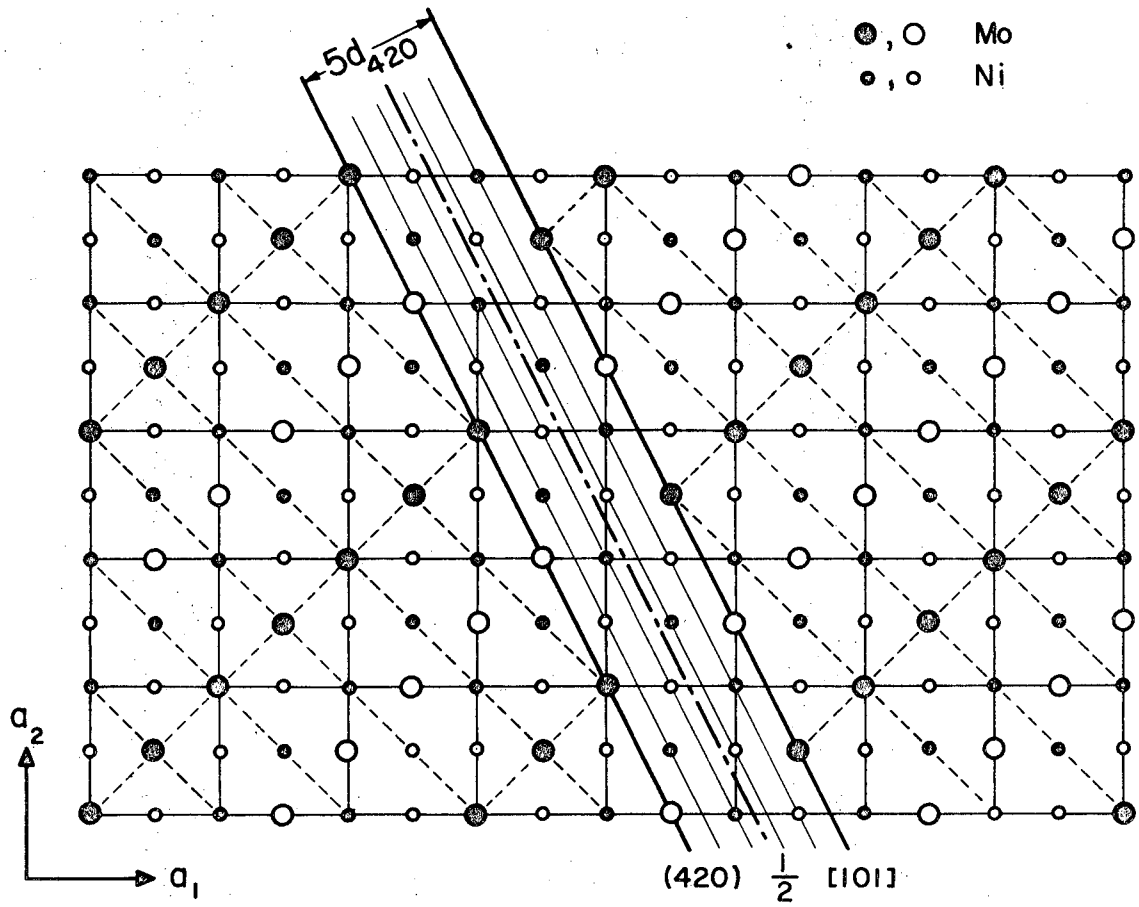

XBL 7111-7648

Fig. 45

LEGAL NOTICE

This report was prepared as an account of work sponsored by the United States Government. Neither the United States nor the United States Atomic Energy Commission, nor any of their employees, nor any of their contractors, subcontractors, or their employees, makes any warranty, express or implied, or assumes any legal liability or responsibility for the accuracy, completeness or usefulness of any information, apparatus, product or process disclosed, or represents that its use would not infringe privately owned rights.

TECHNICAL INFORMATION DIVISION
LAWRENCE BERKELEY LABORATORY
UNIVERSITY OF CALIFORNIA
BERKELEY, CALIFORNIA 94720